NAZARBAYEV UNIVERSITY

DESIGN AND CHARACTERIZATION OF HIGH-PERFORMANCE LAYERED CATHODE MATERIALS FOR SODIUM-ION BATTERIES

by
Lunara Rakhymbay

Submitted in partial fulfillment of the requirements for the degree of
Doctor of Philosophy in Chemical Engineering

School of Engineering and Digital Sciences
Nazarbayev University

Supervised by:
Professor Zhumabay Bakenov
Assistant Professor Aishuak Konarov
Professor Seung-Taek Myung

February 2025

Declaration

I thus affirm that the research presented in this thesis, unless explicitly stated differently, is the exclusive and authentic creation of the author. The thesis has not been previously presented to this or any other university for the purpose of obtaining a degree and does not include any content that has already been submitted for the purpose of obtaining a degree.

Lunara Rakhymbay

February 18, 2025

Abstract

Sodium-ion batteries (SIBs) have garnered significant interest owing to their potential in advancing future energy storage technology. Nonetheless, a major limitation hindering their practical deployment is the insufficient performance of cathode materials, particularly Mn-based layered oxides, which undergo significant capacity deterioration caused by structural alterations during cycling. This thesis provides a comprehensive analysis of the structural and electrochemical properties of innovative layered oxides, focusing on doping methods to enhance their performance.

An in-depth examination of the P3-$Na_{0.62}Mn_{0.75}Cu_{0.19}O_2$ material underscores the notable influence of partial doping with Cu on enhancing structural durability and electrochemical efficiency. *Operando* XRD analyses indicate that Cu-doping enhances the stability of the single-phase reaction and inhibits the unwanted P3-O3 phase transition throughout the cycling process. Moreover, *operando* DEMS verifies that there is no irreversible O_2 gas evolution, highlighting the reversible oxygen redox stability P3-$Na_{0.62}Mn_{0.75}Cu_{0.19}O_2$. XANES studies, complemented by XPS, reveal the active participation of Cu^{2+}/Cu^{3+}, Mn^{3+}/Mn^{4+}, and O^{2-}/O^{n-} redox pairs, leading to a remarkable discharge capacity of 212.2 mAh g^{-1} (0.79 Na^+). Alongside P3-$Na_{0.62}Mn_{0.75}Cu_{0.19}O_2$ the present dissertation delves into the synthesis and characterization of a series of Na_x(Ni–Fe–Mn)O_2 cathode materials, specifically focusing on varying sodium content (x = 0.75, 0.85, and 0.95). The $Na_{0.95}Mn_{0.4}Fe_{0.25}Ni_{0.35}O_2$ cathode material demonstrated exceptional electrochemical performance exhibited 175.7 mAh g^{-1} and with 77% capacity retention after 100 cycles. The findings indicate that optimizing sodium content significantly lowers charge transfer resistance and improves Na^+ ion diffusion kinetics. *Operando* XRD validated the reversible O3–P3 phase transitions, demonstrating no irreversible structural degradation, while *in situ* Mössbauer spectroscopy offered valuable insights into the iron redox behavior at elevated voltages, which observed quick oxidation process to 4+. This study shows that Cu-doping and precise composition tuning are key to improving oxygen redox activity and structural stability in Mn-based layered oxides. The progress made in this area leads to improved cycling stability, increased energy density, and the possibility of commercializing sodium-ion batteries, setting the stage for sustainable and efficient energy storage options.

Acknowledgement

Pursuing a PhD in Chemical Engineering has been one of the most challenging and fulfilling journeys in my entire life. This thesis work would not have been possible without the guidance, advice, support, and encouragement of many individuals and institutions, and I owe them my sincere heartfelt gratitude.

First of all, I would like to sincerely thank my supervisor, Professor Zhumabay Bakenov. His advice, assistance, and constructive feedback helped me overcome various hurdles in my research. At the same time, I am equally grateful to my co-supervisor, Professor Aishuak Konarov, for his steady support, clear guidance, and endless patience throughout my studies. His expertise and encouragement have played a key role in my professional and personal development. I also extend my gratitude to my external supervisor, Professor Seung-Taek Myung, whose specialized knowledge and fresh perspective significantly improved the quality of my work.

I would like to express my appreciation to my friends Nurzhan Baikalov, Aizhan Rakhmanova, Nurbolat Issatayev, Gani Yergaliuly, Zhansaule Bagindyk and Zhamal Yermekbay. Their friendliness, advice, and thought-provoking discussions made my time in this program more enjoyable and valuable for my personal growth. I am also particularly beyond grateful to Alibi Namazbay and Maksat Karlykan, who worked tirelessly alongside me during our experiments in the lab. Their commitment, presence, and assistance in the lab helped me stay motivated and made even the longest days feel rewarding and worthy. I feel fortunate to have had them as a part of my team.

On a personal note, I owe a great debt of gratitude to my family for their endless support and love. My parents, Samat Sadybayev and Binur Sadybayeva, and brothers who have always encouraged me to be curious and persistent. Finally, I would like to express my heartfelt gratitude to my fiancé, whose everlasting love, patience, and encouragement have provided me with steady courage during defense. Their belief in my abilities have laid a solid foundation for everything I have achieved. Thus, I extend my endless gratitude to them.

Table of Contents

List of Tables

List of Figures

List of Abbreviations

LIBs- Lithium-Ion Batteries
SIBs- Sodium-Ion Batteries
LTM- Layered transition metal
TM- transition metal
XRD- X-ray diffraction
XAS- X-ray absorption spectroscopy
SHE- Standard Hydrogen Electrode
PBA- Prussian blue Analogues
ARR- Arrhenius Reaction Rate
EELS- Electron Energy Loss Spectroscopy
NEXAFS- Near-Edge X-ray Absorption Fine Structure
XANES- X-ray Absorption Near-Edge Structure
SXAS- Soft X-ray Absorption Spectroscopy
DOS- Density of States
tg- Transition Gap
e_g- Energy Gap
DFT- Density Functional Theory
SEI- Solid Electrolyte Interphase
STF- Surface Tension Force Measurement
SEM- Scanning electron microscopy
HR-TEM- High-resolution transmission electron microscopy
XPS- X-ray Photoelectron Spectroscopy
ICP-AES- Inductively coupled plasma–atomic emission spectroscopy
XRF- X-ray Fluorescence Spectroscopy
DEMS- In-situ differential electrochemical mass spectrometry
GITT- Galvanostatic Intermittent Titration Technique (GITT)
HC- Hard Carbon
SAED- Selected area electron diffraction
PC-Propylene carbonate
AB- Acetylene black
PVDF- Polyvinylidene fluoride
FEC- Fluoroethylene carbonate
AGM- Absorbed Glassmat
NaMCO- $Na_{0.62}Mn_{1-x}Cu_xO_2$
NNFM75, NNFM85, and NNFM95-$Na_{0.75}Mn_{0.4}Fe_{0.45}Ni_{0.15}O_2$, $Na_{0.85}Mn_{0.4}Fe_{0.35}Ni_{0.25}O_2$, $Na_{0.95}Mn_{0.4}Fe_{0.25}Ni_{0.35}O_2$

CHAPTER 1: Introduction

1.1 Intention of research

Recently, the fast rise of renewable energy technologies and the rising need for better energy storage have shown that we need improved battery technologies. Lithium-ion batteries (LIBs) are popular because they can store a lot of energy and are well-developed. However, they have serious issues like limited resources, high prices, and adverse environmental effects[1].

Sodium-ion batteries (SIBs) are becoming an attractive option because sodium is more readily available and more affordable than lithium. SIBs present an opportunity for cost-effective and environmentally sustainable energy storage, especially for large-scale energy grids[2]. New developments in sodium-ion battery technology have centered on designing new materials and optimizing current varieties to enhance performance parameters comprising energy density and cycle life. Among its components, cathode materials are crucial in influencing the overall performance of a battery. While substantial improvements have been made, numerous current cathode materials still encounter challenges related to structural integrity and capacity. The optimal cathode material for sodium-ion batteries must be both economically viable and environmentally friendly, while also demonstrating strong battery performance and extended cycle life[1,3].

Layered transition metal oxides (Na_xMO_2) are currently being thoroughly investigated as potential cathode options for SIBs, owing to their affordability and comparatively high specific capacity. Following the sodium content, Na_xMO_2 can be classified to two major structural types : P2-type (with $x \leq 0.7$) in which Na^+ occupies by prismatic sites and O3-type (with $0.7 \leq x \leq 1$), which features an octahedral Na^+ environment, as defined by Delmas[4]. O3-type layered oxides exhibit a high initial capacity; however, they undergo structural degradation during cycling as a result of irreversible phase changes. The process of sodium extraction/insertion in O3-type materials typically leads to a phase transition from O3 to P3, accompanied by significant volume alterations that impact structural integrity and cycle longevity[5]. Nonetheless, P2-type layered oxides exhibit enhanced stability throughout the cycling process, thereby enhancing structural integrity and rate performance.

Recent research efforts have concentrated on altering the composition and structure of these layered oxides to achieve an acceptable compromise involving capacity and stability. Approaches consisting of elemental doping, surface coating, and the incorporation of oxygen

vacancies have been investigated to improve their electrochemical performance[6]. Moreover, the incorporation of oxygen vacancies can boost electronic conductivity and promote quicker sodium-ion diffusion, thus enhancing rate capability. The Jahn-Teller distortion, particularly occurs as a result of the existence of Mn^{3+} ions, while the dissolution of passive Mn^{2+} at the cathode-electrolyte boundary over the discharge are two of the obstacles that LTMOs encounter. On the contrary, these obstacles have not yet been thoroughly handled[7].

In order to tackle these challenges, a range of strategies has been investigated in the past several decades. One method includes the partially replacing of Mn with various electrochemically active or inactive cations, including Ni, Co, Li, Mg, Co, Fe, and Al[8–12]. This substitution seeks to reduce the Jahn-Teller distortions and enhance the overall stability of cathode materials. Furthermore, there is a growing interest in improving the capacity of cathode materials by utilizing anionic redox activity in Mn-based TMO. This strategy, usually integrated with doping, offers encouraging prospects for charge storage on oxygen ions, thus enhancing the entire capacity and durability of sodium-ion batteries[13].

1.2 Thesis hypothesis

1. Elemental doping (Cu) into P3-type layered cathodes will improve the electrochemical properties of cathodes by strengthening structural stability.
2. The incorporation of Mn, Ni, and Fe into layered oxide cathodes improves structural integrity and suppresses distortions, thereby enhancing capacity retention.

1.3 The aspiration and novelty of the research

This PhD study focuses on investigating and advancing high-capacity cathodes for sodium-ion batteries, with the intention of enhancing their overall performance significantly. This involves researching novel materials and structural configurations that have the potential to improve the energy density, stability, and cycle life of SIB. The aims of the investigation in the doctoral study are divided into three sections. Multiple tasks were identified to achieve every aspect.

Objective 1: Cu-doping in $Na_{0.62}Cu_xMn_{1-x}O_2$ system.

The first objective is to investigate the impact of Cu-doping on the $Na_{0.62}Cu_xMn_{1-x}O_2$ system to improve structural stability and electrochemical performance. This will involve the following:

1. Synthesizing a sequence of Cu-doped $Na_{0.62}Cu_xMn_{1-x}O_2$ materials with different doping concentrations

2. Studying the effects of doping on crystal structure, oxygen redox processes and on the electrochemical performance.

Objective 2: The integration and Fe in Na_xMO_2 cathodes.

The second objective aims to integrate Mn, Ni, and Fe into the Na_xMO_2 cathode to achieve effective balance among capacity, cycling stability, and cost-effectiveness. This will comprise:

1. Developing a range of $Na_xNi_yFe_zMn_{(1-(y+z))}O_2$ cathode materials in various compositions.
2. Performing comparative analyses to assess the impact of Mn, Ni, and Fe integration on electrochemical performance and to determine the most promising material compositions.

Objective 3: Comprehensive studies of Mn, Fe and Ni-substituted cathode.

The third objective involves conducting an in-depth investigation of Mn, Fe and Ni-substituted cathode material for extended cycling. This will be accomplished using sophisticated characterisation methods, which include:

1. Applying *in situ* Mössbauer spectroscopy to investigate the reduction behavior of Fe throughout the cycling process.
2. Using *ex situ* XANES to explore local structural alterations and oxidation states.
3. Performing *operando* XRD to observe phase transitions and assess structural stability.

It should be noted that throughout this thesis, the term “doping” is used in a broad sense and refers specifically to the substitution of one transition metal ion for another within the host lattice structure.

1.4 Research contribution

During the PhD program 4 research papers, 3 review papers and 2 patents were published. The list of papers is listed below:

1. **L.Rakhymbay**, Z.Zhakiyeva, Z,Bagindyk, S.T. Myung, Z. Bakenov and A.Konarov, Durable Cu-Doped P3-$Na_{0.62}Mn_{1-X}Cu_xO_2$ Cathodes for High-Capacity Sodium-Ion Batteries. Journal of Materials Chemistry A: 2025. DOI https://doi.org/10.1039/D4TA07432G (Q1. IF=11.9).
2. M.Kalibek, **L.Rakhymbay**, Z.Zhakiyeva, Z.Bakenov, S.T. Myung, A.Konarov. From food waste to high-capacity hard carbon for rechargeable sodium-ion batteries, 2024, Carbon Resources Conversion. https://doi.org/10.1016/j.crcon.2024.100225 (Q1. IF=6.4).
3. B.Shugay, **L.Rakhymbay**, A.Konarov, S.T.Myung, and Z.Bakenov Enhanced electrochemical performance of sodium cathode materials with partial substitution of Zr, 2023, Electrochemistry Communications. https://doi.org/10.1016/j.elecom.2022.107413 (Q1. IF=5.7).
4. **L.Rakhymbay**, A.Namazbay, M.Karlykan, M.Abilkairova, A.Konarov and Z.Bakenov. Preparation of Fe-doped $Na_2Mn_3O_7$ and its Application as a Cathode Material for Sodium-ion Batteries, 2022, International Journal of Electrochemical Science. https://doi.org/10.20964/2022.12.28 (Q3. IF=1.2).
5. A.Namazbay, M.Karlykan, **L.Rakhymbay**, Z. Bakenov, N. Voronina, S.T Myung and A.Konarov. Towards High-Performance Sodium-ion Batteries: A Comprehensive Review on $Na_xNi_yFe_zMn_{1-(y+z)}O_2$ cathode materials. Energy Storage Materials. (Q1. IF=17.7).
6. **L.Rakhymbay**, N.Bazybek, K. Kudaibergenov, S.T. Myung, Z. Bakenov and A.Konarov. Present development and future perspectives on biowaste-derived hard carbon anodes for room temperature sodium-ion batteries, Journal of Power Sources, 2024. https://doi.org/10.1016/j.jpowsour.2024.234347 (Q1. IF=8.1).
7. **L.Rakhymbay**, A.Namazbay, M.Karlykan, M.Abilkairova, A.Konarov and Z.Bakenov. Preparation of Fe-doped $Na_2Mn_3O_7$ and its Application as a Cathode Material for Sodium-ion Batteries, 2022, International Journal of Electrochemical Science. https://doi.org/10.20964/2022.12.28 (Q3. IF=1.2).
8. **L.Rakhymbay**, A.Namazbay, M.Karlykan, B.Shugay, A.Konarov and Z.Bakenov. Recent Advances in Layered $Na_2Mn_3O_7$ Cathode Materials for Sodium-Ion Batteries, 2023, Eurasian Journal of Chemistry. https://doi.org/10.31489/2959-0663/1-23-5

Patents:

1. **L.Rakhymbay**, N. Bazybek and A.Konarov. Method of production of hard carbon material

for anodes of sodium-ion batteries, CN 106299365 A, 2024.

2. **L. Rakhymbay**, Z.Bakenov and A.Konarov. Method of obtaining a layered cathode material for sodium-ion batteries CN 108923042 B, 2023.

1.5 Thesis overview

This PhD thesis is divided into several main chapters, beginning with the synthesis of layered oxide cathode materials, followed by their structural and electrochemical optimization for enhanced sodium-ion battery performance.

Chapter 1 begins with an introduction to the research context, outlining the primary objectives, hypothesis, and the research contributions.

Introduction to the research's objectives, hypothesis, goals, and research contributions

Chapter 2 provides a comprehensive literature review, offering an overview of SIB technology, its working mechanisms, and recent advancements in cathode materials: to layered-type cathodes and the role of anionic redox in enhancing electrochemical performance.

Chapter 3 outlines the research methodology used for material synthesis, analytical techniques employed throughout this work: structural characterization, and electrochemical evaluation.

Chapter 4 focuses on investigation of Cu-doped $Na_{0.62}Mn_{1-x}Cu_xO_2$ where the effects of Cu-doping on the structural integrity and electrochemical behavior of the material are thoroughly examined.

Chapter 5 explores Ni/Fe/Mn based layered cathode materials, which compositions are evaluated for their structural stability and suitability as viable SIB cathodes.

Chapter 6 presents advances in O3- $Na_{0.95}Ni_{0.35}Mn_{0.4}Fe_{0.25}O_2$ cathode development for SIBs.

Chapter 7 brings the main conclusions from each experimental chapter and suggests future research ideas to help improve the performance and practical use of sodium-ion battery cathode materials.

CHAPTER 2: Literature Review

2.1 General introduction to SIBs and working mechanism

It is well-established that lithium-ion batteries (LIBs) have dominated the battery market due to their outstanding electrochemical characteristics as well as ability to meet the increasing requirements of developing markets for laptops, phones and electric vehicles.

Despite this, limited resources of lithium and cobalt used for cathode materials poses an issue in the sustainability of this type of batteries[14]. In contrary to lithium, sodium, which ranks as the fourth most abundant element on Earth, circumvents this issue. However, the abundance of sodium is not the only reason, which makes it a potential alternative to LIBs. Taking into account the abundance of sodium, being as the second most lightest and smallest alkali metal following lithium with a standard electrode potential (- 2.71 V vs SHE), rechargeable sodium-ion batteries (SIBs) present themselves as a leading alternative to lithium-ion batteries LIBs[2,15]. The mechanism of electrical storage and battery components of SIBs and LIBs are essentially identical, except for their ion carriers [3]. The intercalation chemistry of sodium exhibits similarities to that of lithium regarding cathode materials, allowing for the potential use of materials equivalent to those implemented in lithium-ion batteries. Nonetheless, in spite of these resemblances, LIBs and SIBs exhibit notable distinctions within their systems. The greater size of Na^+ (1.02 Å) in comparison to Li^+ ions (0.76 Å) influences phase stability, transport characteristics, and interphase formation. Moreover, sodium possesses a heavier molecular weight of 23 g mol^{-1} relative to lithium (6.9 g mol^{-1}) and exhibits a higher standard electrode potential than lithium (-3.02 V versus SHE), resulting in a diminished energy density when contrasted with lithium[16]. However, it was indicated that the mass of sodium represents a little portion of the overall component weight, while capacity is predominantly influenced by the characteristics of the host structure. Despite SIBs exhibiting the presence of some weaknesses in contrast to LIBs, SIBs are still recognized attractive as well as cost-effective alternative to LIBs.

There are four main types of cathode material in SIBs that are considered promising: polyanionic materials, Prussian blue analogue, layered oxides, and organic compounds. When it comes to the former, the majority of the polyanionic cathode materials are phosphate and pyrophosphate-based compounds with good cycling stability and industrial viability; however, they also frequently include cobalt or vanadium. Issues of cost and environmental impact arise

when expensive rare metals like vanadium, cobalt, or others are used in large-scale energy storage projects in the future [17]. Next, the affordable price and long cycle life of Prussian blue counterparts are intrinsic benefits, yet their poor specific capacity and facile absorption of interstitial H_2O severely limit mass manufacturing[17]. Following this, there are layered oxides which exhibit satisfactory cycleability and capacity, structural deterioration and inherent material limitations hamper practical full cell fabrication[18]. When it comes to anode materials in SIBs, due to their substantial operating potential, nanostructured metals and alloys, as well as metal sulfides, selenides, and oxides, may deliver high capacity or relatively stable cycling performance without the formation of sodium dendrites. However, a fundamental issue with practical SIBs is the large volume changes in these anode materials during the sodiation/desodiation process[19].

In SIB cells as shown in Fig. 1, during charge, an oxidation reaction takes place at the positive electrode with loss of electrons and de-insertion of Na. Following this, the migration of Na^+ to the negative electrode (e.g., hard carbon) through the electrolyte occurs while there is a transfer of electrons to the anode part through external conduction. This in turn results in a reduction reaction at the anode with the insertion of Na. During discharge, the opposite process occurs[20]. The associated reaction equations as follow:

Charge

Cathode: $NaMO_2 \rightarrow Na_{1-x}MO_2 + xNa^+ + xe^-$

Anode: $C + xNa^+ + xe^- \rightarrow Na_xC$

Overall: $C + NaMO_2 \rightarrow Na_{1-x}MO_2 + Na_xC$

Discharge

Cathode: $Na_{1-x}MO_2 + xNa^+ + xe^- \rightarrow NaMO_2$

Discharge: $Na_xC \rightarrow C + xNa^+ + xe^-$

Overall: $Na_{1-x}MO_2 + Na_xC \rightarrow NaMO_2 + C$

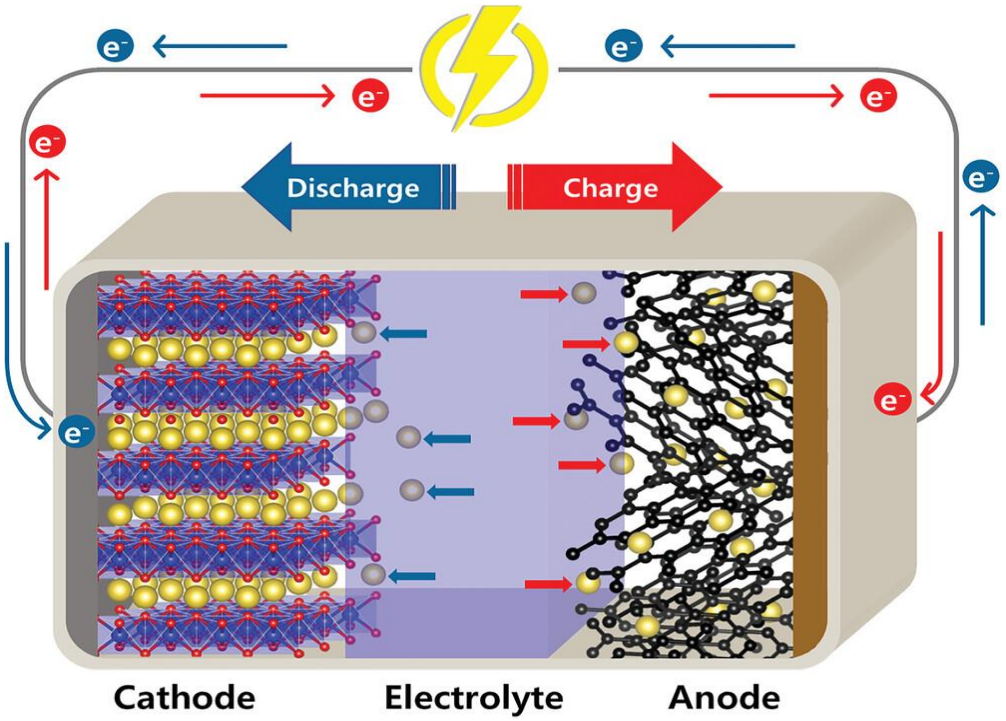

Figure 1. Schematic operation principle of SIBs[21].

2.2 Cathodes, layered type cathodes, and structures

Various cathode materials such as polyanionic cathodes, Prussian blue analogues (PBA), organic compounds, and layered oxides have been extensively investigated for SIBs (Fig. 2a). Their structures can be seen in Fig. 2c. However, successful and practical cathode materials for SIBs play a vital role in defining reliable safety, low cost, high specific energy, large specific power, and long-term cycling-life. Viable cathode materials should exhibit high specific energy, high rate performance, and long cycling life[20]. The cycling life of SIB cathode materials is primarily determined by stability of their structure and electrochemical stability of utilized electrolytes.

Amazingly, throughout the last forty years, Prussian blue (PB) has been investigated in an increasing number of novel, completely unrelated, but extremely promising application areas such as rechargeable batteries[22]. Owing to their remarkable redox activity, affordability, and highly reversible phase transitions that occur when specific cations are inserted or extracted, PB and PBAs have also been extensively researched as potential active materials for energy storage devices, particularly for commercial sodium-ion batteries (SIBs). With a theoretical specific capacity of 170 and 85 mAh g^{-1}, respectively, PB and PBAs might be classified as dual-electron transfer type

and single-electron transfer type based on the quantity of redox-active sites for battery application[23]. Even when compared to $LiFePO_4$, the former one is competitive and shows promise due to their high average voltage and capacity[24,25]. However, PBAs are better suited for systems that promote sustainable cycle life due to their natural low gravimetric energy density, which makes them less appropriate for high specific energy applications. Additionally, PBAs' electrochemical performance is certain to be impacted by the intrinsic crystalline water and structural voids, as they are products of liquid chemical production. To give better theoretical direction, it is still challenging to identify the reaction processes, including any phase change, the water sites inside the structure, and the active sodium storage sites during electrochemical cycling[26].

When it comes to the polyanion type cathodes for SIBs, they have been a major subject of study in recent years due to their unique structure and the benefits of high voltage/high safety. Also, polyanion type cathodes can have strong crystal frameworks and good thermal stability. Furthermore, because of the special "inductive effect," which is connected to the modifications in molecular orbits brought about by the distinct polyanionic groups in these cathodes, polyanion type cathodes often have greater redox potentials[27]. However, polyanionic cathodes have their own disadvantages. Firstly, they have relatively intrinsic low electronic conductivity, which results in inadequate level of Na^+ diffusion. Next, the absence of appropriate electrolytes limits the uses of several polyanion-type compounds with voltages higher than 4.2 V since the typical electrolytes may oxidize beyond that point. In addition, high voltage and high stability would have to be compromised since polyanion-type compounds contain hefty inactive counter cations. The next drawback that should be mentioned is that the valuable and hazardous transition metal vanadium is present in a range of high-performance polyanion-type compounds. It is still difficult to replace element V with less expensive, more ecologically friendly elements without sacrificing their excellent performance. Finally, it should be mentioned that theoretical and practical discharge capacities of compounds of the polyanion type still differ significantly[28]. While phosphate-based polyanionic cathodes such as $Na_3V_2(PO_4)_3$ have been widely studied due to their high operating voltage and structural stability, other families of polyanionic frameworks have also shown promising characteristics for sodium-ion batteries. Sulfate-based compounds like $Na_2Fe_2(SO_4)_3$ exhibit high redox potentials, benefiting from the strong inductive effect of the sulfate group[29]. Silicates, such as Na_2FeSiO_4, have demonstrated structural robustness and stable cycling

performance[30]. Fluorophosphates like $NaVPO_4F$ combine the advantages of phosphate and fluoride anions, leading to improved voltage output and thermal stability[31]. Borate-based materials, though less common, are considered for their lightweight framework and potential for high capacity[32]. Meanwhile, carboxylate-based cathodes—particularly those utilizing aromatic dicarboxylates like $Na_2C_8H_4O_4$—offer tunable redox activity and sustainable design options[33]. Together, these diverse polyanionic systems expand the scope of viable cathode materials for sodium-ion batteries by offering varied electrochemical and structural advantages.

In terms of organic compounds, their flexible molecular structure allows for the reversible accommodation of Na^+ with minimal spatial impediment. This property facilitates the rapid kinetics of the Na^+ insertion/extraction process[34]. Nevertheless, due to their inherently low conductivity, the electrochemical performance of organic materials is significantly inferior to that of inorganic cathode materials, and their operating mechanisms remain poorly understood. By developing organic/carbon hybrid materials, it is anticipated that the electrochemical performance of organic cathodes could be improved. Furthermore, the practical use of organic materials is severely limited by the synthetic process and the high cost of production. Thus, more sensible designs of organic materials with superior electrochemical characteristics might be achieved by refining the synthetic pathway and creating a functional mechanism[35].

Considering the aforementioned aspects of other cathode materials, layered oxides, composed of alternating transition metal (TM) oxide and sodium layers, are high-profile categories of SIB cathode materials due to their relatively high specific energy and better properties compared to the other cathode materials (Fig. 2d)[36]. The prevalence of two-dimensional lamellar oxides in commercially available high energy density Li-ion cells indicates that they represent the most significant class of cathode materials for metal-ion batteries. Almost all of the layered lithium transition metal oxides have sodium counterparts. In Na-ion vs. Li-ion systems, layered AMO_2 (A = alkali, M = transition metal) compounds often show different electrochemical behavior. Due to sodium greater size, which restricts cation disorder and keeps Na^+ from occupying tetrahedral positions, there are slight structural variations despite their similarities. More research has been done on the intercalation chemistry of Na^+ in these compounds than on any other cathode class[15]. In the 1970s, the structures of the sodium layered ternary transition metal oxides were completely studied and explained. The intercalation chemistry of these transitional metal oxides consisting of the first-row transition metals was initially investigated in relation to how removal of Na affected

the structure of the cathode. A considerable portion of the groundbreaking work was derived from studies conducted by Hagenmuller et al. Also, Delmas and Hagenmuller provided specific terminology to characterize the stacking configurations of layered transition metal oxides[15,37].

Unlike their lithium counterparts, almost all $NaMO_2$ (M = transition metal) compounds can reversibly intercalate Na^{+}[38]. The larger size of Na^+ compared to Li^+ helps reduce cation disorder among Na^+ and TM ions. Furthermore, one can integrate different transition metal elements within the transition metal layers, leading to $NaMO_2$ compounds with tunable properties. For example, $NaMO_2$ materials that incorporate Fe and Ni generally demonstrates a high specific capacity and high redox potential due to the Fe^{3+}/Fe^{4+} and Ni^{2+}/Ni^{4+} redox couples[39]. Layered oxides for SIBs demonstrate the Na_xMO_2 formula and the structure is composed of MO_2 slabs and edge-sharing MO_6 octahedra, separated by a layer of Na^+. In general, these materials crystallize in the hexagonal system and sometimes if M is Ni^{3+} or Mn^{3+}, a macroscopic distortion results in an orthorhombic or a monoclinic phase. There is an ion-covalent character of bonds in the MO_2 slabs, which considerably influences their electronic properties (Fig. 2b). An electronic conduction takes place through hopping (semiconductor) or through delocalization (metallic-like) which depends on the amount of alkali metal. The electronic conduction in layered oxides relies on the nature of M cation: i) average oxidation state, ii) the M-M bond distance versus the t_{2g} orbital extension, iii) the occupation of e_g or t_{2g} levels, and iv) the presence of the Jahn-Teller effect In contrast, the Na-O are considered to be more ionic, enabling Na^+ to move within the interslab space if provided sufficient vacancies. The layered structures can remain stable over a wide range of compositions, at least at room temperature, for certain transition elements. The extent of this compositional range relies on the redox potential of $Mn^{3+/4+}$ couple and the stability of the structure. In order for a material to be utilized as a cathode material, it should meet requirements such as electronic and ionic conductivities, and a broad compositional range, provided the redox couple possesses a sufficiently high potential[40].

The sodium-based layered oxides are classified into two primary categories: P2 and O3 types which are governed by the surrounding Na^+ environment and the number of distinct oxide layer stackings, a classification first introduced by Delmas et al.[37] (Fig. 2e). The symbol “O” or “P” denotes an octahedral or prismatic coordination environment of Na^+, whereas “2” or “3” indicates the quantity of transition metal layers with various types of oxygen stacking within a single unit cell[6]. It should be noted that a prime (′) denotes a distorted phase. The O3 phase, which

typically forms when $0.7 \leq x \leq 1$ (Na_xMO_2), has oxide layers arranged in an ABCABC pattern, with each Na^+ sharing one face and one edge. The P2 phase, which occurs when $x \approx 0.7$, has an ABBA pattern of stacking, where each Na^+ shares either all faces or all edges. The P3 phase, usually occurs when $x \approx 0.5$, follows an ABBCCA stacking pattern, with each Na^+ sharing one face with a MO_6 octahedron and three edges with three other MO_6 octahedra[41]. Electrochemical performance is significantly impacted by the phase structures, not only due to the amount of Na in the pristine state but also because of the stability of each layer and kinetics influenced by the surrounding Na environment. For instance, the O3 phase typically experiences a series of phase transitions due to slab-gliding during charging and discharging processes[42]. Overall, the P2 phase tends to exhibit better electrochemical performance than the O3 phase at or beyond 2nd cycle due to its low diffusion barrier and high ionic conductivity[4]. However, the O3 phase typically demonstrates higher 1st charge capacity because it contains more Na in its pristine state. In addition to this, it is considered that P2 phase possesses more stable structure than that of O3 phase since the latter might experience a series of slab gliding while the process of de/intercalation process at room temperature[41]. However, some studies show that transition from P2 to O2 can take place if there is an extensive quantity of Na deintercalated from the host structure implying unstable structure of layered oxides comes from a deep charge state[43].

O3-type layered sodium 3d transition metal oxides, which also involves O'3-type ones, were found between the 1930s and the 1975s, and Delmas et al. published the first reports on the electrode performance of Ti, V, Cr, Mn, Co, and Ni systems in Na cells in 1980–1985. These mentioned oxides are active in electrochemical nature, and for the initial tests, they are frequently assessed using Na-metal half-cells, which have metallic Na as the negative electrode and the oxide as the positive electrode. Electrode materials without Na, including carbon, are placed in the negative electrode of practical Na-ion complete cells since $NaMO_2$ includes Na in its structure. The Na-extraction method is typically used to begin charge/discharge experiments of $NaMO_2$ electrodes, which entail the simultaneous oxidation of transition metals in the half-cell and full cell[15]. When it comes to P2-type layered transition metal oxides, they have also been created to produce high-capacity, high-power, long-life, and safe Na-ion batteries. The rationales behind it was i) boosting operation voltage and a reversible capacity, ii) inhibition of irreversible phase changes and substantial interslab reduction, iii) smoothing voltage profiles with suppressed Na^+/vacancy ordering, iv) mitigation of H_2O insertion into interslab spacing, v) protection of the

surface from HF attack and moist air . It should be mentioned that P2- and O3-type layered oxides with single 3d transition metal systems differ considerably from one another. P2 type phases form with only V, Mn, and Co as single 3d transition metal systems, in opposed to O3-type layered oxides, where the majority of 3d transition metals may be hosted in the slab. P2-type materials typically have low Na concentrations and crystallize around $0.5 \leq x \leq 0.8$ in Na_xMO_2. A lot of researchers have created P2-type cathode materials with the usual $Na_{2/3}MO_2$ composition[15].

In addition to main P2- and O3-type structures, the extraction of Na from these structures results in other phase transitions. In the O3-type structure, Na^+ ions are initially located at edge-sharing octahedral sites coordinated with MO_6 octahedra. As Na^+ ions are partially extracted, vacancies are created, promoting the stabilization of Na^+ at prismatic sites. This transition leads to a structure resembling the P2-type. It should be noted that this transformation takes place without the process of M-O bond breakage and is implemented by the gliding movement of MO_2 slabs. As a result, the previous arrangement of oxygen atoms "AB CA BC" turns into "AB BC CA" and this new structure is defined as P3-type phase (Fig. 2e)[21]. In addition to this, P2-type structure can change into O2-type phase (Fig. 2e). During the extraction of Na^+, it makes the MO_2 slabs to glide in order to occupy octahedral positions and can be caused by Na^+/Li^+ ion exchange. The new phase "AB AC AB" is formed because of this gliding motion and features unique oxygen packing configurations (Fig. 2b). This phase is composed of two distinct MeO_2 crystallographic layers, denoted by the letters AB and AC for the oxygen arrangements. The O2-type phase forms as a result of the octahedral sites created by the vacancies between the AB and AC layers[21].

The first investigated sodium-based layered oxide was sodium cobaltate $NaCoO_2$ and it was studied for its electrochemical sodium intercalation chemistry. This material has attracted a lot of interest in various fields of study because of its intriguing superconducting, thermoelectric, and magnetic characteristics[44]. The first investigations revealed that within a restricted range Na^+ could be reversibly intercalated by the different Na_xCoO_2 polymorphs, with the P2 structure exhibiting the maximum capacity of 95 mAh g^{-1} [45]. It was demonstrated that during the process of de-intercalation of Na^+ from $NaCoO_2$, the O3, O'3, and P'3 structures interconvert reversibly[46]. Next, layered sodium iron oxides ($NaFeO_2$) and sodium manganese oxides ($NaMnO_2$) have drawn significant attention because they contain inexpensive and generally non-toxic elements. The weak electrochemical characteristics of $NaFeO_2$ have limited its application in Na batteries. Although

α -$NaFeO_2$ is the structural model for layered materials in the R-3m space group, the unstable Fe(IV) oxidation state inhibits its functionality in a Na cell[47]. In the α-$NaFeO_2$ type, a wide range of transition metals can be accommodated. According to this fact, the synthesis of $NaMO_2$ suppresses and avoids cation mixing between Na^+ and transition metal ions, and different transition metals are simultaneously adopted to form α-$NaFeO_2$-type solid solutions. This is beneficial for optimizing the composition of Na_xMO_2, which represents attractive electrochemical properties for Na-ion batteries[15]. As the Li-ion battery field swiftly grew in the 1990s, the quantity of known Na-containing layered oxide materials increased dramatically. The usage of the Na compounds as precursors to metastable Li polymorphs that could not be produced via direct solid state chemistry was the primary motivator for this interest[15]. The most investigated layered sodium compound for the implementation as a cathode in SIBs is the $NaNi_{1/2}Mn_{1/2}O_2$ material that was reported by Komaba and his colleagues. In the potential range of 2 to 3.8 V, the material exhibited reasonable reversibility, providing around 120 mAh g^{-1} for a minimum of 15 cycles; charging to 4.5 V thereafter enabled the reinsertion of 0.77 Na (185 mAh g^{-1}), but with a substantial irreversible capacity[48]. For the majority of the layered oxide compounds in SIBs, only about 0.5 Na can be cycled in the structure, delivering capacities of about 120 mAh g^{-1} or less at average potentials of 3.5 V. Therefore, there is an important need for enhancement of the specific capacities of such cathode materials, even though over-extraction of Na^+ has been demonstrated to trigger structural damage in some layered oxides[15].

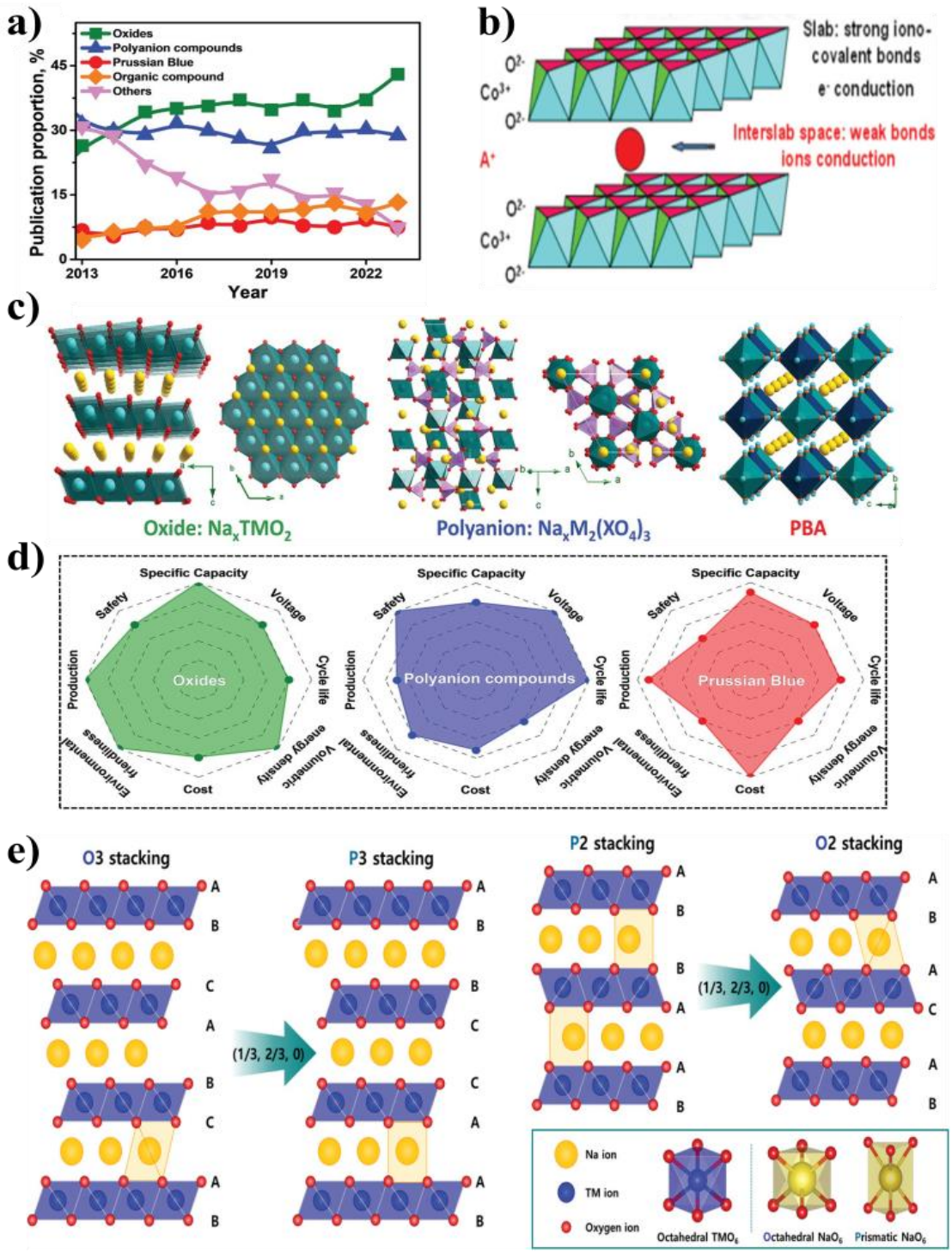

Figure 2. a) Proportion of publications on different cathode materials[36]. b) The general structure of layered oxide. c) Structures of different cathode materials. d) Properties of different cathode materials[36]. e) Schematic representation showing the classification of sodium layered oxide[40].

2.3 Anionic redox mechanism

As mentioned, for SIBs to be practically viable, they must overcome the challenge of the cathode's relatively insufficient capacity. Numerous studies have been conducted to develop high-performance cathode materials through various strategies, including doping modifications, surface treatments, and composite construction. The capacity achieved through cationic redox is near to its theoretical limit and can only be enhanced via other methods such as incorporating anionic redox reactions[49,50]. In fact, anionic redox was first developed for LIBs after it was discovered that lithium-rich cathodes could exhibit capacities beyond their theoretical value. Nevertheless, the fundamental reaction mechanism is still debated and it might be inappropriate to directly apply knowledge of anionic redox from lithium-based systems to sodium-based ones[51]. When Li-rich Li_2MnO_3 delivered a superior initial capacity of more than 400 mAh g^{-1}, Thackeray and Rossouw turned their attention to this material in 1991 and conducted some systematic research[52]. Then, Oishi et al. used soft X-ray absorption spectroscopy (sXAS) to examine the oxygen behavior in Li_2MnO_3 and Li_2MnO_3-based Li-rich oxides[53]. Yet, due to the extreme oxygen release and phase transition from the cathode material, its electrochemical performance was inadequate. Therefore, further investigations on anionic redox reaction of oxygen and modifications have been conducted[54]. It should also be noted that it was not originally thought that anionic redox would occur in oxides as they are less covalent than sulfides[55]. Thus, it was surprising that totally delithiated Li_0CoO_2 could be prepared in 1996[56] , given that magnetic properties indicated that Co had not entirely oxidized to 4+ [56]. Following this, in 1999, it was hypothesized that oxygen participates in the redox process at high potential of Li_xCoO_2 based on the modest reduction in O–O interplanar distances inferred by synchrotron diffraction[57]. After almost two decades of investigations, according to Assat et al., as of 2016, it reached a point when the theory behind the anionic redox process was applied to several kinds of metal-based cathodes (3d, 4d, and 5d). In order to produce reversible anionic redox, the calculations demonstrated the significance of O 2p non-bonding states (or Li–O–Li configurations in panel e, top), the prerequisites for O–O shortening, and the reductive coupling process (panel e, bottom)[55].

Anionic redox reaction (ARR) usually involves the $O^{2-/n-}$ redox couple and can provide additional capacity beyond the well-known cationic redox[58]. According to energy band theory, the energy band structure of Li/Na-based layered transition metal oxides is primarily defined by the overlap between p orbitals of oxygen and d orbitals of transition metals. This overlap is represented

in the energy spectrum by the bonding (M-O) and antibonding (M-O)* bands[55]. The activation of ARR includes their localized/delocalized electronic structures and atomic arrangements. This activation is anticipated to advance the practical use of SIBs[50]. The activation of ARR is closely correlated to the energy of the (M-O)* antibonding orbitals as well as O 2p orbitals according to energy band theory[59,60]. In cationic redox systems, the (M-O)* close to the Fermi level is inclined towards donating electrons for oxidation during charging, while the O 2p states, located far below Fermi level, cannot take part in charge compensation[61]. It is widely accepted that nonbonding O 2p states are essential for triggering ARR. For example, in Li-rich cathode materials such as Li_2MnO_3, one-third of the TM sites are occupied by Li^+ ions, forming configurations of Li-O-Li as shown in Fig. 3a[62]. In these configurations, the O 2p orbitals do not hybridize with either alkali metal orbitals or TM orbitals, resulting in orphaned and unhybridized O 2p states. The density of states (DOS) for these unhybridized O 2p is proportional to the quantity of configurations of Li-O-Li[60]. In terms of the energy of unhybridized O 2p states, it is situated near the Fermi level, as illustrated in Fig. 3b, and it is greater than that of the bonding O 2p states[55]. As a result, the oxygen electrons in the Li-O-Li configurations are more mobile and can participate in the process of charge compensation during high-voltage operation. Thus, it provides additional capacity beyond that provided by the TM redox[62]. As it was mentioned, nonbonding O 2p orbitals are essential to trigger ARR in layered oxides and this principle applies to Na-based TM oxides as well. Similar to what occurs in Li-rich cathode materials, in Na-rich materials; the particular Na-O-Na configurations promote the formation of nonbonding O 2p states, triggering ARR[59]. When it comes to Na-deficient cathodes, the introduction of vacancies or elements with low electronegativity into TM layers to create $Na_xA_yTM_{1-y}O_2$ where A is denoted as those elements. For instance, Mg, Zn, and Li[63]. These elements coordinate with oxygen to form A-O bonds with a strong ionic character and this, in turn, leads to lone-pair oxygen electrons and nonbonding O 2p states. The energy of these nonbonding O 2p states is near to the Fermi level and when (TM-O)* bands are empty, oxide anions can take part in oxidation through donation of electrons, thereby providing additional capacity[64]. From the other perspective, reducing the energy of the nd band of the transition metal can also activate ARR. If $Na_{0.67}Ni_{0.33}Mn_{0.67}O_2$ is taken as an example, the manganese in it is in a tetravalent ($t_{2g}^3e_g^0$) results in lower energy (Mn-O)* bands[65]. The O 2p bands, which are relatively higher energy levels than (Mn-O)* bands are believed to facilitate ARR[66].

There is a significant impact of the various coordination environments of oxygen in the crystal structures of TM oxides on the behavior of ARR. Through density functional theory (DFT) on P2- and O2-$Na_xMg_{1/3}Mn_{2/3}O_2$, Tarascon et al. discovered that ARR can become stable in P-type structure, but is not reversible in the O-type structure[67]. As illustrated in Fig. 3c, in deep dissociation states, O-O dimers that have bond lengths shorter than 2.5 Å are able to be created between neighboring Na layers in the P2 structure. The way how different stacking affects ARR is also elucidated from the viewpoint of the energy band. During the process of charging, the extraction of electrons results in the creation of holes within the narrow nonbonding O 2p band. Concurrently, there is a tendency of formation of oxygen pairs from these holes and this leads to structural distortion, causing varying O-O distances (Fig. 3d). This, in turn, leads to the breakage of O 2p bonds into antibonding and bonding orbitals. Following this, there is a division of the partially filled bands into completely empty and completely filled bands[67].

Certain Na-deficient manganese-based layered structures are discovered to possess an unusually high capacity of a plateau area about 4.2 V in SIBs[10]. For instance, O3 and P2-type layered oxides have been extensively researched as cathodes materials for their great reversible capacity and high operating voltage. Because of its abundance of elements, large reversible capacity, and operating voltage, the $Na_xNi_yMn_{1-y}O_2$ layered oxide has been thoroughly explored as a potential cathode material. It also provides an intriguing example for studying the chemistry of anionic redox reactions in the crystal lattice. According to Ma et al. a relatively novel cathode material $Na_{0.78}Ni_{0.23}Mn_{0.69}O_2$ has a stable structure throughout a broad voltage window and a large and satisfactory capacity of 138 mAh g^{-1}. With the use of soft X-ray absorption spectroscopy (sXAS) and electron energy loss spectroscopy (EELS), the variations in the electronic structures of the bulk and surface of electrochemically cycled particles were examined. It was suggested that the lattice oxygen site with a surface to bulk gradient TM distribution, which is intimately connected to the creation of oxygen vacancies at the material surface, was the location of a portion of the charge compensation mechanism during the first cycle[68]. In addition to this, Susanto et al. examined the source of the irreversible capacity of O3-type $NaFeO_2$. It was done by examining the oxidation state of Fe and transition of phases of the cathode during the process of charging. Through Fe K-edge XAS and O K-edge near edge X-ray absorption fine structure (NEXAFS) investigations, it was possible to witness active redox oxygen atoms for charge compensation in the electrochemical reaction of $NaFeO_2$. It was shown that oxygen redox activity, rather than the

Fe^{3+}/Fe^{4+} redox process, is the mechanism responsible for charge adjustment. Consequently, Fe_3O_4 production and the ensuing oxygen release are what cause electrochemical irreversibility $NaFeO_2$ since they prevent Na from entering the structure[69]. It is also appealing for ternary cathode materials for SIBs to have anionic redox. According to Hakim et al., there is an extra reversible capacity of about 25 mAh g^{-1} for the P2-type $Na_{0.78}Co_{1/2}Mn_{1/3}Ni_{1/6}O_2$ cathode material between 4.2 and 4.5 V. This is thought to be caused by the contribution of anionic redox activity during the charging process[70]. Likewise, Maitra et al. studied and verified that some oxygen loss in the $Na_{2/3}Mg_{0.28}Mn_{0.72}O_2$ and mechanism of charge compensation by the oxygen redox were the causes of the excess capacity. It is paramount to note that Mg^{2+} ions stabilize and reduce oxygen loss throughout the extraction process since they stay dormant in the TM layers. Every O 2p orbital interacts with at least one cation, and oxygen is always coordinated by at least three cations. Corresponding with the absence of oxygen loss in $Na_{2/3}[Mg_{0.28}Mn_{0.72}]O_2$, even at high deintercalation levels, are the absence of non-bonding and very electron-deficient O 2p states[71]. Higher energy density batteries have been created because technology has gotten more advanced. In an intercalation cathode material intended for batteries with higher energy densities in the future, many 3d TMs (Mn, Fe, Co, and Ni) for layered oxides are thought to be the source of the improved charge storage and reversibility. Reversible oxygen redox also offers a promising novel path for the development of future intercalation cathodes materials, as recent observations suggest that it may offer additional capacity over the theoretical TM redox capacity at a high voltage, potentially enabling high energy densities[72].

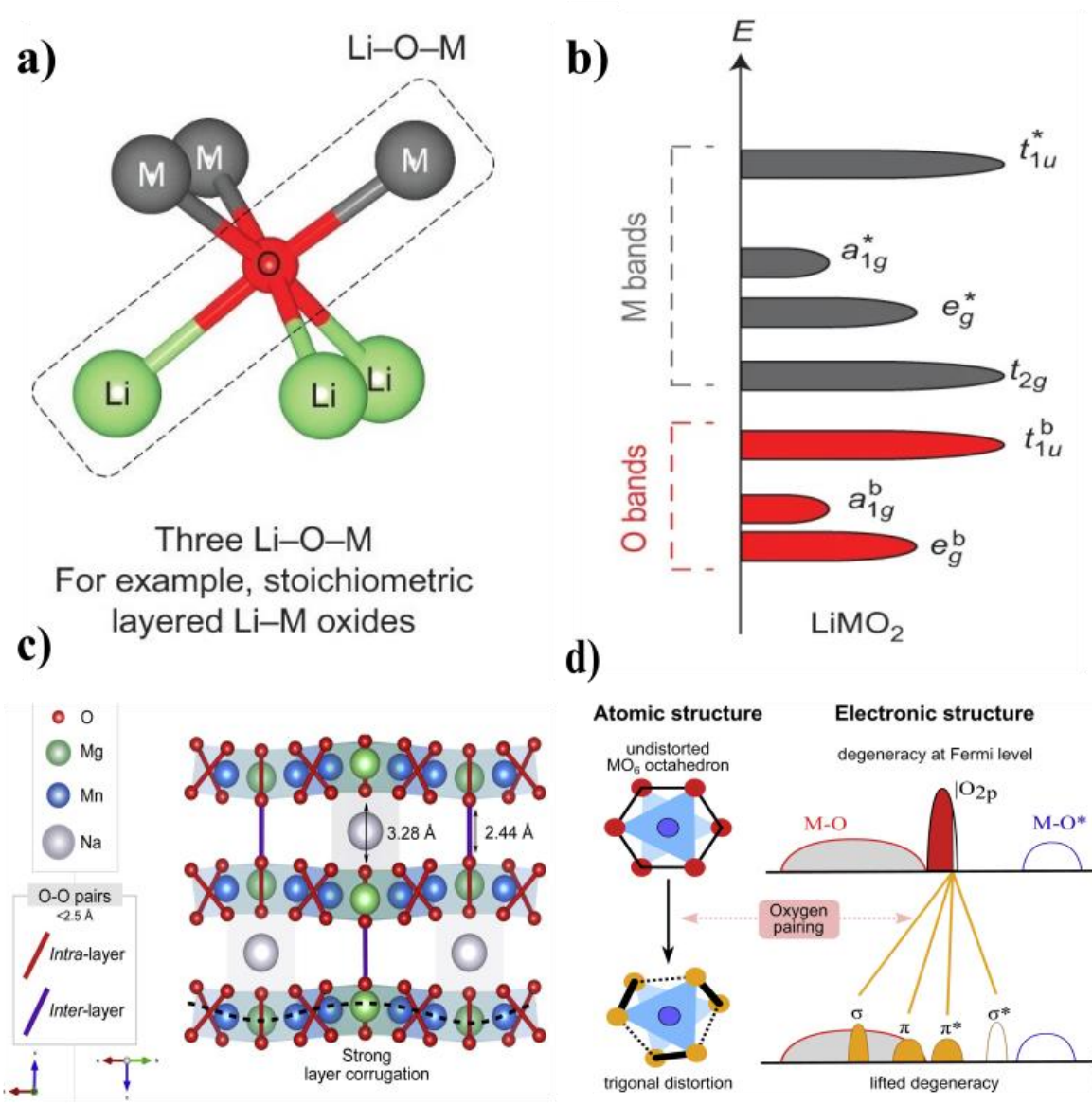

Figure 3. a) Local atomic coordination around oxygen in layered Li metal oxides. b) Schematic of the band structure for stoichiometric layered Li–M oxides[60]. c) Crystalline distortion in desodiated P2 structure. d) Early states of anionic oxidation process[67].

2.4 $Na_xNi_yFe_zMn_{(1-(y+z))}O_2$ cathode

As noted before, LTMO,$NaMO_2$, (M = Ni, Fe, Co, Mn, Ti, V, and their arrangments) are are regarded as highly promising cathode materials because of their high theoretical capacity, ionic mobility and relatively easy synthesis route[73]. Among TMO cathodes, Mn-based ones have been

extensively researched due to the abundance of Mn, its low cost, and significant electrochemical properties. Mn^{3+} in Mn-based layered oxides is inherently unstable, as it tends to disproportionate into Mn^{2+} and Mn^{4+}. The resulting can dissolve into the electrolyte and degrade the solid electrolyte interphase (SEI), reducing performance at the negative electrode[74]. For instance, in 1985 Mendiboure et al. investigated the P2-type Mn-based layered metal oxide $Na_{0.7}MnO_2$, however material excibited poor electrochemical performance[75]. After this, Caballero et al. synthesized P2-type $Na_{0.6}MnO_2$ using the sol-gel method, which delivered 150 mAh g^{-1} within a voltage window of 2.0 - 3.8 V. However, its cycling performance was still unsatisfactory and the material's structure deteriorated during Na^+ insertion and extraction due to the Jahn-Teller effect[76]. Researchers typically address the Jahn-Teller effect by designing novel structures and/or substituting other inactive cations[73].

Considering the potential large-scale commercialization of SIBs for energy storage systems in distributed power grids, effective management of cost of SIBs is crucial. Fe with its low cost and abundant resources has been considered suitable for single-transition metal oxide $NaFeO_2$. Additionally, the solid-state synthesis method for this material is relatively simple and iron is a non-toxic and environmentally friendly element. However, Zhuang et al. reported that $NaFeO_2$ has a capacity of 90 mAh g^{-1} which is less than half of its theoretical capacity of 240 mAh g^{-1} which indicates that only about 35% of Na^+ are reversibly extracted during the charging process[77]. Lee et al. investigated the capacity decay mechanism of $NaFeO_2$ using *ex situ* Mössbauer spectroscopy and found that more than 20% of Fe^{4+} spontaneously reduced to Fe^{3+} during the charge-discharge process which resulted in electrolyte decomposition. *In situ* synchrotron X-ray diffraction analysis confirmed that an irreversible phase transition from O3 to O"3 took place which negatively affected coulombic efficiency and capacity[78]. These issues with capacity and cyclic instability limit the widespread application of $NaFeO_2$ in SIBs.

Ni-based $NaMO_2$ has also been extensively studied as a cathode material for SIBs due to its satisfactory electrochemical performance and relatively simple synthesis method[79]. For instance, O3-type $NaNiO_2$ exhibits a good reversible capacity of about 123 mA h^{-1}, indicating that nearly 50% of Na^+ can be extracted and reinserted into the material[42]. In addition, Ni-containing cathodes used for LIBs feature an open layered framework that allows for the extraction and insertion of Li^+ ions, which provides a high reversible capacity of 200 mAh g^{-1}. This is attributed to the multi-electron reaction of the active nickel ions[80]. Similarly, a comparable oxide is expected

to be a promising host for accommodating more Na^+ to achieve superior capacity. Some studies have shown the high-capacity characteristic of layered oxide cathode materials is strongly correlated with adding of Ni to the structure[42]. Despite having similar elemental composition and comparable crystal structure as LIB Ni-containing oxides, it remains a challenging task to synthesize a comparable highly reversible cathode material for SIBs. For example, $NaNiO_2$ encounters significant structural deterioration during Na^+ insertion and extraction. The phase transitions (O′3–P′3–P″3–O″3–O‴3) lead to irreversible transformations within the material which significantly reduces its capacity[81] .

Overall, it can be seen that Na-based single transition metal oxide cathodes are impractical in contrast to LIBs in which $LiCoO_2$ cathode material is still utilized commercially.

However, in $NaM1_{1-x}M2_xO_2$ (M1, M2 - transition metals) compounds, the aforementioned problems associated with single transition metal layered oxide structures are significantly reduced while ternary compositions exhibit smooth charge-discharge curves with satisfactory cycling stability and low overvoltage. For instance, Ni and Mn co-substitution of Fe in O3-$NaFeO_2$ effectively suppress capacity fading and iron migration. Therefore, the solid solution of $NaFeO_2$ and $NaNi_{0.5}Mn_{0.5}O_2$ was synthesized to be $NaFe_{0.4}(Ni_{0.5}Mn_{0.5})_{0.6}O_2$ which showed a reversible capacity of 130 mAh g^{-1} within a voltage range of 2.0 - 3.8 V. It was indicated that this cathode material demonstrated smooth charge/discharge curves without considerable voltage hysteresis[82]. In addition to this, the ratio optimization of Ni and Fe with a stable content of Mn of 25% in $NaNi_{0.75-x}Fe_xMn_{0.25}O_2$ where x = 0.4, 0.45, 0.5, and 0.55 showed that the increase in nickel content positively impacts capacity, but have negative effects on cycling and thermal stability[83]. The increase in the number of d-cations can be considered impractical since it makes synthesis and achieving a homogeneous distribution of too many d-cations in the crystal structure challenging. Therefore, ternary systems can be considered to possess a good balance between satisfactory electrochemical performance and the simplicity and reproducibility of synthesis route. Among these, O3-type $NaNi_{1/3}Fe_{1/3}Mn_{1/3}O_2$ is the most widely investigated which demonstrated

130 mAh g^{-1} and stable cycling with the cutoff voltage of 4.0 V vs Na/Na^+. Increasing this cutoff to 4.2 - 4.3 V results in the increased capacity of around 160 mAh g^{-1} because of the presence of high voltage plateau. Nevertheless, this increased potential window leads to rapid degradation of

the structure during cycling. This degradation might be primarily attributed to the hexagonal-to-monoclinic phase transition associated with the migration of d-cations into the Na layer[84,85].

2.5 Conclusion

This chapter provided an in-depth overview of sodium-ion battery (SIB) technology, with a particular focus on cathode materials. Among the various types: polyanionic compounds, Prussian blue analogues, organic materials, and layered transition metal oxides have emerged as the most promising due to their relatively high specific capacity, structural versatility, and compatibility with sodium intercalation. The review also discussed the importance of anionic redox reactions as a strategy to overcome the capacity limitations of conventional cationic redox systems. Lastly, the advantages and challenges of ternary layered oxides, especially Ni-Fe-Mn based compounds, were explored, underlining their potential for high performance and structural stability. These insights form the foundation for the experimental investigations in the following chapters, which aim to improve the electrochemical behavior and long-term viability of layered oxide cathode materials for next-generation SIBs.

CHAPTER 3: Methodology

3.1 Chemicals

The precursors and materials utilized in the synthesis and study of the NNFM and NaMCO materials, with subsequent utilization of the produced powder in the cathode production and half and full cell-batteries are listed in Table 1.

Table 1. The catalog of chemicals used in synthesis of NNFM and NaMCO materials, electrode casting and assembling of the half and full-cells.

Chemicals	Brand	Molecular weight,g/mol	Purity,%	Formula and structure
Sodium Carbonate	Sigma-Aldrich	105.99	99.5	Na_2CO_3
Iron Oxide	Sigma-Aldrich	159.69	96	Fe_2O_3
Manganese Oxide	Sigma-Aldrich	157.87	99	Mn_2O_3
Nickel Oxide	Sigma-Aldrich	74.69	99	NiO
Sodium Nitrate	Sigma-Aldrich	84.99	99.5	$NaNO_3$
Copper Oxide	Sigma-Aldrich	79.55	99	CuO
Manganese Carbonate	Sigma-Aldrich	114.95	99	$MnCO_3$
Solvent NMP	Sigma-Aldrich	99.13	99	C_5H_9NO
Sulfuric Acid	Sigma-Aldrich	98.08	95	H_2SO_4
Nitric Acid	Sigma-Aldrich	63.01	65	HNO_3
Ethanol, anhydrous	Sigma-Aldrich	52.11	99.5	C_2H_5OH
Polyvinylidene fluoride	MTI Corp	64.03		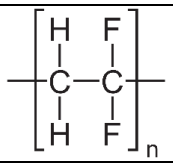
Sodium cubes	Sigma	22.99	99%	Na
Acetylene black	MTI Corp			C
Acetone	Sigma-Aldrich	58.08	99	C3H6O

3.2 Utilized equipment and characterization methods

This section provides a brief description of the equipment and methods used for the

synthesis and characterization of the material and its physical properties.

Mortar and pestle. The mortar and pestle was used in conjunction with acetone for mixing the precursors for synthesis as the first step of the "shake and bake" method and to make slurry after obtaining pure phase cathode material.

Tubular furnace. The International STF 1200 tubular furnace was used to calcine the NMCO. The conditions for the synthesis were at 600 °C with 10 °C min^{-1} heating rate for 5 hours and with a naturally cooling step. The prepared materials were stored in the desiccator.

X-ray diffraction (XRD). The crystalline phase of the materials was studied via XRD analysis on a benchtop MiniFlex instrument from Rigaku Co., Japan. The study was done with Cu Kα radiation in the range of 10 to 70°. Further FullProf program was used for the Rietveld refinement of the data.

Scanning electron microscopy (SEM). The surface morphology of the samples was observed by 5 kV Zeiss Crossbeam 540 SEM (Nazarbayev University).

High-resolution transmission electron microscopy (HRTEM). Key morphological characteristics of crystals was determined using high-resolution transmission electron microscopy with the use of JEM-3010 instrument from JEOL (Sejong University, South Korea).

Energy-dispersive X-ray spectroscopy. Dispersive X-ray analysis was used to further determine the morphology and ascertain elemental composition. The instrument used in this analysis was 7200-H from HORIBA.

Inductively coupled plasma–atomic emission spectroscopy (ICP-AES). The composition of the material was investigated via inductively coupled plasma–atomic emission spectroscopy on Optima 8300, Perkin-Elmer.

X-ray Fluorescence. The analytical method of X-ray Fluorescence was used to confirm the composition of the material with use of PANanalytical (ICGM).

***Operando* XRD.** Deployment of X'Pert from PANanalytical diffractometer was used to examine structural changes during cycling. The angle was set from 14 to 50 ° (2θ).

X-ray absorption spectroscopy (XAS). O K-edge measurements were done in emission mode and K-edge regions for Mn and Cu were performed in the transmission mode on XAS, beamline was set at 8C on Pohang Accelerator Laboratory (PAL) in South Korea. Further data interpretation was done using Athena software.

Glovebox. Half- and full-cells assembling took place inside the MBRAUN glovebox (O_2

and H_2O concentration lower than 0.1 ppm) filled with inert gas.

3.3 Cell configuration and assembly

3.3.1 Electrode preparation

The synthesized cathode materials have been mixed with polyvinylidene fluoride (PVdF) and acetylene black (AB) in an 8:1:1 weight ratio that use NMP (N-methyl-2-pyrrolidone) as the solvent. The consistency of the slurry were adjusted and was applied to aluminium (Al) foil via a doctor blade technique and then dried at 80°C overnight in a vacuum oven. The mass loading of the active material was around 3.5–4 mg cm^{-2}.

3.3.1 Cell assembling process

The half-cell batteries were constructed by assembling CR2032 type coin cells within the MBRAUN glovebox. The assembly of the cell started from the positive cap where the cathode (d=14 mm) was carefully placed and 60 MicroL of electrolyte (0.5 M $NaPF_6$ in (PC) and (FEC) in a ratio of 98:2.) was added dropwise. The wetted cathode was covered with a glass fiber separator and 60 MicroL more electrolyte was added. The sodium disc (d=15 mm) is placed on top of the battery, covered with a negative cap, and finally sealed in the press.

3.4 Electrochemical performance

3.4.1 Galvanostatic charge/discharge cycling

WonAtech BTS battery tester was used to conduct constant current charge/discharge tests. The batteries were cycled at 0.1C and between voltage windows of 1.5 to 4.7 V and 2.0 to 4.4 V.

3.4.2 Rate capability (C-rate)

Rate capability (C-rate) test was conducted via the same instrument as the previous test. The batteries were cycled for 5 cycles at 0.1C, 0.2C, 0.5C, 1.0, 2.0 and 5.0C settings.

3.4.3 Galvanostatic intermittent titration technique (GITT)

The diffusion coefficient was calculated via data obtained from GITT. The tester was programmed to charge and discharge the battery for 5 minutes and relaxed for 5 minutes at the current density of 0.1C.

3.4.4 Electrochemical impedance spectroscopy (EIS)

EIS tests were performed on the coin cells using the following settings: sweep from 100 mHz - 100 kHz at 5 mV amplitude.

3.4.5 *Operando* differential electrochemical mass spectrometry (o-DEMS)

The test was performed using HPR-40 DEMS from Hidden Analytical instrument.

CHAPTER 4: Probing the effect of Cu doping on $Na_{0.62}Cu_xMn_{1-x}O_2$ as cathode material for SIBs

4.1 Introduction

In contrast to Cu-substitution in LIBs, recent studies have shown that layered Mn-based compounds are electrochemically effective in Cu^{2+}/Cu^{3+} redox processes due to their high operating voltage and excellent capacity retention[86]. Given its slightly lower ionic radius (0.73 Å) in relation to sodium (1.02 Å), copper presents an opportunity to serve as a partial replacement for transition metals within the layers of TMO_2[87]. Previous studies, theoretical and experimental, have proposed that the β-phase is stabilized by Cu-doping for Mn in $NaMnO_2$. This substitution promotes Cu to exist in its divalent oxidation state and Mn in its tetravalent oxidation state[88]. Furthermore, instead of the structure deteriorating during high-voltage charging, an anionic redox process can be started in the Na-Cu-Mn-O combination[89]. For example, Zheng et al. investigated the redox activity of oxygen on a layered $Na_{0.67}Cu_{0.28}Mn_{0.72}O_2$ cathode with low voltage hysteresis and indicated that the unbound O 2p states along the Cu-O bond increased the redox activity of oxygen. P2- $Na_{0.67}Cu_{0.28}Mn_{0.72}O_2$ demonstrated a remarkable reversible capacity of 104 mAh g^{-1} with a stable voltage curve, highlighting both cationic and anionic processes[90]. Subsequently, Komaba et al. conducted an in-depth study effectiveness of copper substitution in P′2- and P2-type $Na_{0.67}[Cu_xMn_{1-x}]O_2$, ($0 < x \leq 0.33$), focusing on synergistic distortions of Jan-Teller by Mn^{3+} and Cu^{2+} ions, which includes reversible redox reactions of $Mn^{3+/4+}$, $Cu^{2+/3+}$, and O^{2-}/O^{1-}. A comparison shows that the type of Mn substituent has no effect on the activation of oxygen redox. The structural alterations occur during the charge and discharge processes, influenced by the characteristics and quantity of substituent elements. To avoid O_2 voltage hysteresis, the P2-type $Na_{0.67}[Cu_xMn_{1-x}]O_2$ maintains its P2 phase throughout the bulk and at the final point of the charge (at 4.5 V) without undergoing any extra phases[91].

Previous studies have primarily focused on Cu-substituted sodium layered manganese oxides of type P2, despite the fact that P3-type materials may offer greater environmental sustainability because they can be synthesized at lower temperatures. It is suggested that one of the key factors contributing to the rapid capacity degradation in P3-type materials. The investigation into the effect of Cu-doping on the understanding regarding oxygen redox behavior in P3-type LTMO was conducted by Linnel et al. Over the broad voltage range of 1.8–4.3 V the

$Na_{0.67}Mn_{0.9}Cu_{0.1}O_2$ produced a greater capacity of 176.3 mAh g^{-1}; however, cycling performance decreased significantly and only retained for 71% after 40 cycles. The capacity fading is linked to the transformation of the P3 phase to the P′3 phase when charged to 4.3 V, followed by a complete phase transformation from P′3 to O′3 upon discharge (at 1.8 V)[92]. Nevertheless, the high capacity that the P3-type compound may achieve is still preferred. Although there is ongoing discussion on the intrinsic mechanism, more materials of P3 type with anionic redox activity are being studied.

In this chapter, we examine the influence of partial Cu-doping on the structural and electrochemical behavior of P3-type- $Na_{0.62}Mn_{0.75}Cu_{0.19}O_2$. Building on recent developments in copper-doped layered oxide cathodes, this work aims to understand how Cu incorporation affects phase evolution and redox activity during cycling. A combination of advanced characterization techniques is employed to gain insight into the material's structural dynamics and the nature of cationic and anionic redox processes.

4.2 Experimental section

4.2.1 Material synthesis

A simple solid-state method was used to produce the $Na_{0.62}Cu_xMn_{1-x}O_2$ material. Copper oxide, manganese carbonate and sodium nitrate were were thoroughly mixed in stoichiometric amounts and ground in an agate mortar with acetone for 15-30 minutes. The mixture was subsequently pressed into tablets with a diameter of 20 mm and subjected to calcination in an oxygen atmosphere at 600 °C, applying a heating rate of 10 °C min^{-1} for a duration of 5 hours, followed by a process of natural cooling. The synthesized materials were kept in a vacuum drawer before characterization.

4.2.2 Material characterization

A benchtop type MiniFlex (Rigaku, Nazarbayev University) was utilized to perform X-ray diffraction (XRD) measurements in a 2θ range of 10° to 70°. The FullProf software was used to refine the acquired XRD data. The sample morphology was examined using scanning electron microscopy (SEM) (Crossbeam 540, Zeiss, Core Facilities, Nazarbayev University). The oxidation behavior states of the elements were observed using a NEXSA XPS spectrometer (Core Facilities, Nazarbayev University) fitted with an Al Ka achromatic X-ray source (1486.6 eV). Using energy-

dispersive X-ray spectroscopy (7200-H, HORIBA, Sejong University, South Korea) and high-resolution transmission electron microscopy (HRTEM, JEM-3010, JEOL, Sejong University, South Korea), morphology of crystals and elemental mapping were determined. The chemical compositions of synthesized powders analyzed via using inductively coupled plasma–atomic emission spectroscopy (ICP-AES, Optima 8300, Perkin-Elmer, Sejong University, South Korea) and X-ray Fluorescence (PanAnalytical, ICGM, France). *Operando* XRD was used to conduct structural research while cycling (X'Pert, PANalytical diffractometer, 14–50° (2θ) Sejong University, South Korea). X-ray absorption spectroscopy (XAS) measurements were performed at the 8C beamline of the Pohang Accelerator Laboratory (PAL) in South Korea. Mn and Cu K-edge spectra were collected in transmission mode, while O K-edge data were obtained in fluorescence mode. The collected spectra were processed using the Athena software.

4.2.3 Electrochemical measurements

Polyvinylidene fluoride (PVdF) and acetylene black powders were mixed with powdered $Na_{0.62}Mn_{0.75}Cu_{0.19}O_2$ in an 8:1:1 weight ratio, with N-methyl-2-pyrrolidone (NMP) serving as the solvent. The homogeneous mixture was applied to aluminum (Al) foil using a doctor blade and subsequently dried in a vacuum oven at 80°C overnight. The mass loading of the active material was around 3.5–4 mg cm^{-2}. The synthesized $Na_{0.62}Mn_{0.75}Cu_{0.19}O_2$ electrodes were incorporated with sodium metal serving as the counter electrode within CR2032 coin cells. These cells used glass fiber (AGM) separators and utilized an electrolyte solution with 0.5 M $NaPF_6$ in a volumetric mixture of propylene carbonate (PC) and fluoroethylene carbonate (FEC) in a ratio of 98:2. A WonAtech BTS operating at room temperature was used to apply a steady current of 20 mA g^{-1} throughout a voltage window of 1.5–4.7 V in order to assess electrochemical performance. Measurements using the galvanostatic intermittent titration technique (GITT) were performed with intervals of 5 minutes for charging and discharging, accompanied by relaxation periods of 5 min at a current density of 20 mA g^{-1} (0.1C). Additionally, the HPR-40 DEMS system from Hidden Analytical was used in an R2032 coin cell setup to conduct operando differential electrochemical mass spectrometry (o-DEMS).

4.3 Results and Discussion

4.3.1 Structural and morphological characterizations

A combination of materials $Na_{0.62}Mn_{1-x}Cu_xO_2$ (x=0.0, 0.09, 0.19 and 0.28) doped with copper have been synthesized through a straightforward solid-phase method. To evaluate the chemical composition of the obtained $Na_{0.62}Mn_{1-x}Cu_xO_2$, XRF and ICP-AES analyses were performed. The findings are collected in Table 2-3, which confirms the effective synthesis of the designed materials, demonstrating a precise alignment with the intended chemical composition. It is noteworthy there are differences in the overall metal composition that are not equivalent to one ($Mn + Cu \neq 1$). The observed manganese shortage is likely attributable to the formation of metal vacancies, as are identified within the undoped material system ($Na_{0.62}MnO_2$). In this context, manganese vacancies allow non-bonding 2p oxygen orbitals via oxygen redox processes contributing additional capacity[93].

The crystalline structure and phase composition of $Na_{0.62}Mn_{1-x}Cu_xO_2$ were examined by X-ray diffraction (XRD) patterns and corresponding Rietveld refinements, as illustrated in Fig. 4a and Fig. 5. According to Fig. 4a, the XRD patterns show diffraction peaks that are ascribed to the P3-type layered structure, which is primarily composed to R-3m space group alongside a slight amount of the P1 triclinic phase. This quantitative phase research reveals a proportion of small triclinic to P3 phase is 6.6:93.4%.

Table 2. ICP-AES result of Cu-doped samples.

Sample	Measured atomic ratios		
	Na	Mn	Cu
x=0	0.586	0.959	-
x=0.09	0.644	0.841	0.093
x=0.19	0.655	0.745	0.191
x=0.28	0.654	0.641	0.284

Table 3. Summary of XRF result

Sample	weight % of elements			
	Na	Mn	Cu	O
$Na_{0.62}Mn_{0.75}Cu_{0.19}O_2$	15.22	40.69	12.90	31.181

FullProf software were used to perform Rietveld refinements. Figure 4a distinctly demonstrates that the $Na_{0.62}Mn_{0.75}Cu_{0.19}O_2$ material is devoid of CuO or any other contaminants. The calculated cell indexes for $Na_{0.62}Mn_{0.75}Cu_{0.19}O_2$ were a=2.8807 Å, b=2.8807 Å, and c=16.7313 Å, and comprehensive revised data provided in Tables 4 and 5. The crystal structure scheme (Fig. 4b) illustrates that the oxygen layers adhere to the ABBCCA stacking pattern characteristic of P3-type materials. Among the three designed compounds, $Na_{0.62}Mn_{0.75}Cu_{0.19}O_2$ has been selected for an extensive structural analysis.

Table 4. Lattice parameters obtained by Rietveld refinement as-prepared Cu-doped powders and quantitative phase analysis.

Sample	a(Å)	b(Å)	c(Å)	Ratio of P3:P1 (%)
$Na_{0.62}Cu_{0.09}Mn_{0.9}O_2$	2.8805	2.8805	16.7103	88:12
$Na_{0.62}Cu_{0.19}Mn_{0.75}O_2$	2.8807	2.8807	16.7113	93.4: 6.6
$Na_{0.62}Cu_{0.28}Mn_{0.65}O_2$	2.8903	2.8903	16.749	94.3:5.7

Table 5. Detailed structural parameters as-prepared Cu-doped powders.

Atom	x(Å)	y(Å)	z(Å)	Occup.	B
O1	0	0	0.612/0.62/0.638	1	0.5
O2	0	0	0.388/0.386/0.38	1	0.5
Mn1	0	0	0	0.85/0.75/0.65	0.5
Cu1	0	0	0	0.09/0.19/0.28	0.5
Na1	0	0	0.838/0.839/0.86	1	0.5

The morphology of the synthesized $Na_{0.62}Mn_{0.75}Cu_{0.19}O_2$ was examined using SEM (Fig. 4c). The sample exhibit small irregularly shaped particles (average particle size ~ 0.847 μm Fig.S1) with indistinct boundaries, exhibiting features characteristic of layered materials. The reduced particle size enhances the electrochemical performance by shortening Na^+ diffusion paths and improving particle-to-particle interactions[94]. Despite the non-uniform particle morphology observed at the microscopic level (1 μm), HR-TEM analysis confirms that the internal crystallographic structure retains the characteristic layered configuration of P3-type materials (Fig. 4d). The electrochemical performance is influenced by its ordered structure, which facilitates Na^+ diffusion. The HR-TEM image exhibited a distinct and consistent lattice fringe of 0.553 nm in length. This fringe corresponds with the d-spacing frequency of the (003) sector in the P3 phase, exhibiting strong concordance between the selected area electron diffraction (SAED) pattern. Corresponding planes (003) and (006) are identified by the ring SAED pattern (Fig. 4e), highlighting a connection with structure refinement.

The obtained EDS mappings shown in Fig. 4f reveal a uniform distribution of Na, Cu, Mn and O throughout the bulk phase, supporting that copper has contributed to the crystallization process across the entire component.

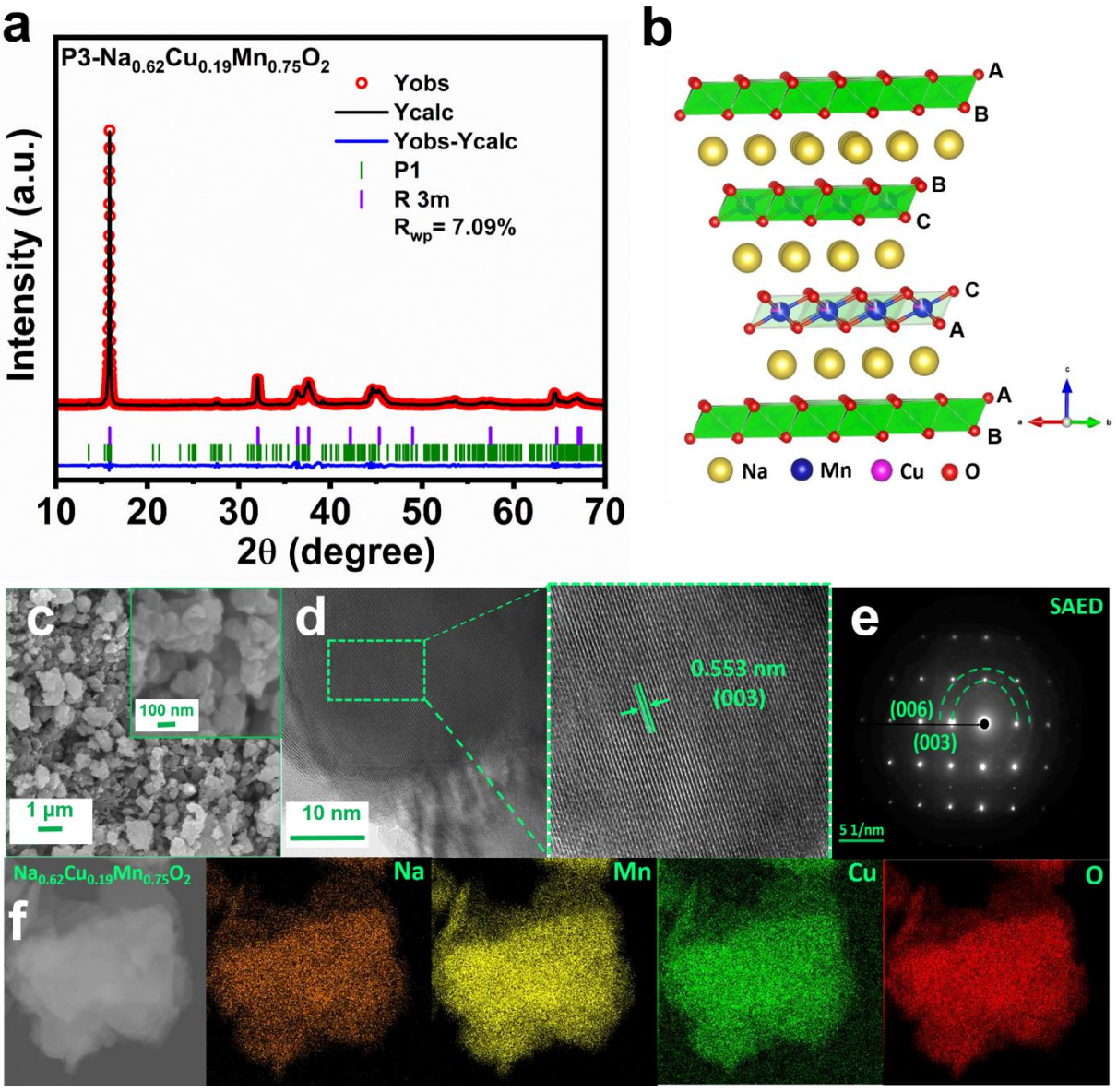

Figure 4. a) XRD Rietveld refinement of $Na_{0.62}Mn_{0.75}Cu_{0.19}O_2$. b) Illustration of crystal structure. c) SEM image of $Na_{0.62}Mn_{0.75}Cu_{0.19}O_2$. d,e) HR-TEM images and SAED pattern of $Na_{0.62}Mn_{0.75}Cu_{0.19}O_2$, f) TEM EDS mapping.

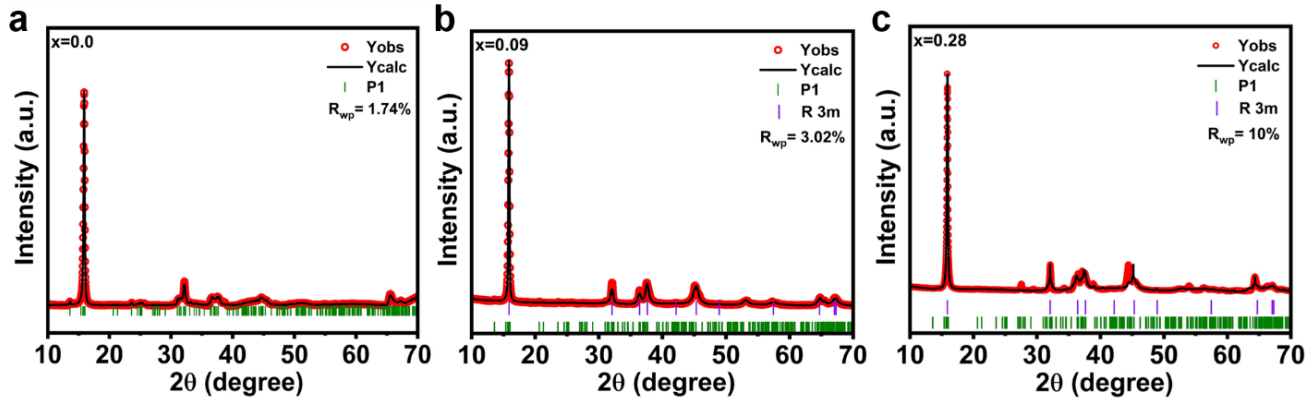

Figure. 5. XRD Rietveld refinement of $Na_{0.62}Mn_{1-x}Cu_xO_2$: a) undoped. b) x=0.09 and c) x=0.28. The refined cell parameters for undoped material were: a=6.6058 Å, b=6.8190 Å, and c = 7.4781Å.

4.3.2 Electrochemical properties

Cu-doped P3-$Na_{0.62}Mn_{1-x}Cu_xO_2$ cathodes electrochemical performance was evaluated at 25°C in a sodium half-cell configuration. Fig. 6a and Fig. S1 illustrate that the cathode materials were assessed within a voltage range of 1.5 to 4.7 V at a constant current density of 20 mA g^{-1} to demonstrate their electrochemical behavior during the initial five cycles. P3-$Na_{0.62}Mn_{0.75}Cu_{0.19}O_2$ demonstrates an initial charge capacity of 148.5 mAh g^{-1} (0.55 Na^+: $Na_{0.86}Mn_{0.75}Cu_{0.19}O_2$) and a higher discharge capacity of 212.2 mAh g^{-1} (0.79 Na^+: $Na_{0.86}Mn_{0.75}Cu_{0.19}O_2$). A significant variation in the voltage profile is observed after the initial cycle. The failure of Mn^{4+} to attain further oxidation states in $Na_{0.62}Mn_{0.75}Cu_{0.19}O_2$ during Na^+ extraction is attributed to a reversible oxygen-redox reactions[93]. However, a slight decrease in capacity was observed over repeated cycles (Fig. 6a). The coexistence of the minor triclinic phase is characterized by intrinsic lattice distortion, which is attributed to Mn-vacancies in the structure that generate internal stress throughout desodiation and sodiation[95,96]. The undoped sample exhibited an initial discharge capacity of 186.14 mAh g^{-1}. However, performance declined rapidly, showing significant capacity loss during the first five cycles (Fig. 6b).

As illustrated in Fig. S2, the differential capacity profiles reveal a significant oxidation peak at 4.5 V, alongside another peak in the range of 3.6-4.2 V. Additionally, there are reversible reduction peaks observed at 3.6-4 V, 3.0 V, and 2.0 V, which correspond to the redox reactions of Mn^{4+}/Mn^{3+}, Cu^{2+}/Cu^{3+}, and O^{2-}/O^n, throughout the initial cycle. Subsequent to the initial cycle,

the dQ/dV profiles exhibited an enormous decrease in peak intensity, indicating more uniform plateaus with reduced distortions. This behavior can be explained by the copper ions present in the crystal structure, which mitigates the Jahn-Teller distortion by decreasing the concentration of Mn^{3+}. Previous research has demonstrated that the inclusion of Cu^{2+} into the structure reduces the amount of Mn^{3+} ions, consequently increasing the quantity of Mn^{4+} to maintain charge balance. The diminished distortion ratio between the Jahn-Teller active (Mn^{3+}, Cu^{2+}) and inactive (Mn^{4+}) species indicates structural stabilization[91].The irreversible oxidation peak at around 4.5 V, as observed in the inset of the dQ/dV graphs, vanished after the fifth cycle. The characteristics of anionic redox processes have been thoroughly examined in layered oxides, focusing on the generation of superoxo and peroxo species during charging. The superoxo-related species is significant due to its instability and propensity to react with the electrolyte solvent, such as propylene carbonate (PC), resulting in parasitic outcomes of solvent degradation that further intensify capacity loss[97–99]. The potential for the oxidation peak at approximately ~ 4.5 V to vanish in subsequent cycles corresponds with these observations.

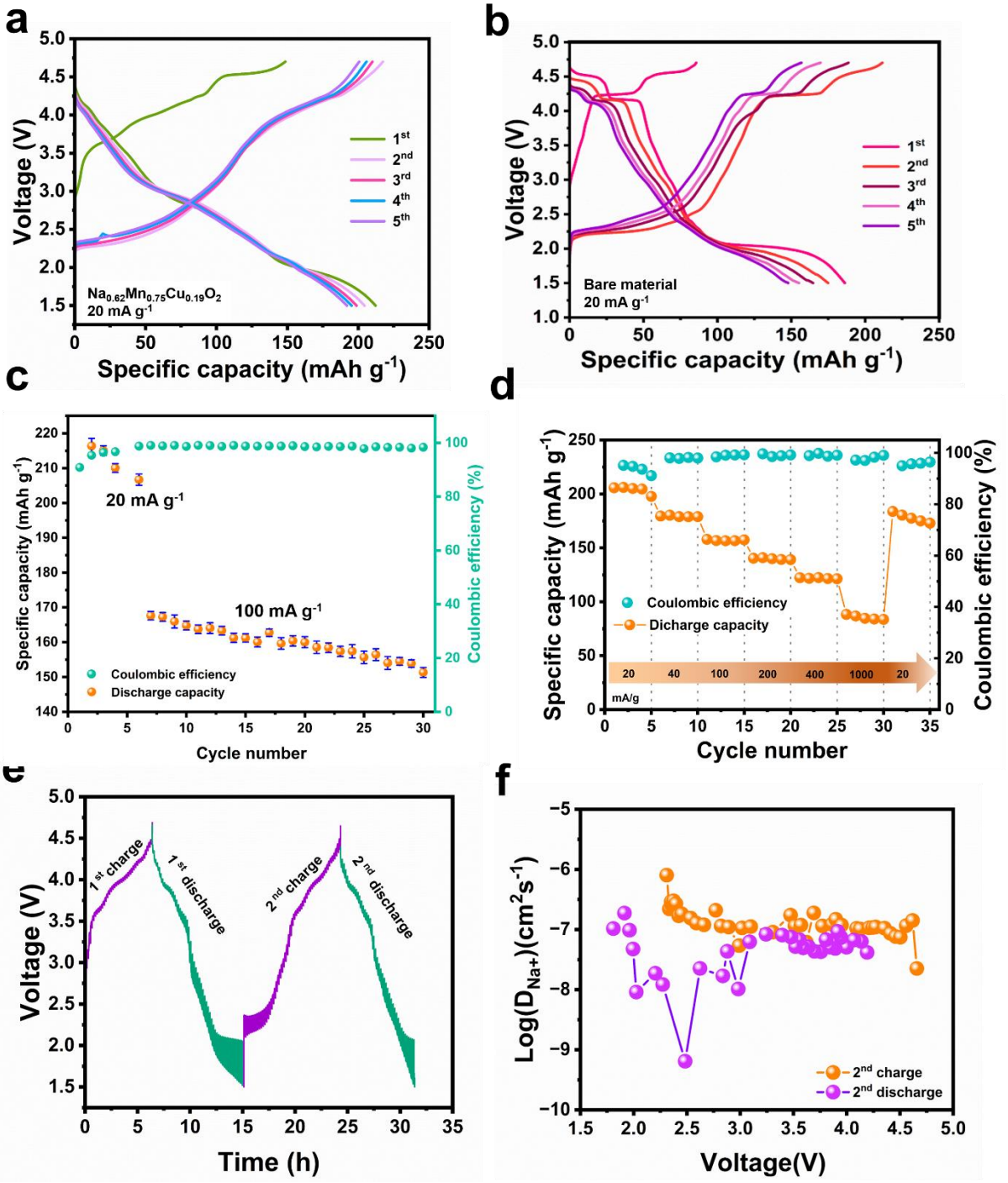

Figure 6. a,b) Voltage profiles of $Na_{0.62}Mn_{0.75}Cu_{0.19}O_2$ and undoped material between voltage range of 1.5-4.7 V. c) Cycling performance at 20 mA g^{-1} and 100 mA g^{-1}. d) Rate capability. e) GITT profiles during the second cycle. f) Variation of the D_{Na+} values.

Fig. 6c displays the cycling performance of P3-$Na_{0.62}Mn_{0.75}Cu_{0.19}O_2$ at rates of 20 mA g^{-1} and 100 mA g^{-1}, correspondingly. Following at low current density 5 cycles of activation, the material demonstrates minor degradation. The material demonstrates favorable cycling performance, exhibiting no significant reduction in capacity after 30 cycles, with a retention capacity of 87%. Fig. 6d presents the analysis and rate capabilities of P3-$Na_{0.62}Mn_{0.75}Cu_{0.19}O_2$ at current densities of 20, 40, 100, 200, 400, and 1000 mA g^{-1}. The capacity varies based on the rate capability result, ranging from 205.8 mAh g^{-1} at a discharge rate of 20 mA g^{-1} to 140.4 mAh g^{-1} at a 200 mA g^{-1}. Despite a high current rate of 1000 mA g^{-1}, the sodium half-cell with the P3-$Na_{0.62}Mn_{0.75}Cu_{0.19}O_2$ cathode retains a reversible capacity of 88.3 mAh g^{-1}. The performance rate indicates a stepwise decrease in capacity with increasing current, followed by a recovery to a high level when the current density reverts to the starting value, demonstrating significant ability for recovery.

The electrodes and the kinetics of Na^+ diffusion in $Na_{0.62}Mn_{0.75}Cu_{0.19}O_2$ were further characterized using the galvanostatic intermittent titration technique (GITT). The cell underwent testing at a constant current density of 20 mA g^{-1} within a voltage range of 1.5 to 4.7 V throughout the second charge/discharge processes (Fig. 6e). The collected data can be utilized in Fick's second law equation to calculate the corresponding sodium ion diffusion coefficients:

$$D_{Na+} = \frac{4}{\tau\pi}\left(\frac{m_B V_M}{M_B A}\right)^2\left(\frac{\Delta E_s}{\Delta E_\tau}\right)^2 \qquad (1)$$

In this context, τ represents pulse duration (s), m_B (g) denotes the active mass of the electrode, V_M (cm^3 mol^{-1}) indicates molar volume, M_B (g mol^{-1}) refers to the molar mass of $Na_{0.62}Mn_{0.75}Cu_{0.19}O_2$, and A ($cm^2$) signifies the surface area of the electrode. With the IR drop (V) excluded, ΔEs and ΔEτ denote the difference between the steady-state potential (V) and the potential change during the current pulse (V), respectively. Fig. 6f presents the calculated diffusion coefficients for Na^+. D_{Na+} values generally ranging from $2.6763*10^{-7}$ to $2.1503*10^{-10}$ cm^2 s^{-1}. A logarithmic transformation is applied to reveal fluctuations in D_{Na+}. Upon the discharge cycle, two distinct regions are observed: one sharp region corresponding to vacancy-cation ordering at approximately 3.0 V, and a weaker region associated with $Mn^{4+/3+}$ at approximately 2.1-2.5 V[99]. But during the charging process, the region remains unidentified. These phenomena can be linked to the absence of polarization exceeding 4.2 V following copper-doping, which inhibits the phase

transition to O3. This is attributed to the high potential polarization associated with the presence of O-type stacking, thereby increasing the Na^+ diffusion barrier. Within the low voltage region, minor polarization may result from the Jahn-Teller-induced phase transferring linked to the rising concentration of Mn^{3+}[93,100].

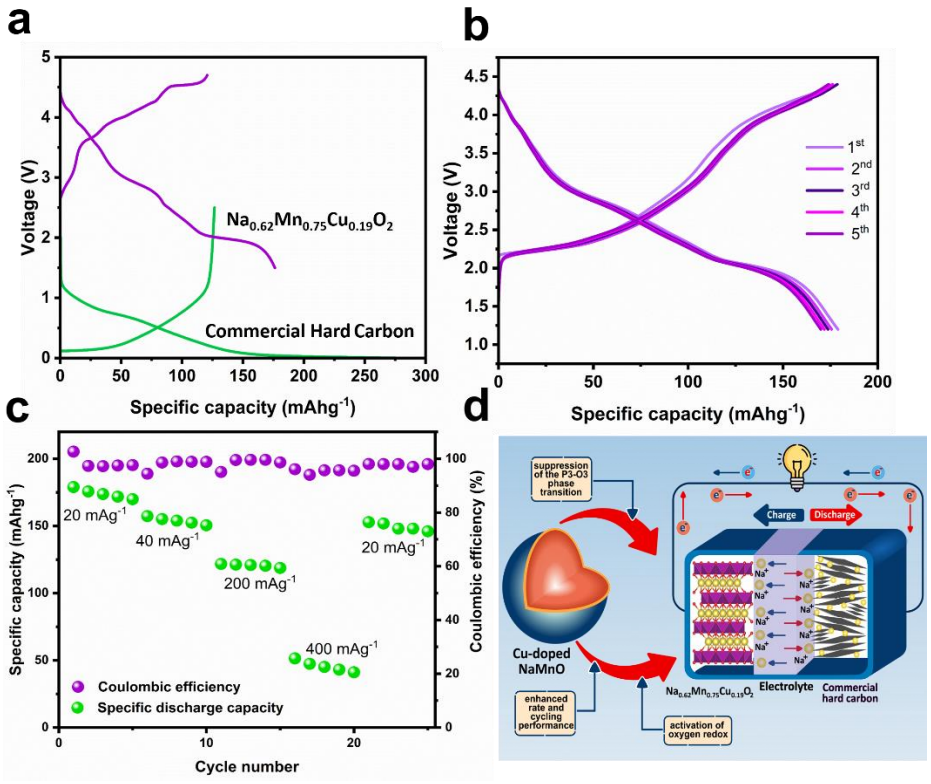

Figure 7. a) The voltage profiles of the $Na_{0.62}Mn_{0.75}Cu_{0.19}O_2$ and commercial hard carbon during first cycle. b) Voltage profile of full cell between 1.2- 4.4 V. c) Rate performance graph of full cell. d) Illustration of the commercial HC and $Na_{0.62}Mn_{0.75}Cu_{0.19}O_2$.

Furthermore, to assess the practical effectiveness of the cathode material, the full cell was constructed utilizing an anode based on commercial hard carbon. Both electrodes underwent pre-cycling for three cycles at a current density of 20 mA g^{-1} to establish stable profiles prior to the assembly of the full cell (Fig. 7a). The optimal N/P ratio, determined by the weights of the cathode and anode, is calculated to be 1.2. During the first cycle at 20 mAh g^{-1}, the full cell demonstrated a significant capacity of 178 mAh g^{-1} at a cut-off voltage range of 1.2-4.4 V (Fig. 7b).The rate performance of the full cell was highlighted across multiple current densities (20, 40, 100, 200,

and 400 mA g^{-1}). At elevated current densities, the full cell capacity consistently attains 50 mAh g^{-1}. Additionally, the full cell continues to exhibit reversible capacity capability (Fig. 7c).

4.3.3 The evolution of structure

To investigate the alteration in oxidation states of synthesized materials during charge-discharge cycles, XANES (Fig. 8) and XPS (Fig. 9 and Fig. S4) analyses were conducted. Fig. 8a presents for P3-$Na_{0.62}Mn_{0.75}Cu_{0.19}O_2$ Cu K-edge spectra alongside a standard reference for the Cu^{2+} oxidation state. The copper in our pristine sample is divalent, as indicated by the comparison with the CuO standard. At a charge of 4.7 V, there is a slight decrease of the Cu K-edge spectra's intensity. A significant change is noted in the shoulder region at approximately 8990 eV. The observed flattening of the shoulder (as indicated by an arrow on Fig. 8a) suggests the oxidation of Cu^{2+} to the Cu^{3+} state[101]. The observed changes in Cu K-edge spectra upon charge can be attributed to the impact of oxygen ligands bonding to Cu metal. The oxidation of O^{2-} leads to diverse Cu-O and O-O lengths of bonds and geometries, potentially affecting the configuration of the Cu K-edge spectrum. The Cu 2p XPS spectra of the pristine material (Fig. 9a) identifies that Cu is 2+ oxidation state. The output signal displays two distinct peaks linked to Cu $2p_{1/3}$ and Cu $2p_{2/3}$ at binding energy levels of 935 eV and 955 eV, respectively, along with characteristic satellites (only one depicted). A minor increase in energy is detected during charging to 4.7 V for $Na_{0.62}Mn_{0.75}Cu_{0.19}O_2$, indicating that Cu^{2+} is oxidized to a higher oxidation state, which aligns with our Cu K-edge XAS data (Fig. 8a). Upon complete discharge to 1.5 V, the peaks revert to the Cu^{2+} state, consistent with observations of the pristine material.

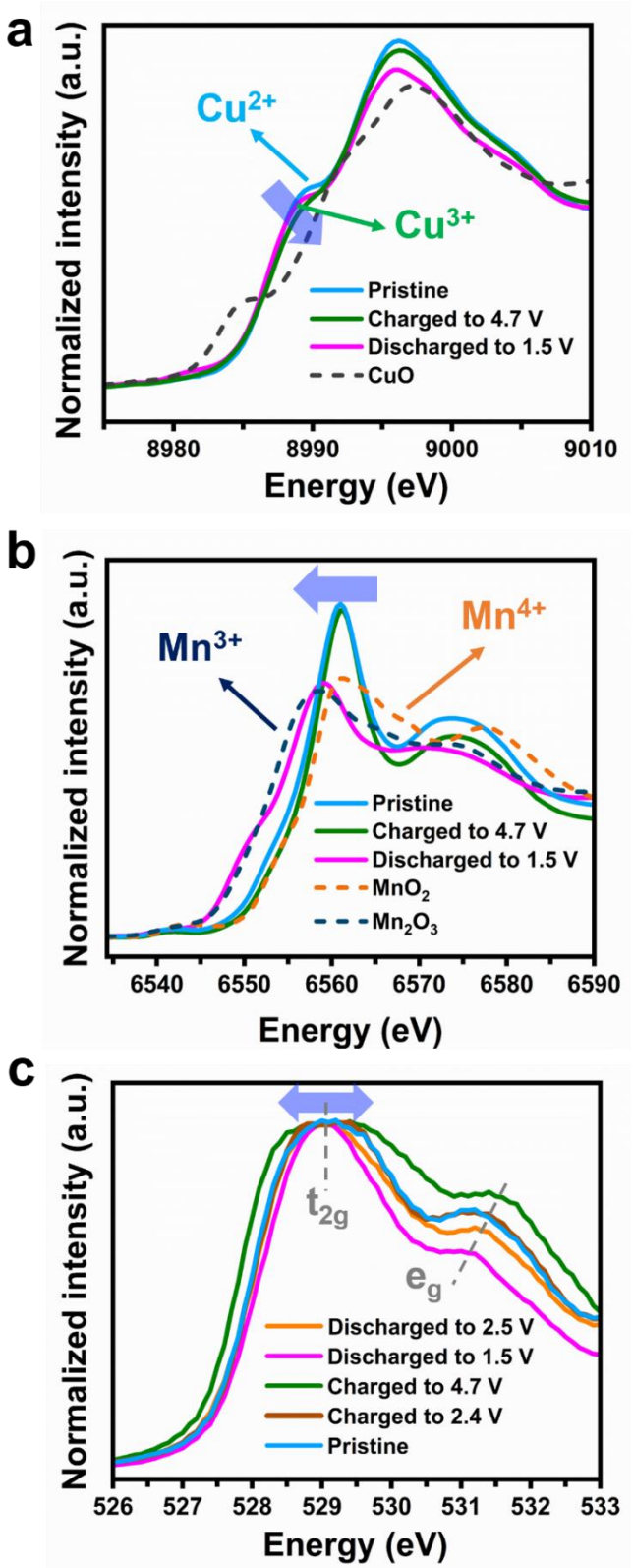

Figure 8. *Ex situ* XANES result of K-edges of a) copper, b) manganese, and c) oxygen.

Fig. 8b presents the collected Mn K-edge spectra for $Na_{0.62}Mn_{0.75}Cu_{0.19}O_2$ alongside standard references for Mn^{3+} and Mn^{4+}. The qualitative contrast among conventional references and the pristine material suggests that the valence state that is present of the latter is roughly tetravalent[100], though it does not precisely correspond to Mn^{4+}. Upon charging to 4.7 V, a subtle shift to higher energies is observed, suggesting the oxidation of a pristine sample to Mn^{4+}. This inference is supported by a comparison with a reference MnO_2 sample. As a result of Mn reduction to the 3+ state and additional Na^+ insertion, the Mn K-edge spectra of the discharged P3-$Na_{0.62}Mn_{0.75}Cu_{0.19}O_2$ moves considerably (approximately 4 eV) to lower energies. Fig. 9b and 9c display the Mn XPS spectra for the P3-$Na_{0.62}Mn_{0.75}Cu_{0.19}O_2$ samples. The energy ranges of X-ray photoelectron spectroscopy for Mn 2p (Fig. 9b) and Mn 3s (Fig. 9c) have been thoroughly examined. Manganese oxidation states are identified by the Mn 3s peaks, where ΔMn 3s decrease as oxidation states rise (4.4 eV < 5.4 eV < 6.1 eV for Mn^{4+}, Mn^{3+}, and Mn^{2+}, respectively). The ΔMn 2p typically exhibits an analogous trend, where a reduced delta signifies elevated oxidation states. Nonetheless, the Mn 2p region exhibits reduced reliability owing to the proximity of doublet peaks corresponding to Mn^{2+}, Mn^{3+}, and Mn^{4+} states. The pristine sample exhibits a ΔMn 3s of approximately 5 eV, indicating simultaneous existence of Mn^{3+} and Mn^{4+} ions. The ΔMn 2p is approximately 11.8 eV, consistent with reported values for MnO_2 (11.8 eV), suggesting the presence of manganese in a tetravalent oxidation state. The XPS spectra of Mn 2p and Mn 3s for the charged state demonstrate the presence of the Mn^{4+} state. A change to lower energies in the Mn 2p peaks upon discharge suggests the presence of Mn^{3+} species.

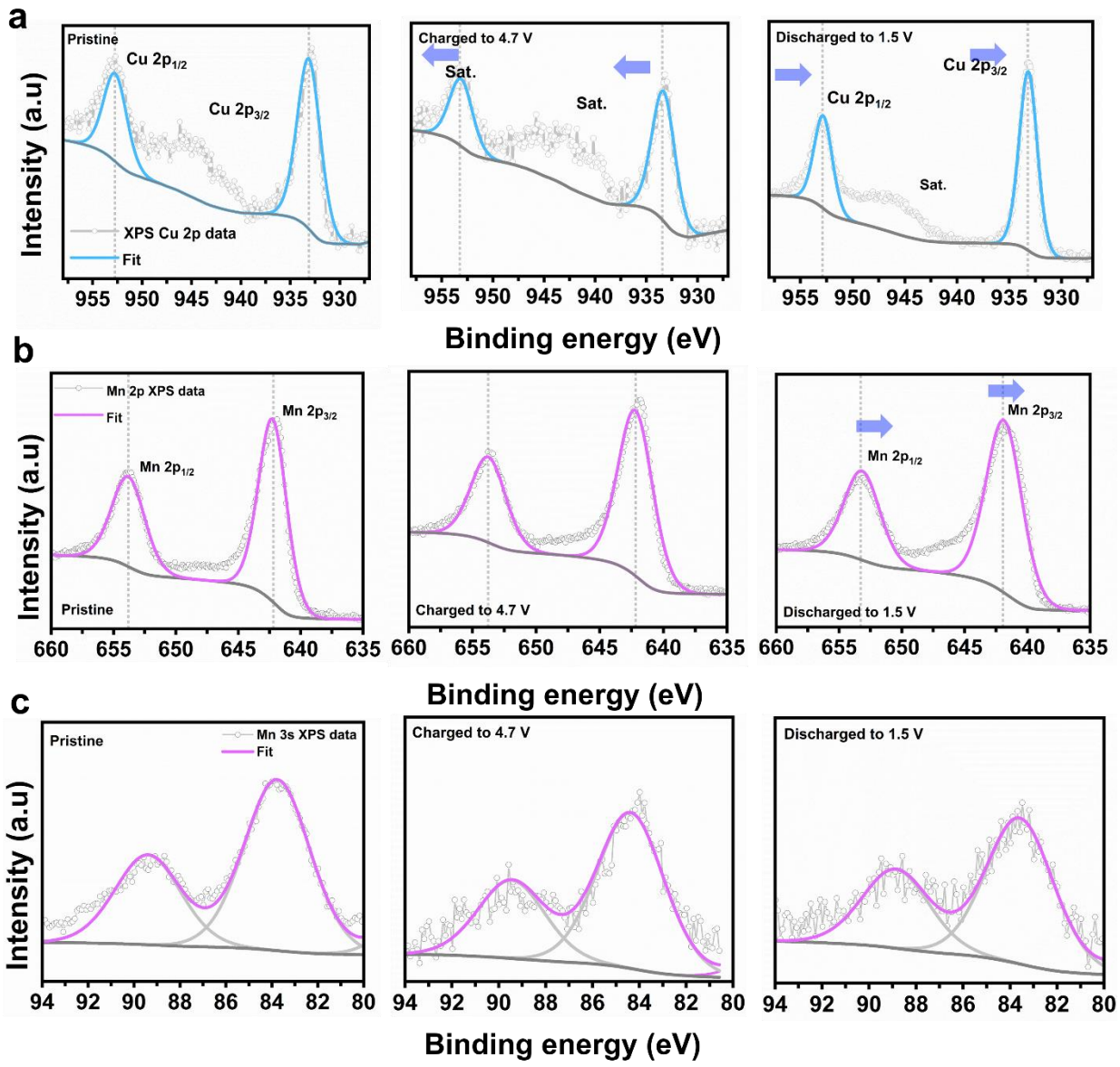

Figure 9. *Ex situ* XPS spectra a) Cu 2p, b) Mn 2p, c) Mn 3s.

Fig. 8c shows the oxygen K-edge spectra of pristine, half-charged, charged, half-discharged, and discharged electrodes. The electronic structure of oxygen redox were analyzed, revealing absorption peaks in the spectra below 533 eV at around 529 and 531.5 eV. The electronic shifts in the O 1s states to the unoccupied hybridized O 2p TM t_{2g} and e_g states can explain the two subsequent peaks[72,92,102]. The spectra exhibit widening, and there is an increase in the intensity of the e_g peak, accompanied by an increase in energy levels when charged to 4.7 V. Upon discharging

to 1.5 V, reverse changes occur, characterized by a general narrowing of the spectra and a decrease in the intensity of the e_g peak, resulting in a shift towards lower energies. These alterations are attributed to a reversible oxygen redox process. Three distinct peaks can be seen in the O 1s XPS spectra of P3-$Na_{0.62}Mn_{0.75}Cu_{0.19}O_2$ (Fig. S4) at its pristine state: the lattice oxygen (O^{2-}) peak at around 530.0 eV, the oxygenated carbonated species (C=O and C−O) at approximately 532.0 eV and 535.0 eV, respectively. Recognized as peroxo-like oxygen (O^{2n-}) appears during the charging process as an additional small peak at ~ 530.4 eV (Fig. S4)[103]. The presence of the latter indicates potential oxygen redox activity during the initial processes of charging[104,105].

Operando differential electrochemical mass spectrometry (DEMS) was utilized to examine the oxygen movement of $Na_{0.62}Mn_{0.75}Cu_{0.19}O_2$ during the charging process. Fig. 10 demonstrates that undetectable O_2 release was observed in the high-voltage area, indicating a lack of significant oxygen evolution. Research results support the hypothesis of a reversible anionic redox mechanism ($O^{2-}/O2^{n-}$); however, they do not rule out the potential for minor structural alterations or other oxygen-related activities that may occur without detectable O_2 evolution. Irreversible oxygen evolution processes ($O^{2-}/O_2^{n-}/O_2$) are frequently observed in sodium layered oxides and are often attributed to the movement of manganese ions and the consequent rearrangement of manganese and vacancies within the TMO_2 planes upon charging[95,106].

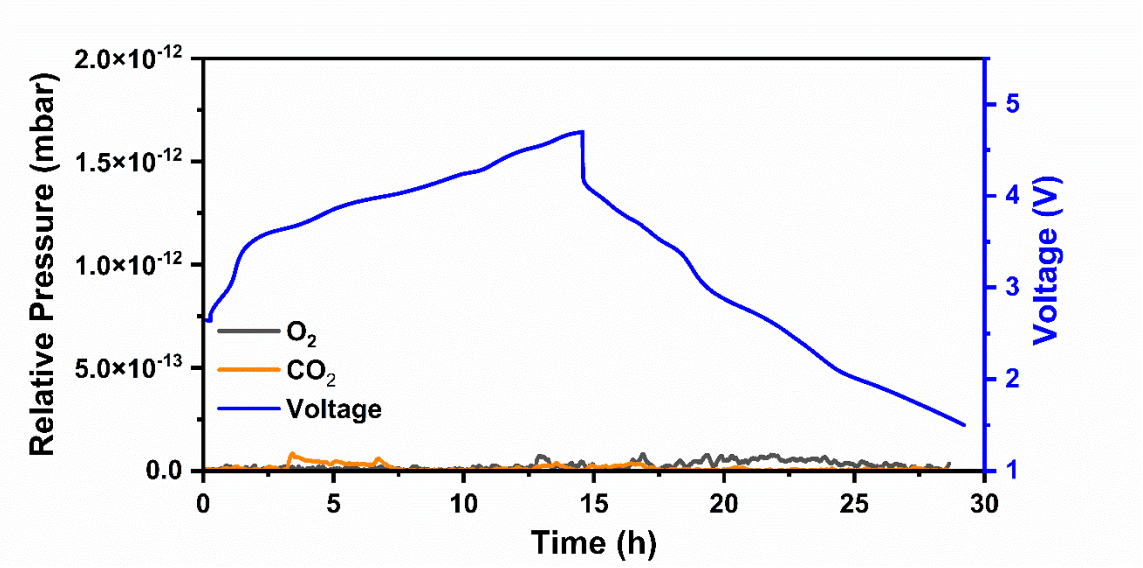

Figure 10. *Operando* DEMS analysis during 1st cycle.

An *in situ* XRD was used to investigate the phase transition and crystal structure evolution of $Na_{0.62}MnO_2$ and $Na_{0.62}Mn_{0.75}Cu_{0.19}O_2$ during the initial Na^+ desodiation/sodiation process between voltage window of 1.5 to 4.7 V. Fig. 11a depicts the evolution of the contoured representation of the structure during the charge-discharge cycles across the right, with the corresponding voltage curve shown on the left. The contour-mapping graph reveals that the initial desodiation step does not cause in the appearance of new peaks, and the P3 layered structure is preserved throughout the entire processes of charge/discharge. Solid-solution behavior is demonstrated by the reported results when charged to 4.7 V and subsequently discharged to 1.5 V. The reversible displacement of the peak locations can be influenced by the relative concentration of sodium[72] . In the initial stages of Na^+ extraction, the (003) and (006) reflection values regularly shift regarding smaller angles, indicating an expansion of the lattice parameter c. As shown in Fig. 11b, the observed trend was validated by computing the fluctuation in lattice parameters throughout the complete charge/discharge process using the least squares approach. This analysis revealed that charging resulted in an increase in the c lattice parameter value, while the a and b parameters decreased. The resulting shift can be reversed after subsequent discharge. The reason for this phenomenon was the increased repulsive contact of oxygen ions between the adjacent layers during the Na^+ deintercalation process[104]. In general, variations in lattice parameters of layered cathodes are affected by displacements in transition metal and metal layers. Removal of sodium from the structure diminishes the shielding effect among the oxygen layers, resulting in increased repulsion and an expanded distance between the layers. A more significant change in the spacing of the sodium layer causes the c lattice parameter to increase during charging, while the a lattice parameter decreases as the volume of the transition metal layer decreases[105]. Simultaneously, the (101) and (012) patterns demonstrate a transition to elevated angles. It is essential to emphasize that the volume change exhibited merely a 1.54% (Fig. 11b). Additionally, the absence of further peaks indicates a significant suppressive effect on phase transitions from the hexagonal P3 phase to the O3 and O3′ phases at elevated voltage. In general, phase transitions in cathode materials are typically linked to anisotropy changes in transition TM-O bonding during charge and discharge. In line with earlier research, strong Cu-O covalence inhibits phase transitions and maintains lattice integrity, promoting the stability of the TM-O structure[107–109].The stabilization of the TMO_2 layer reduces gliding, thereby minimizing volume changes and the generation of stress[109]. Significant shifts of the 15.8° and 32.2° (2θ) peaks towards higher angles

are shown in the XRD result for the undoped electrode (Fig. S5) during the Na^+ extraction in the charging process. The observed alterations indicate a volumetric change due to the gliding of $[\square 1/7Mn6/7]O_2$ layers, as documented in previous studies[95]. This range of voltage corresponds to the Mn^{4+}/Mn^{3+} redox process when discharged to 1.5 V. This implies that structural alterations brought on by the Jahn-Teller distortion, such as phase separation and the creation of biphasic domains, are intimately linked to Mn redox activity. The XRD plots (Fig. S5) further support this mechanism, as the most prominent peaks show a decrease in intensity, while two new peaks emerge, suggesting that the primary peak is becoming unstable and splitting. The observed peaks are ascribed to P'2 phases (Fig. S5)[99,110]. Additionally, *ex-situ* XRD was performed during the initial charge and discharge to further examine the structural evolution. Fig. S6 shows the XRD pattern fresh electrode with distinctive P3 phase peaks. Charging the electrode to 4.7 V reveals that most peaks related to the P3 phase remain detectable. Nevertheless, there is a persistent decline in intensities. This indicates that the increased removal of sodium may lead to a disruption in the atomic arrangement in the lattice[106]. The material was discharged to 1.5 V, and the resulting diffraction patterns revealed a P3 structure phase. *Ex situ* XRD patterns (Fig. S7) facilitate further investigations into the structural development after 30 cycles. It was observed that the structure could be sustained after 30cycles.

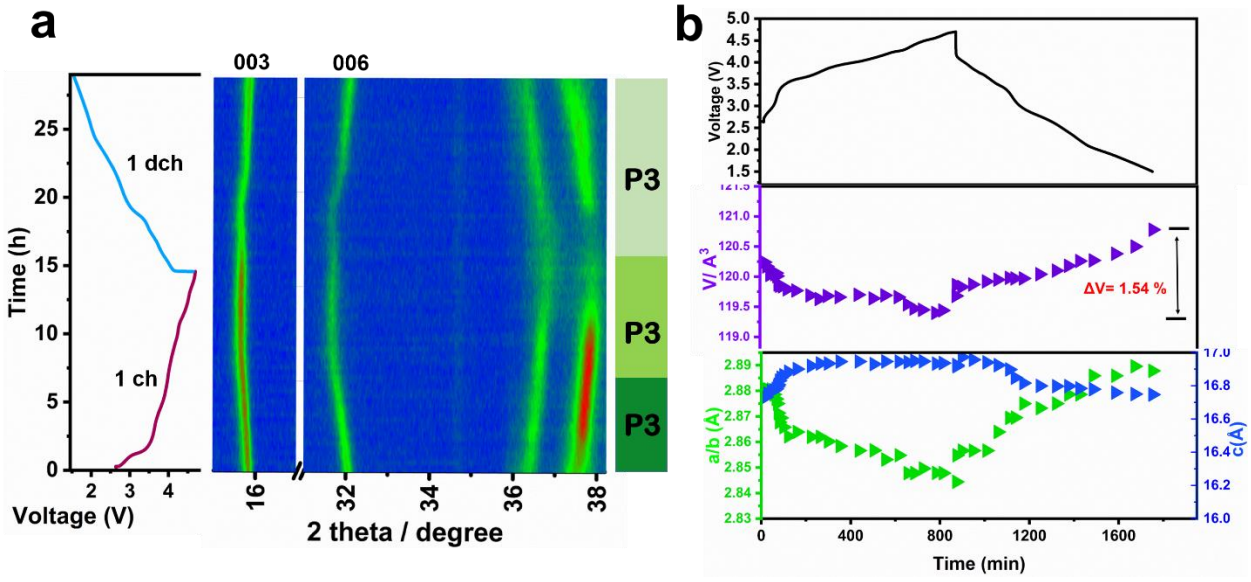

Figure 11. a) *Operando* XRD patterns of the $Na_{0.62}Mn_{0.75}Cu_{0.19}O_2$ during first charge/discharge at 1.5−4.7 V of. b) Lattice parameters variation.

4.4 Conclusion

In conclusion, the material P3-$Na_{0.62}Mn_{0.75}Cu_{0.19}O_2$ shows significant promise as a cathode for SIBs. An initial charge capacity of 143 mAh g^{-1} was achieved, linked to the redox activity of both $Cu^{2+}/^{3+}$ and $O^{2-}/^{n-}$ pairings. Upon discharge, the material demonstrated an impressive capacity surpassing 200 mAh g^{-1}, enabled by the redox pairs $Cu^{3+}/^{2+}$, $Mn^{4+}/^{3+}$, and $O^{2-}/^{n-}$. The redox couples continued to participate in subsequent cycles, ensuring reliable functioning. The strength of these findings was confirmed using a combination of *ex situ* X-ray absorption spectroscopy (XAS), X-ray photoelectron spectroscopy (XPS), and operando differential electrochemical mass spectrometry (DEMS) measurements. The introduction of partial Cu-substitution markedly improved structural stability throughout cycling, as demonstrated by *operando* X-ray diffraction (XRD) data, which reliably showed a single-phase reaction. Furthermore, the substitution of Cu significantly reduced the Jahn-Teller distortion linked to Mn^{3+}, enhancing overall stability. This extensive investigation highlights the significant influence of Cu-doping on the electrochemical functionality of sodium-ion batteries, especially in balancing oxygen redox activities and improving structural integrity.

CHAPTER 5: Ni/Fe/Mn based layered cathode materials for sodium ion batteries

5.1 Introduction

Sodium-ion batteries provide a considerable benefit owing to their affordability. The choice of components for cathode materials needs to emphasize cost-effectiveness, great natural abundance, and availability. Both iron (Fe) and manganese (Mn) are viable alternatives due to their cost-effectiveness and accessibility. Even so, Fe will unavoidably migrate between the sodium layer to the transition metal layer throughout the charge-discharge process, obstructing sodium ion movement and resulting in capacity deterioration[35,111]. The presence of Mn^{3+} induces a significant the Jahn–Teller effect, leading to distortion in the crystal structure and contributing to the irreversible phase change. Numerous studies have shown that even a small amount of Ni can significantly mitigate these drawbacks[112]. Ni-Mn based oxides outperform other layered oxides, but their use is restricted because they undergo irreversible changes in structure and absorb moisture as discussed in the Introduction part. Furthermore, the price of nickel has shown a consistent upward trend annually, potentially resulting in higher raw material expenses. Consequently, optimizing its content is essential, and it is worth exploring the possibility of replacing nickel with more cost-effective elements like Mn and Fe. Considering the excellent electrochemical properties and cost effectiveness, the Ni–Fe–Mn-based materials are progressing rapidly. Recently Yuan developed a series of Fe-substituted $NaNi_{0.5}Mn_{0.5}O_2$ cathode materials, demonstrating that the incorporation of Fe into the Ni-Mn layered oxides effectively softened the MO_2 sliding and Na/vacancy ordering. This led to a reversible O3-P3 phase transformation while increasing the interpolate distance, thereby enhancing ion diffusion. The O3-type $NaFe_{0.2}Mn_{0.4}Ni_{0.4}O_2$ exhibited smoother charge/discharge curves compared with $NaNi_{0.5}Mn_{0.5}O_2$ and showed significantly improved cycling stability, retaining 96.4% of its capacity after 30 cycles in the voltage range of 2.0–4.0 V[113]. Sun et al. additionally noted that boosting the Fe content in Ni–Fe–Mn based materials led to enhanced thermal properties and cycling stability, although there was a minor reduction in the reversible capacity[114]. This finding validates the stabilizing influence of Fe on the crystal structure. Later Guo et al. proposed DFT calculations, that incorporating Fe^{3+}, which possesses a marginally larger ionic radius, into $NaNi_{0.5}Mn_{0.5}O_2$ leads to an expansion of the transition metal layers and promotes electron delocalization. The $NaFe_{0.3}Ni_{0.35}Mn_{0.35}O_2$ compound

experiences a direct O3–P3 phase transformation, maintaining a lack of monoclinic distortion. The capacity retention of $NaFe_{0.3}Ni_{0.35}Mn_{0.35}O_2$ material achieved 80% after 100 cycles at 1C within the 2.0 − 4.0 V voltage range, and the rate performance showed significant improvement. The progress in the commercialization of Ni–Fe–Mn-based materials is rapidly accelerating[115]. Ma's research team accomplished large-scale production using a co-precipitation technique followed by calcination, a method that has gained significant traction for the production of layered oxide cathode materials utilized in lithium-ion batteries[116]. Therefore, it is crucial to properly manage the components and valence states of the elements in the Ni–Fe–Mn based material for its application. Ni–Fe-Mn-based materials typically demonstrate commendable cycling performance; however, notable performance degradation, accompanied by monoclinic structural distortion, frequently arises in the high voltage region (greater than 4.0 V). Additionally, it is necessary to elevate the plateau voltage to achieve enhanced energy density for practical applications. This study focuses on the integration of Mn, Ni, and Fe into the $NaMO_2$ structure to achieve an optimal balance among capacity, cycling performance, and cost-effectiveness. The comprehensive impact of varying concentrations of Fe and Ni, along with Na, on the electrochemical performance and structural alterations of $Na_x(Ni–Fe–Mn)O_2$ remains inadequately explored.

The above-mentioned literature review (in Chapter 2 also) highlights the significance of developing the cathode for SIBs. Taking into account the positive effects of each Ni, Mn, and Fe transition metal, we would like to develop low-cost, environmentally friendly, and high-capacity $Na_x(Ni–Fe–Mn)O_2$ ($Na_xNi_yFe_zMn_{1-(y+z)}O_2$) with novel stoichiometry cathode material for SIBs.

5.2 Experimental section

5.2.1 Material synthesis

The $Na_xNi_yFe_zMn_{1-(y+z)}O_2$ cathode materials were synthesized via solid-state synthesis method by mixing the precursors of Na_2CO_3 (≥ 99.5%, Sigma-Aldrich), NiO (≥ 99%, Sigma-Aldrich), Fe_2O_3 (≥ 99%, Sigma-Aldrich), and Mn_2O_3 (≥ 99%, Sigma-Aldrich) in desirable stoichiometric ratios. The precursors were thoroughly mixed in acetone and uniformly grounded in an agate mortar. Subsequently, the resulting powder mixtures were pressed into a pellet and subjected to calcination in air at 950 ℃ for 12 h, followed by gradual cooling (Fig. 12). The as-prepared samples were stored in a vacuum drawer.

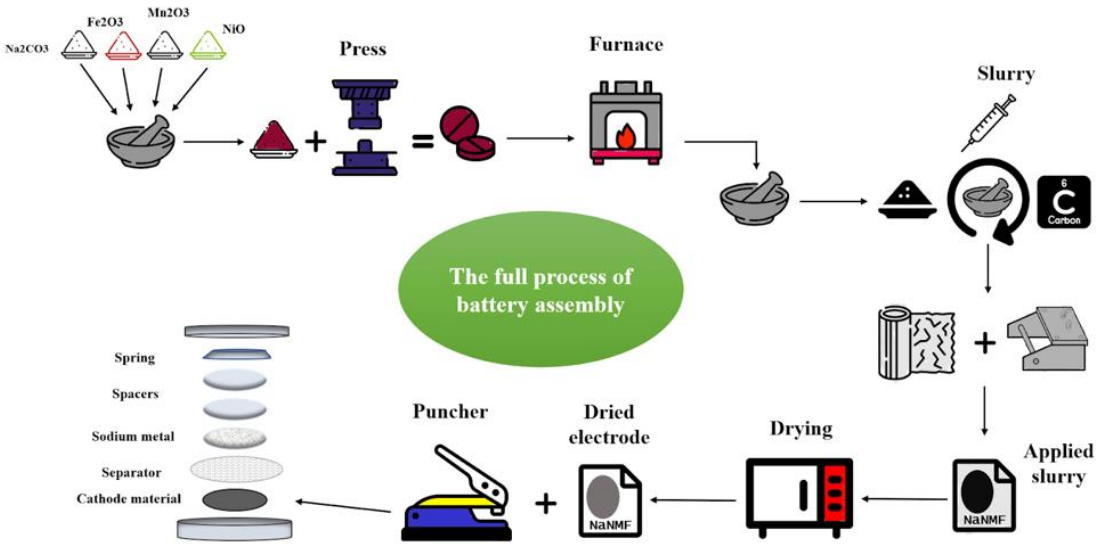

Figure 12. Schematics of the preparation process of the material.

5.2.2 Material characterization

X-ray diffraction measurements were carried out with a benchtop MiniFlex (Rigaku, Nazarbayev University) in a 2θ range of 10 to 70°. The obtained XRD data were refined by FullProf program. The samples morphology were investigated using scanning electron microscopy (Crossbeam 540, Zeiss, Core Facilities, Nazarbayev University). The high-resolution transmission electron microscopy (HRTEM, JEM-3010, JEOL, Sejong University, South Korea) with energy-dispersive X-ray spectroscopy (7200-H, HORIBA, Sejong University, South Korea) was used to determine microstructure and elemental analysis. The valence states of the samples were conducted using NEXSA X-ray photoelectron spectroscopy equipped with an Al Kα radiation (1486.6 eV) (Core Facilities, Nazarbayev University). The compositions of the samples were examined with an inductively coupled plasma-optical emission spectrometer (ICP−OES). Structural evolution after cycling was monitored using XRD (o- XRD, 6 kW, Cu Kα radiation, PANalytical).

5.2.3 Electrochemical measurements

The electrodes were prepared by mixing a slurry of active cathode material (80 wt.%), conductive agent (AB, 10 wt.%) and polyvinylidene fluoride (PVDF, 10 wt%) in N-methyl-2-pyrrolidone (NMP) and casted on aluminum foil. Then the aluminum foil was dried at 80 ℃ in a vacuum oven for 12 h. The mass loading of active materials was about 3-4 mg cm^2. All the electrochemical

performance tests were carried out in CR2032 coin cells. Metallic sodium and glass fibers (AGM) were used as the negative electrode and separator, respectively. The electrolyte solution consists of 0.5 M $NaPF_6$ dissolved in propylene carbonate (PC) with (98:2) fluoroethylene carbonate (FEC). The coin cells were assembled in an Ar-filled glove box (H_2O, O_2 < 0.1 ppm). Galvanostatic charge/discharge measurements were conducted at 25 ℃ using a WonAtech BTS within the voltage range of 2.0 - 4.4 V. The EIS measurements were performed using an electrochemical workstation (Autolab-M204) between 10 mHz to 100 kHz. During the galvanostatic intermittent titration technique (GITT) tests, the cells were charged at 0.1C for 15 min, followed by open-circuit relaxation of 30 min. The Na^+ diffusion coefficient can be calculated according to the following equation: $D_{Na+} = \frac{4}{\tau\pi}(\frac{m_B V_M}{M_B A})^2(\frac{\Delta E_s}{\Delta E_\tau})^2$, where, τ represents pulse duration, m_B (g) denotes the active mass of the electrode, V_M (cm^3 mol^{-1}) indicates molar volume, M_B (g mol^{-1}) refers to the molar mass of $Na_xNi_yFe_zMn_{1-(y+z)}O_2$, and A ($cm^2$) signifies the surface area of the electrode.

5.3 Results and Discussions

5.3.1 Structural and morphological characterizations

Since the solid-state reaction method was utilized for synthesizing the materials followed by high-temperature calcination, as shown in the material synthesis part in detail, the oxidation state of manganese in the $Na_x(Ni–Fe–Mn)O_2$ system was constrained to +4, rendering it a non-active ion. This restriction ensured that the manganese content could be adjusted to 0.4 within the $Na_x(Ni–Fe–Mn)O_2$ framework. As a result, we formulated the targeted compositions using specific transition metal (TM) ratios, normalizing the total TM content to 1 and designated three compositions using the Ni/Fe/Mn ratio for ease of reference in order examine of three TM contents on battery performance: $Na_{0.75}Mn_{0.4}Ni_{0.15}Fe_{0.45}O_2$ (NNFM75), $Na_{0.85}Mn_{0.4}Ni_{0.25}Fe_{0.35}O_2$ (NNFM85), and $Na_{0.95}Mn_{0.4}Ni_{0.35}Fe_{0.25}O_2$ (NNFM95). The atomic composition of all three samples were confirmed by ICP-OES analysis, as shown in Table 6. From the ICP-OES results, the target stoichiometry of all three cathode materials have been achieved.

Table 6. The ICP-OES results of NNFM75, NNFM85 and NNFM95.

Sample	Theoretical formula	Measured atomic ratios			
		Na	Mn	Ni	Fe
NMFN75	$Na_{0.75}Mn_{0.4}Ni_{0.15}Fe_{0.45}O_2$	0.7120	0.4000	0.1503	0.4317
NMFN85	$Na_{0.85}Mn_{0.4}Ni_{0.25}Fe_{0.35}O_2$	0.8403	0.3999	0.2547	0.3424
NMFN95	$Na_{0.85}Mn_{0.4}Ni_{0.35}Fe_{0.25}O_2$	0.9148	0.4000	0.3555	0.2463

Analysis of the X-ray diffraction (XRD) patterns (Fig. 13) confirmed that the predominant phase of the synthesized layered metal oxides was the O3 phase. However, a presence of the P2 phase was detected when the sodium content was set at x = 0.75. In this sample recorded a hexagonal lattice with a mix space group of P63/mmc + R3m and minor NiO impurity. The ratio between phases is determined as 61.7: 23.8: 14.5 respectively. With the increase in Na content, the corresponding peak of the O3 phase shows a continuous upward trend, indicating a total O3 phase fraction. The refinement of the XRD data confirms that samples crystallize in a biphasic P2/O3 and O3-type (R3m) structure with hexagonal symmetries, and detailed crystallographic parameters are specified in Table 7.

Table 7. Rietveld Refinement calculations of lattice parameters of NNFM75, NNFM85 and NNFM95.

Sample	a(Å)	b(Å)	c(Å)	Volume ($Å^3$)	Phase (%)	R_{wp} (%)
NMFN75	2.9507/2.9203	2.9507/2.9203	16.3872/16.7104	123.5670	P2/O3	2.6500
NMFN85	2.9567	2.9567	16.2318	122.8890	O3	1.6900
NMFN95	2.9677	2.9677	16.0480	122.400	O3	2.6600

Table 8. Structure Rietveld Refinement parameters of NNFM75, NNFM85 and NNFM95.

Atom	x(Å)	y(Å)	z(Å)	occup.	B
O1	0	0	0.2685/0.2339	1	0.5
Mn1	0	0	0.0000/0.5000	0.4	0.5
Fe1	0	0	0.0000/0.5000	0.45/0.35/0.25	0.5
Ni1	0	0	0.0000/0.5000	0.15/0.25/35	0.5
Na1	0	0	0.5/0.0000	1	0.5

The lattice parameters of NNFM cathode materials are affected by various competing factors, such as the ionic radius and oxidation state of the metal ions, and M–O bond strength. Table 7 indicates that a decrease in Fe content alongside an increase in Ni results in a modest rise in the lattice parameter *a*, which is associated with the larger ionic radius of the TM ions. Furthermore, the concentration of sodium is essential in influencing the distribution of oxidation states and the spacing between layers, as Na^+ act as a shield between neighboring O_2 layers. An elevated Na content leads to the expansion of the TMO_2 layers, resulting in an increase in the lattice parameter *a*. Nonetheless, it also diminishes the electrostatic repulsion among neighboring O layers, resulting in a reduction of Na layer spacing. The observed reduction in Na layer spacing is considerably more pronounced than the expansion of the TMO_2 layers, leading to a decrease in the lattice parameter c[117,118].

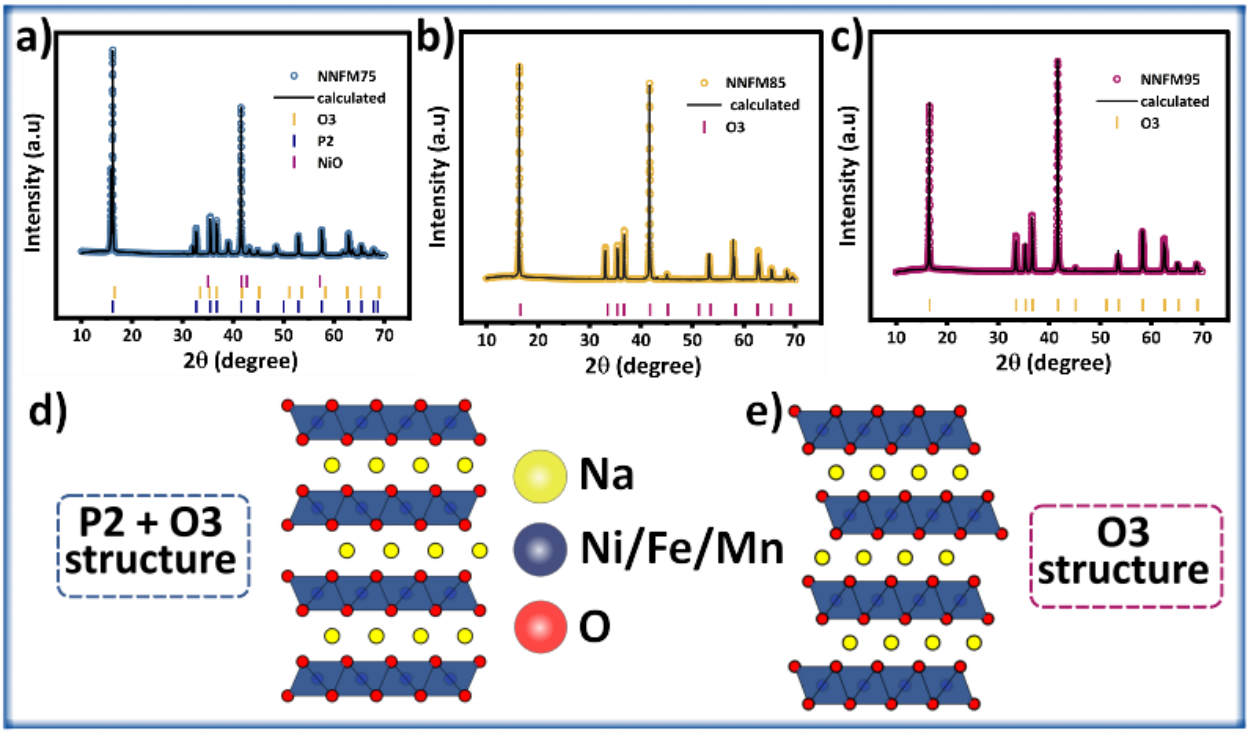

Figure 13. XRD Rietveld Refinement of a) NNFM75, b) NNFM 85, c) NNFM 95, d) Crystal structure of P2/O3 phase. e) O3 phase.

The scanning electron microscopy (SEM) pictures in Fig. 14e and makes it clear that all samples have irregularly plateaued shapes and particle sizes that range from 1 to 2 μm. The samples NNFM85 and NNFM95 display a distinct small nanosheet-like morphology. This nanosheet structure is particularly advantageous for sodium-ion extraction and insertion processes. Because they are, thin and do not put much mechanical stress on them, ions can move through them more quickly. This makes the charge-discharge curves more even. These structural features help make the electrochemical reversibility and cycle stability better[119]. Additionally, HR-TEM images of NNFM75, NNFM85, and NNFM95 are shown in Fig. 14a-c, respectively, which clearly demonstrate the typical layered hexagonal structure. Their corresponding width of 2.74, 2.70, and 2.68 Å stand for the d-spacing values of the (006) plane with R–3m spacing group. These values also have been confirmed by XRD Rietveld analysis. The selected area electron diffraction (SAED) patterns for NMFN95 show the characteristic projected along the (006) zone axis of O3-type structure and give more evidence to hexagonal structure. The energy dispersive spectroscopy

(EDS) images reveal a uniform distribution of five elements within the NNFM95 particle, with no signs of segregation (Fig. 14f).

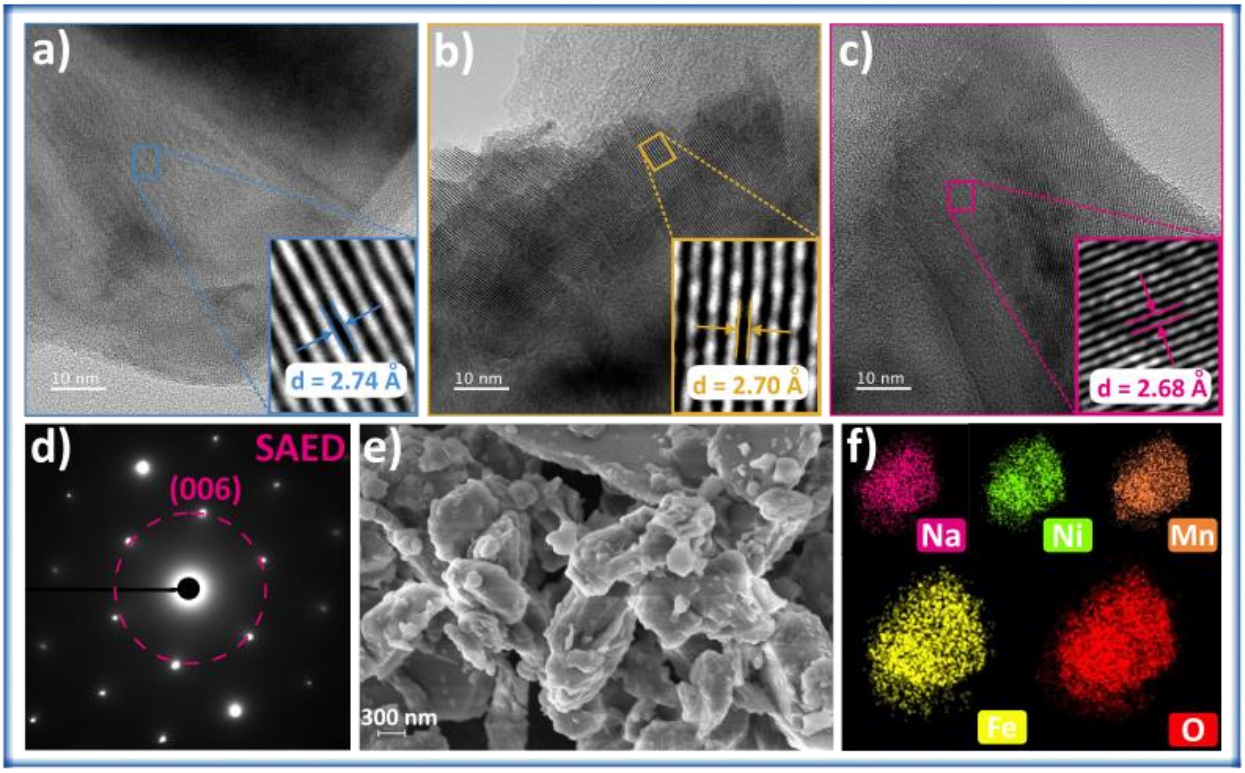

Figure 14. HR-TEM images of a) NNFM75. b) NNFM85. c) NNFM95. d) SAED pattern of NNFM95. e) SEM image. f) EDS mapping of NNFM95.

5.3.2 Electrochemical performance

Using coin-type C2032 cells with metallic sodium as the counter electrode, the electrochemical performance of NNFM75, NNFM85, and NNFM95 were tested within the voltage range of 2.0 - 4.4 V. At a current density of 0.1C, the initial stable discharge specific capacity of NNFM75, NNFM85, and NNFM0.95 was 144.6, 158.98 and 175.7 mAh g^{-1}, respectively (Fig. 15a). After 100 cycles at 100 mA g^{-1}, the discharge capacity of NNFM75 was 103.67 mAh g^{-1}, with a capacity retention of 72%; NNFM85 exhibited a discharge capacity of 113.57 mAh g^{-1}, with capacity retention of 73%; and NNFM95 displayed a discharge specific capacity of 125.5 mAh g^{-1}, with 76% capacity retention. All three cathode materials demonstrated stable coulombic efficiency at around 98–99% after initial cycles. These results suggest that capacity of the cathode materials varies considerably with changes in Ni, Fe, and Na contents. As Ni content increases (from 0.15 in NNFM to 0.35 in NNFM95) with corresponding Fe content decreasing, the average

voltage shifts higher, and the specific capacity increases significantly. Similarly, with an increase in Na content (from 0.75 to 0.95), the specific discharge capacity enhances. In addition to improved capacity, the capacity retention follows the same trend. NNFM95 shows the highest retention, maintaining its performance over extended cycling, while NNFM85 and NNFM75 exhibit intermediate retention and the lowest capacity retention, respectively. Furthermore, a series of charge-discharge tests were conducted across varying current densities ranging from 0.3C to 5C to examine the rate capabilities of the three cathode materials, as demonstrated in Fig. 15c. It can be observed that the difference in capacities is more obvious at 5C. Upon returning to a current density of 0.3C, the specific discharge capacities of NNFM75, NNFM85, and NNFM95 returned to near initial values.

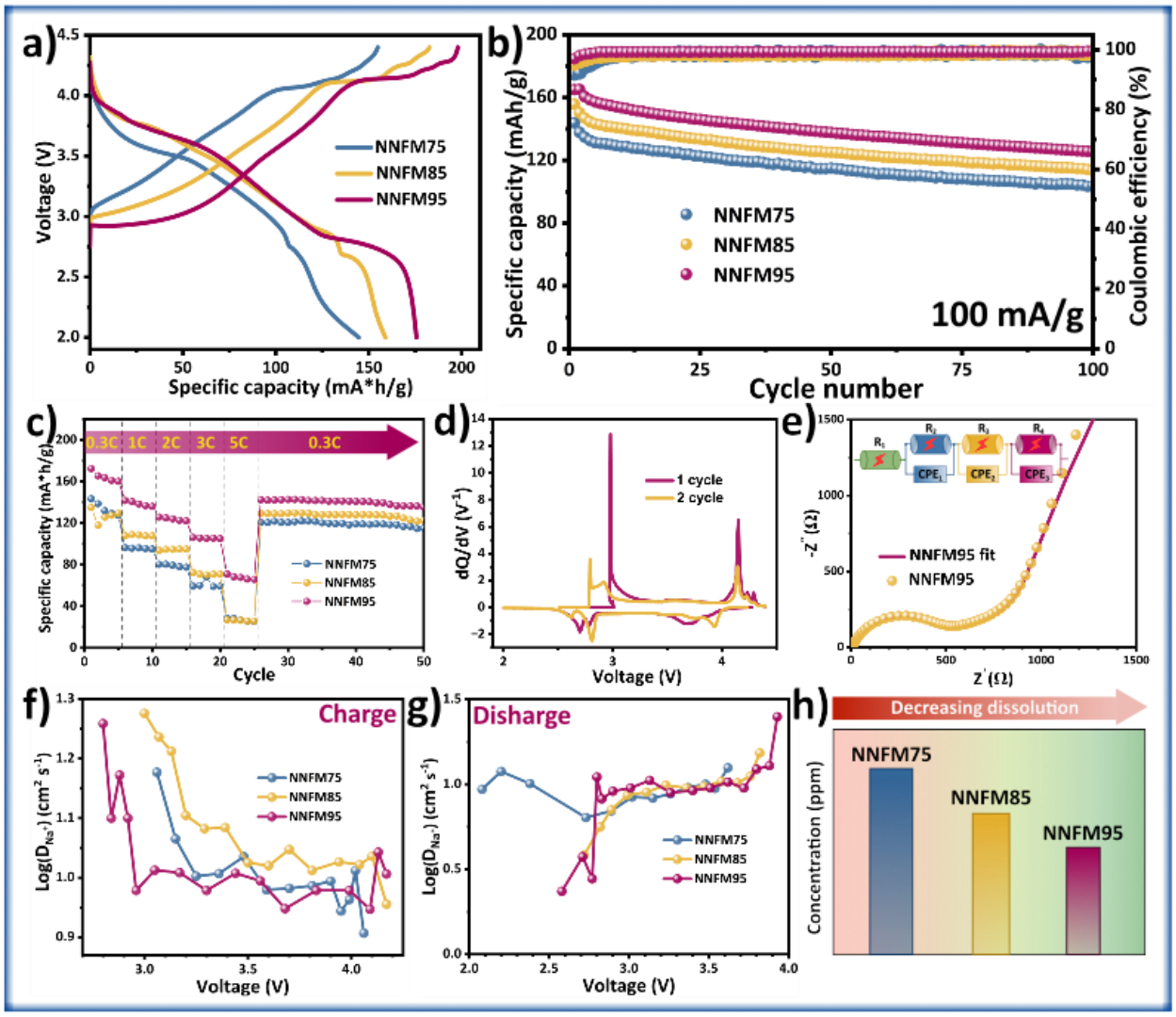

Figure 15. Electrochemical properties of a) charge/discharge profile. b) Cycling performance. c) c-rate. d) dQ/dV profile. e) EIS spectra (Nyquist plots) of NNFM95. f-g) The calculated $D_{coefficient}$. h) Illustration of Mn dissolution result.

The galvanostatic intermittent titration technique (GITT) was performed to investigate the Na^+ diffusion kinetics. The results of the second cycle (Fig. 15 f-g) offer valuable insights into the diffusion behavior of Na^+ and the dynamics of phase transitions in the samples under investigation. The observed D_{Na+} values are linked to the plateau region that is related to phase transitions and lattice rearrangements[120]. The findings suggest that a reduction in Na content leads to a decrease in the negative impacts associated with phase transitions and lattice rearrangements. In particular, the phase transition is smoother in NNFM75, O3–P3 phase transition mild in

NNFM85, and more pronounced in NNFM95.Throughout the discharging process, the overall trend remains consistent. Furthermore, the Na^+ diffusion coefficient for O3-NNFM85 and NNFM95 was found to be 8.02 $*10^{-8}$ cm^2 s^{-1}, which significantly surpasses that of P2/O3-NNFM75 (1.57 $*10^{-10}$ cm^2 s^{-1}). This underscores the improved ionic transport characteristics of the optimized composition.

The investigation of charge transfer at the electrodes was conducted using electrochemical impedance spectroscopy (EIS), with the results illustrated in Fig. 15e. A corresponding circuit was created to examine the conditions of the cycled electrodes (inset Fig. 15e). The charge transfer resistance in NNFM95 seems to be elevated compared to other samples. This phenomenon is justifiable, considering that the reaction activity is markedly elevated, as demonstrated by the GITT results.

5.3.3 Structural evolution

The investigation into the cycling stability mechanism involves collecting *ex situ* XRD patterns at specific voltage points throughout the first charge and discharge. This data is utilized to analyze the phase transformations of NNFM75, NNFM85 and NNFM95 (Fig. 16a–c). Upon charging to 3.6 V, the distinctive (003)/(006)/(104) diffraction peaks of the O3 phase in NNFM75 disintegrate, while new diffraction peaks develop at 31.9° (006) and 46.5° (015), signifying an O3–P3 phase change. The peak positions of (003) P3 and (002) P2 are remarkably similar, complicating the differentiation of these phases based only on their XRD patterns. The heightened peak intensity at 15.5° unequivocally indicates the formation of the P3 phase. Once charge progresses to 4.4 V, the (002) P2 and (003) P3 diffraction peaks progressively diminish, while a new broad diffraction peak appears around 16.0°, indicating that both the P2 and P3 phases experience additional phase transitions. The (002) P2 and (003) P3 peaks ultimately disappear entirely, while the broad diffraction peak relocates to 16.3°. P2-type oxides are known to commonly experience an OP4 phase change. The recently established broad peaks at 16.3° are accurately indexed to OP2 and OP4 phases, signifying that the P2 phase transforms to a P2–OP4 structure, whilst the P3 phase experiences a P3–OP2 transformation[121]. This phase can be described as the OP2 structure that has octahedral and prismatic layers stacked in different ways along the c-axis, as reported in work of Yabuuchi et al[122]. Throughout the discharge process, at

3.2 V the broad diffraction peak progressively diminishes, while the (002) P2 and (003) P3 peaks emerge once more, signifying the shift of the OP4 phase reverting to the P2 phase and the OP2 phase reverting to the P3 phase. As the discharge continues to 2.0 V, the diffraction peaks associated with the O3 phase gradually reappear, while the peaks of the P3 phase decrease, indicating a full return to the original structural state. Therefore, the structural changes of P2/O3-NNFM75 can be outlined as follows: P2/O3→P2/P3→OP2/OP4→P2/P3→P2/O3.

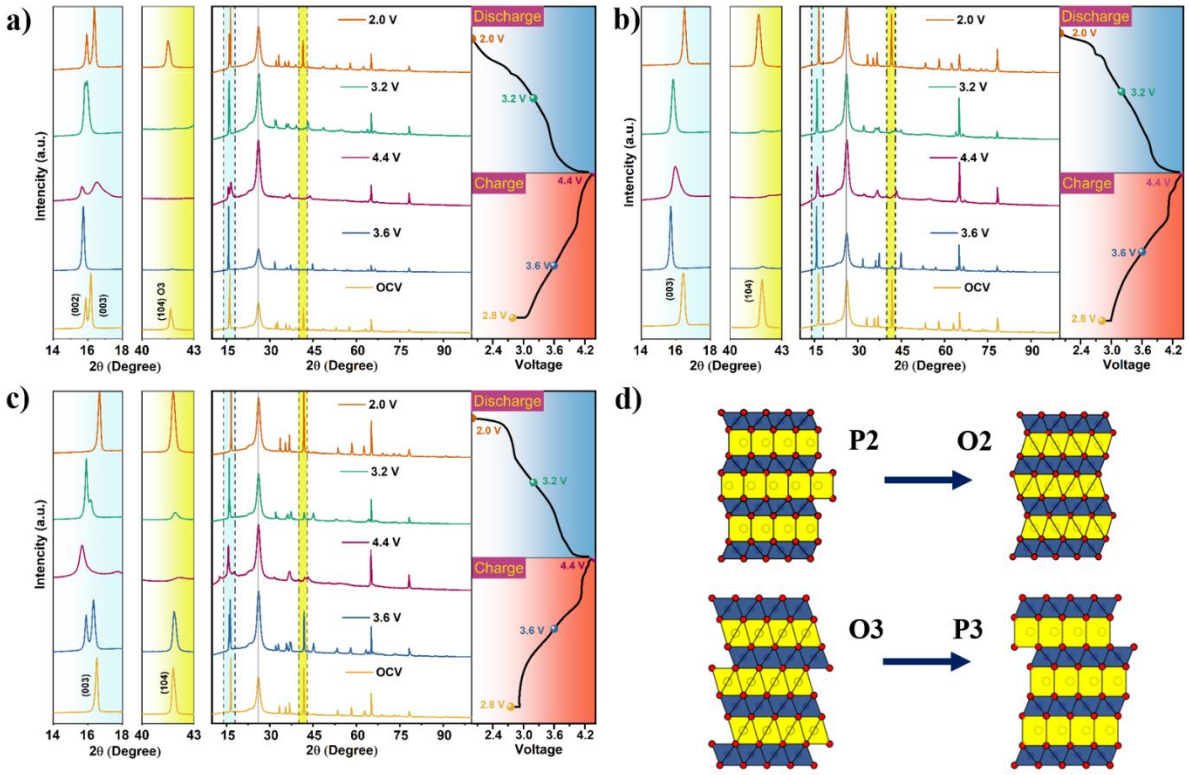

Figure 16. *Ex-situ* XRD pattern of a) NNFM75. b) NNFM85. c) NNFM95. d) Crystal structure changes.

In NNFM85, upon charging to 3.6 V, the (003) peak of the O3 phase exhibits a shifting accompanied by the emergence of a new set of diffraction peaks that are characteristic of the hexagonal P3 phase at lower angles. In addition, new peaks appear at 31.9° and 46.9°, whereas the (104) O3 peak decreases, suggesting a two-phase reaction characterized by the coexistence of O3 and P3 phases. Further the charging till 4.4V, the intensity of the (003) P3 peak rises, whereas the

(003) O3 and (104) O3 peaks diminish entirely, resulting in the presence of only diffraction lines that correspond to the hexagonal P3 phase, with no additional peaks observed. Following discharge, the XRD pattern exhibits a precisely inverse trend, with the sharp and well-defined peaks of the O3 phase returning entirely to their original positions following a complete cycle. The findings indicate that the O3–P3 phase transition exhibits complete reversibility. In the same way, the NNFM95 samples demonstrated a comparable pattern; however, at 3.6 V, the electrode exhibited a peak splitting at around 15.7° (2θ). The principal distinctive peak of the O3 phase retained at this stage. The observed result could have ascribed to experimental errors, wherein the battery was not immediately detached from the tester upon reaching 3.6 V, thereby permitting a transient unintentional voltage surge exceeding the established threshold. Such aberrations may have affected the phase behavior evident in the XRD patterns.

An additional significant factor that leads to the structure breakdown of Mn-based layered oxides during cycling is the dissolution of Mn[123]. To find out how much Mn is being dissolved, an ICP-OES test is used to measure the Mn ratio in the cathode electrodes after the first charge (Fig. 15h). We can observed that NNFM95 has the lower molar ratio of Mn, which means that a few Mn is dissolving. The highest Mn ratio identifies that Mn is dissolving very quickly in other samples, which could be linked to the many microcracks from literature[124].

5.4 Conclusion

This chapter presents the successful synthesis and characterization of a series of ($Na_xNi_yFe_zMn_{1-(y+z)}O_2$) cathode materials, emphasizing the investigation of their electrochemical performance and structural evolution as it pertains to sodium content. The investigation demonstrated that different sodium concentrations (x = 0.75, 0.85, and 0.95) led to the development of biphasic (P2/O3) and pure O3-type materials. The NNFM95 sample demonstrated the most encouraging electrochemical performance among these options. EIS and GITT analyses revealed that optimizing sodium content effectively lowers charge transfer resistance and markedly improves Na^+ ion diffusion kinetics. The *ex situ* XRD analysis provided additional confirmation of the reversible O3–P3 phase transition occurring during charge-discharge cycles, demonstrating structural integrity without any irreversible degradation. Furthermore, the dynamics of phase transformation underscored the importance of a precisely balanced composition of Fe, Ni, and Mn

in preserving structural integrity and improving cycling performance. The results offer significant insights into the design and enhancement of high-performance cathode materials for sodium-ion batteries, highlighting advancements in energy density, cycling stability, and potential for commercial application. The following chapter will explore the electronic structure and intricate structural evolution of these materials, employing advanced characterization techniques to clarify the mechanisms that influence their performance.

CHAPTER 6: Advances in O3- $Na_{0.95}Ni_{0.35}Mn_{0.4}Fe_{0.25}O_2$ cathode development for SIBs.

6.1 Introduction

The incorporation of various transition metals in Na-layered oxides has attracted significant attention due to its ability to stabilize voltage profiles, enhance average operating voltage, increase reversible capacity, and prevent complex phase transformations. O3-structured $Na_x(Ni–Fe–Mn)O_2$ cathodes, utilizing cost-effective and environmentally friendly elements like Mn and Fe, have emerged as promising options for next-generation sodium-ion batteries, as discussed in Chapter 5. Through the systematic regulation of transition metal ratios, these materials effectively address phase transitions, reduce electrolyte degradation, and minimize capacity fading, which are common issues in single-transition-metal cathodes. This section delves deeper into the findings presented in the previous chapter, providing a more comprehensive analysis related to the multi-transition metal oxide cathode, $Na_{0.95}Mn_{0.4}Fe_{0.25}Ni_{0.35}O_2$.

Through careful compositional adjustments, $Na_{0.95}Mn_{0.4}Fe_{0.25}Ni_{0.35}O_2$ must tackle the limitations of its constituent elements, achieving a cohesive performance in terms of capacity retention and extended cycling durability. This chapter serves as a continuation of the previous section, focusing on in-depth characterization methods, including X-ray Absorption Spectroscopy (XAS), Mössbauer spectroscopy, and *operando* XRD. The aim is to provide detailed insights into electronic structure, phase transitions, charge compensation mechanisms, and iron migration, which are essential for understanding and improving the stability of Fe-containing sodium-layered oxides as discussed in Chapter 2.

6.2 Experimental section

6.2.1 Material characterization

Structural analysis during charging/discharging were analyzed using *operando* XRD (X'Pert, PANalytical diffractometer, 14–50° (2θ) Sejong University, South Korea). XAS analyses for the Mn and Fi and Ni K-edge regions were performed in a transmission mode, and the O K-edge measurements in a fluorescence mode at the 8C beamline (Pohang Accelerator Laboratory (PAL), South Korea). The obtained XAS data were analyzed using the Athena. *In situ* Mössbauer spectra (Transmission ^{57}Fe) were obtained at room temperature using a constant acceleration the

method using a ^{57}Co:Rh source. The preparation of the Mössbauer absorbers involved using cathode materials in the range of 40 mg cm^{-2}. The isomer shifts are reported relative to Fe metal at room temperature.

6.3 Results and discussion

The redox process behavior and the changes in local structure during Na^+ extraction/insertion in $Na_{0.95}Mn_{0.4}Fe_{0.25}Ni_{0.35}O_2$ were examined using *ex situ* XANES for Mn, Fe, Ni, and O K-edges during the first charge-discharge (Fig. 17). The FT magnitudes along with their EXAFS fits are presented in Fig.18. The two pronounced peaks in the Mn, Ni and Fe K-edges are detected within the range of 1–3 Å. The initial peak located at approximately 1.5 Å is linked with TM–O_6 correlations in the initial shell, whereas the subsequent peak at roughly 2.6 Å is associated with the follow-up shell TM–TM_6 across the ab plane. Generally, the K-edge XANES spectra for Fe and Ni exhibit a consistent trend where the average oxidation states of the transition metals rise during the charging process, followed by a shift toward a lower energy level during the discharge. The XANES spectra for Mn K-edge in Fig. 17a do not indicate the shift of the absorption edge for pristine, charged and discharged samples. However, the shift of ~ 2eV on the top of the absorption edge is observed as indicated by dashed lines. Still the Mn in $Na_{0.95}Mn_{0.4}Fe_{0.25}Ni_{0.35}O_2$ is in Mn^{4+} state as shown by the comparison with reference MnO_2 sample. The Mn^{3+} lies to significantly lower energies from Mn^{4+}. EXAFS spectra of the Mn K-edge reveal that minor fluctuations in the Mn–O interatomic distance result from alterations within the local environment, impacted by the presence of Ni or Fe. This is attributed to recognize that all TM ions occupy octahedral sites and are distributed at random in O3 layered structure. XPS analysis of pristine (Fig. S8a) $Na_{0.95}Mn_{0.4}Fe_{0.25}Ni_{0.35}O_2$ confirms the results of Mn K-edge XAS, and indicates the presence of Mn in 4+ oxidation state. Both Mn2p and Mn3s energy ranges have been probed. Generally, Mn3s peaks are used to identify the oxidation states of Mn, with ΔMn3s decreasing with rising oxidation states (4.4 eV < 5.4 eV < 6.1 eV for Mn^{4+}, Mn^{3+}, Mn^{2+}, respectively). The ΔMn2p is also used to assign the oxidation state of Mn, and our value of ~11.5 eV is close to the reported values for MnO_2 (11.8 eV) (Fig. S8b).

Ni K-edge XAS indicate a significant shift ~3 eV of the absorption edge from pristine to charged states. Upon discharging the spectrum returns back to pristine state. Ni is in 2+ oxidation state in pristine and discharged samples as deduced from the comparison with NiO spectrum. In

the charged sample the oxidation state increases, indicating Ni^{3+}, which is the Jahn-Teller active state. The EXAFS spectra (Fig. 18b) reveal a reduction in both the interatomic distance of Ft magnitude and Ni-O as Na^{+} is extracted during the initial charge, signifying a rise in the oxidation state of the Ni ion from 2+ to 3+. The presence of an effective the Jahn-Teller Ni^{3+} ion may result in a reduction of the intensity within the first coordination shell[84]. XPS analysis of pristine $Na_{0.95}Mn_{0.4}Fe_{0.25}Ni_{0.35}O_2$ confirms the results of Ni K-edge XAS, and indicates the presence of Ni in 2+ oxidation state (Fig. S8c).

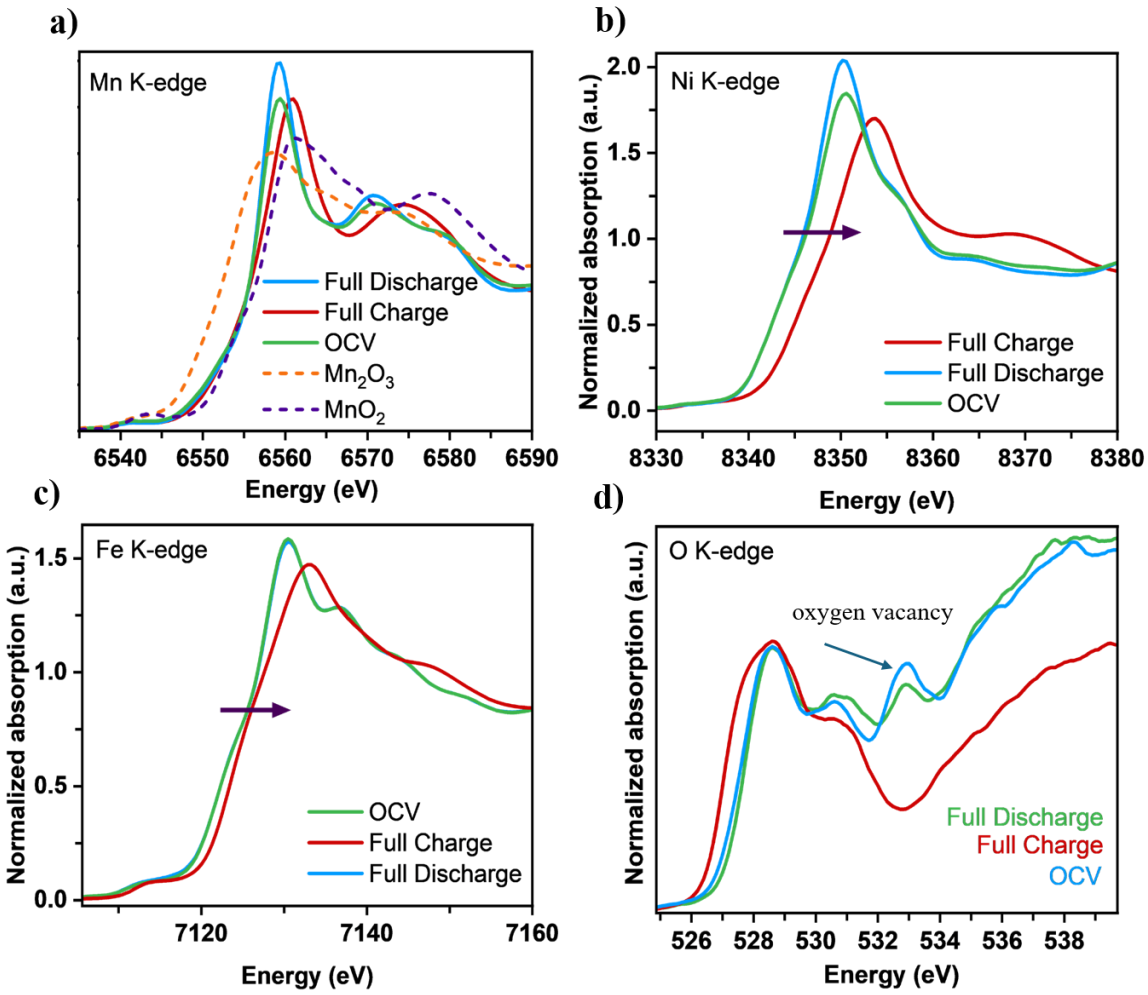

Figure 17. *Ex situ* XANES at the a) Mn K-edge; b) Ni K-edge; c) Fe K-edge; d) oxygen K-edge.

Fe K-edge XAS indicate shift to higher E (shown with an arrow) and higher oxidation states upon charging $Na_{0.95}Mn_{0.4}Fe_{0.25}Ni_{0.35}O_2$ in a good accordance with literature that involves the oxidation process (Fig. 17c). The absorption edges of pristine and discharged samples coincide,

and indicate Fe in 3+ oxidation state. The EXAFS spectra indicate that the interatomic distance of Fe–O decreases following Na^+ deintercalation, which indicates the oxidation of Fe ions. During the discharge process, the FT magnitudes revert to their original state. This occurrence corresponds to the oxidation behavior of the Fe element over the charge and previous studies noted that given the O3-type crystal structure it can be hypothesized that iron remains electrochemically inactive during the initial stage until the O3-P3 phase transition takes place, which will be clarified with Mossbauer experiment results. XPS analysis of pristine $Na_{0.95}Mn_{0.4}Fe_{0.25}Ni_{0.35}O_2$ confirms the results of Fe K-edge XAS, and indicates the presence of Fe in 3+ oxidation states (Fig. S8d).

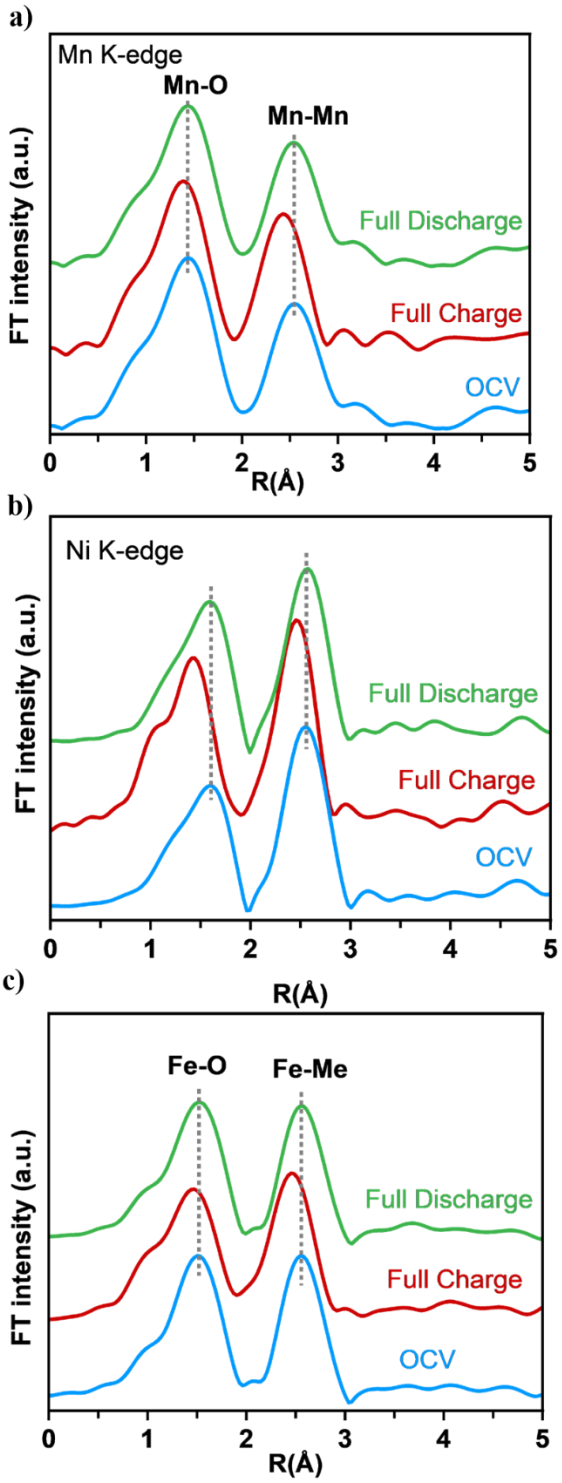

Figure 18. FT-EXAFS spectra of a) Mn K-edge; b) Ni; K-edge c) Fe K-edge.

The O K-edge showed (Fig. 17d) peak at around 530 eV arises from migrations across transition metal 3d and O 2p orbitals, while the edge peak at 534 eV corresponds to oxygen vacancies. The edge exhibits a minor displacement towards the lower energy region, and the oxygen vacancy peak is absent in the charged samples, attributed to the triggered electron filling and removal inside the O 2p band due to oxygen redox[89].

In order to acquire deeper insights into the structural evolution of the prepared material during the Na^+ (de)intercalation process, *operando* XRD patterns were obtained in the voltage range of 2.0–4.4 V upon 2 cycles (Fig. 19). At the onset of Na^+ deintercalation, the (003) peak of the O3 phase predominantly shifts to a lower angle, suggesting a two-phase reaction characterized by the coexistence of the O3 and P3 phases. The P3 phase (space group: R3m) arises due to sodium vacancies, leading to significant oxygen-oxygen repulsions that cause the translation of MO_6 layers by the (1/3, 2/3, 0) direction. As a result, positions for prismatic sodium are being established. Following further desodiation, the hexagonal P3 phase peaks exhibit a consistent shift, with the (003), (006), and (108) diffraction peak positions moving towards a lower angle, while the (101) and (102) peaks shift towards a higher angle as long as charging to 4.4 V, as illustrated in Fig.19 This behavior indicates a solid-solution reaction characterized by the expansion of the c-axis and contraction of the ab-plane, aligning with the observed electrochemical behavior. In contrast, upon completion of the charging process, a new peak corresponding to the monoclinic O'3 phase (space group: C2/m) emerged at 17.2° 2θ. The monoclinic distortion identified in the intermediate O’3 phase aligns with earlier findings for $NaNi_{0.5}Mn_{0.5}O_2$. Interestingly, monoclinic O’3 phase did not observed previously in *ex situ* XRD patterns (Chapter 5). Furthermore, this phase transition is reversible; throughout the discharging process, characterized by intercalation, the P3 phase emerges, while the O’3 phase is absent. Following complete discharge, the initial phase O3 is reinstated in its entirety positions.

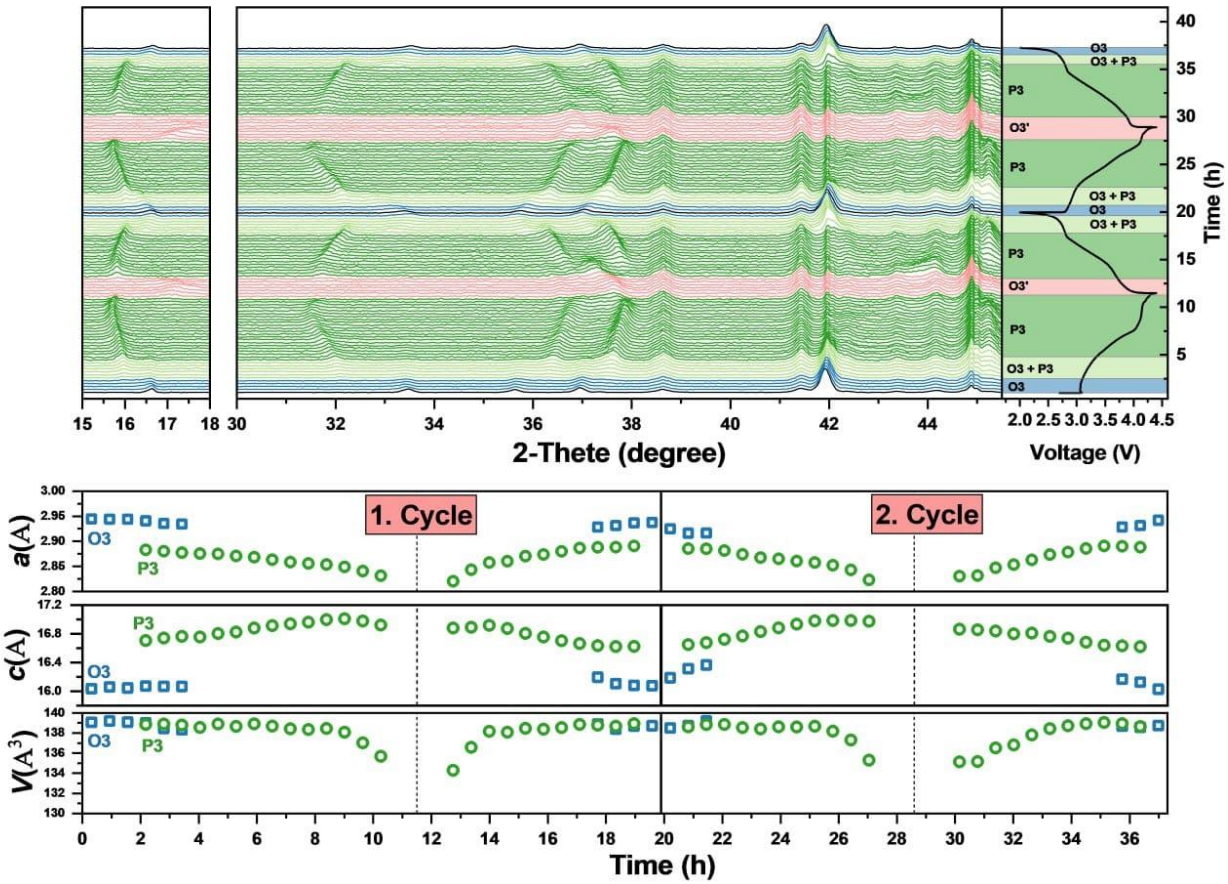

Figure 19. *Operando* XRD data during the first and second cycle.

Fig. 20 displays *the in situ* Mössbauer spectroscopy results for various voltages related to the $Na_{0.95}Mn_{0.4}Fe_{0.25}Ni_{0.35}O_2$ sample. All obtained spectra were analyzed using an asymmetrical doublet and a single line for fitting. The results for the OCV state $Na_{0.95}Mn_{0.4}Fe_{0.25}Ni_{0.35}O_2$ align with the XANES measurements discussed in previous section, which demonstrated that iron is present solely in the 3+ oxidation state within an octahedral oxygen environment. The regenerated distribution p(Δ) of the quadrupole splitting (Δ) exhibits a symmetrical shape (Fig. 20 OCV), corroborating that iron ions occupy analogous places within the structure of this complex, characterized by an erratic pattern of transition metal ions (Ni, Fe, Mn) in their surrounding[125]. As the cell voltage approaches full charge (4.4 V), there is an observable formation of Fe^{4+} ions, along with peak broadening and asymmetry in the spectral features. When returning to 2.0 V, a reversible reduction of Fe^{4+} to Fe^{3+} takes place, demonstrating stable redox behavior. Upon charging the cell to 3.5 V, a quadrupole splitting akin to that seen at 4.4 V is observed, indicating the continued

presence of high-valence Fe species. It is important to note that iron stays in the Fe^{3+} oxidation state until around 3.9 V, where reductive coupling phenomena could potentially take place.

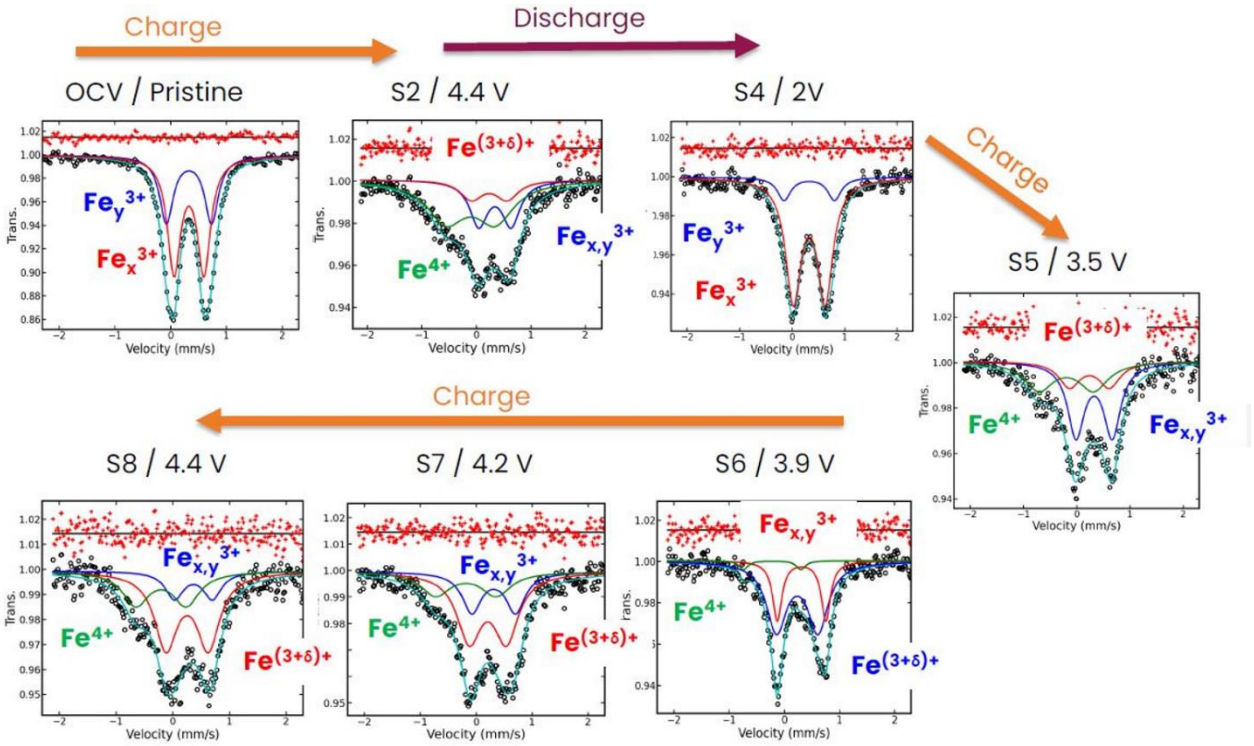

Figure 20. The *in situ* Mossbauer spectra at different voltages.

After this voltage, it is proposed that unoxidized Fe^{3+} ions may move into octahedral sites within the Na layer. This movement enables the activation of oxygen redox processes within a reachable voltage range, indicating a shift from Fe-based redox activity to O-redox. The release of O-redox generally relates to layered structures that feature A–O–A dumbbell configurations[60]. In balanced materials featuring a completely occupied transition metal layer, O-redox processes typically remain unreachable during the Fe^{3+}/Fe^{4+} redox differ unless there is migration of the transition metal ions. The migration results in the creation of vacancy-O-vacancy (□-O-□) arrangements, facilitating O-redox activity[126]. The observed electrochemical behavior near 3.9 V can likely be attributed to these structural changes.

6.4 Conclusion

This chapter provided a comprehensive analysis of the redox reactions and structural changes of the $Na_{0.95}Mn_{0.4}Fe_{0.25}Ni_{0.35}O_2$ during the extraction and insertion of sodium ions. By employing a combination of *ex situ* XANES, EXAFS, XPS, *operando* XRD and *in situ* Mössbauer spectroscopy, we attained a thorough comprehension of the electrochemical behavior and the associated structural dynamics. The findings from the XANES and EXAFS analyses indicated that Fe and Ni experience reversible oxidation-reduction processes throughout the charging and discharging cycles, with Fe shifting between 3+ and 4+ oxidation states and Ni fluctuating between 2+ and 3+. The results were validated through XPS measurements, which provided additional confirmation of the oxidation states of Mn, Fe, and Ni in the pristine material. The *in situ* XRD analysis demonstrated a reversible O3–P3 phase transition occurring during Na^+ deintercalation, featuring a solid-solution reaction. Interestingly, a monoclinic O'3 phase was observed at elevated voltages (4.4 V), which was not present in *ex situ* XRD patterns. The application of Mössbauer spectroscopy yielded significant findings regarding the iron redox behavior, validating the emergence of Fe^{4+} ions at elevated voltages and their reversible reduction during discharge. The findings indicated that iron stays electrochemically inactive until the O3–P3 phase transition takes place, following which unoxidized Fe^{3+} ions move to octahedral sites within the Na layer. This migration enables oxygen redox activity, indicating a transition from iron-based redox processes to oxygen redox mechanism. By understanding the redox behavior of transition metals (Fe and Ni) and the dynamics of oxygen redox processes, it is possible to design multi-transition metal oxide cathodes that optimize capacity retention, cycling stability, and energy density.

CHAPTER 7: Conclusion and Future perspectives

The doctoral thesis presents research on the synthesis, characterization, and performance assessment of novel layered cathode materials for sodium-ion batteries, emphasizing the doping strategy, variation of transition metal compositions to improve electrochemical performance and structural stability.

7.1 Conclusion

The synthesis and characterization of P3-$Na_{0.62}Mn_{0.75}Cu_{0.19}O_2$ revealed the material's considerable promise as an electrode for sodium-ion batteries. The addition of Cu significantly enhanced the structural stability and electrochemical performance, demonstrated by an initial charge capacity of 143 mAh g^{-1} and a discharge capacity surpassing 200 mAh g^{-1}. The observed performance can be linked to the redox activity of the $Cu^{2+}/^{3+}$, $Mn^{4+}/^{3+}$, and O^{2-}/O^{-n} pairs, which continued to exhibit activity throughout the cycling process. Advanced techniques, such as ex situ XAS, XPS, and operando DEMS, validated the stabilization of oxygen redox activities and the reduction of the Jahn-Teller distortions commonly linked to Mn^{3+}. The consistent single-phase reaction observed through operando XRD underscores the significance of Cu-substitution in preserving structural integrity, presenting a promising avenue for improving sodium-ion battery performance.

The comprehensive examination of Na_x(Ni–Fe–Mn)O_2 cathode materials, featuring different sodium contents (x = 0.75, 0.85, and 0.95), yielded essential insights into the interplay between composition, structural changes, and electrochemical performance. Among the samples, NNFM95 exhibited the most favorable electrochemical performance, which is likely associated with its higher sodium content, contributing to lower charge transfer resistance and improved Na^+ diffusion, as indicated by EIS and GITT measurements. The *ex situ* XRD analyses provided confirmation of a reversible O3–P3 phase transition, demonstrating remarkable structural stability throughout the cycling process.

Additionally, study offered an in-depth examination of the redox conduct and structural changes in $Na_{0.95}Mn_{0.4}Fe_{0.25}Ni_{0.35}O_2$ throughout the processes of Na^+ extraction / insertion. *Ex-situ* XANES and EXAFS analyses demonstrated reversible oxidation-reduction processes for Fe, Ni and O, with Fe shifting between 3+ and 4+ oxidation states and Ni fluctuating between 2+ and 3+ and confirms reversible oxygen redox. The *operando* XRD results revealed a reversible O3–P3

phase change and the appearance of a monoclinic O'3 phase at higher voltages (4.4 V). The application of *in situ* Mössbauer spectroscopy provided deeper insights into the redox behavior of iron, revealing the generation of Fe^{4+} ions at elevated voltages and their reversible reduction during the discharge process. The movement of unoxidized Fe^{3+} ions to octahedral sites within the Na layer initiated oxygen redox processes, signifying a shift from Fe-based redox to O-redox mechanisms.

7.2 Outlook

Expanding upon the encouraging findings of Cu-doping in P3-$Na_{0.62}Mn_{0.75}Cu_{0.19}O_2$, subsequent investigations may delve into the combined effects of multi-element doping to further improve electrochemical performance. The activation of oxygen redox reactions seen in $Na_{0.95}Mn_{0.4}Fe_{0.25}Ni_{0.35}O_2$ underscores the necessity of comprehending the structural evolution that enables this mechanism. Future work may utilize sophisticated DFT calculations and neutron diffraction to offer a more profound understanding of how transition metal migration and oxygen vacancy formation contribute to the stabilization of O-redox reactions and the effect of Fe dissolution to electrochemical performance. In addition, for future commercialization the full cell configuration is needed.

To improve safety and performance, subsequent studies could explore the feasibility of cathode materials with solid-state electrolytes. Considering the rising need for sustainable and economical battery technologies, future outlooks must focus on refining synthesis techniques to achieve reduced energy usage and minimal ecological footprint. The use of plentiful and safe materials, combined with recycling methods for sodium-ion battery parts, will be essential for achieving sustainable commercialization.

References

(1) Dunn, B.; Kamath, H.; Tarascon, J.-M. Electrical Energy Storage for the Grid: A Battery of Choices. *Science* **2011**, *334* (6058), 928–935. https://doi.org/10.1126/science.1212741.

(2) Yabuuchi, N.; Kubota, K.; Dahbi, M.; Komaba, S. Research Development on Sodium-Ion Batteries. *Chem. Rev.* **2014**, *114* (23), 11636–11682. https://doi.org/10.1021/cr500192f.

(3) Hwang, J.-Y.; Myung, S.-T.; Sun, Y.-K. Sodium-Ion Batteries: Present and Future. *Chem. Soc. Rev.* **2017**, *46* (12), 3529–3614. https://doi.org/10.1039/C6CS00776G.

(4) Ma, X.; Chen, H.; Ceder, G. Electrochemical Properties of Monoclinic NaMnO2. *J. Electrochem. Soc.* **2011**, *158* (12), A1307. https://doi.org/10.1149/2.035112jes.

(5) Liang, Z.; Ren, M.; Guo, Y.; Zhang, T.; Gao, X.; Ma, H.; Li, F. Depressed P3–O3′ Phase Transition in an O3-Type Layered Cathode for Advanced Sodium-Ion Batteries. *Inorg. Chem. Front.* **2023**, *10* (24), 7187–7192. https://doi.org/10.1039/D3QI01884A.

(6) Peng, B.; Wan, G.; Ahmad, N.; Yu, L.; Ma, X.; Zhang, G. Recent Progress in the Emerging Modification Strategies for Layered Oxide Cathodes toward Practicable Sodium Ion Batteries. *Advanced Energy Materials* **2023**, *13* (27), 2300334. https://doi.org/10.1002/aenm.202300334.

(7) Huang, D.; Engtrakul, C.; Nanayakkara, S.; Mulder, D. W.; Han, S.-D.; Zhou, M.; Luo, H.; Tenent, R. C. Understanding Degradation at the Lithium-Ion Battery Cathode/Electrolyte Interface: Connecting Transition-Metal Dissolution Mechanisms to Electrolyte Composition. *ACS Appl. Mater. Interfaces* **2021**, *13* (10), 11930–11939. https://doi.org/10.1021/acsami.0c22235.

(8) Yabuuchi, N.; Hara, R.; Kajiyama, M.; Kubota, K.; Ishigaki, T.; Hoshikawa, A.; Komaba, S. New O2/P2-type Li-Excess Layered Manganese Oxides as Promising Multi-Functional Electrode Materials for Rechargeable Li/Na Batteries. *Advanced Energy Materials* **2014**, *4* (13), 1301453. https://doi.org/10.1002/aenm.201301453.

(9) Konarov, A.; Choi, J. U.; Bakenov, Z.; Myung, S.-T. Revisit of Layered Sodium Manganese Oxides: Achievement of High Energy by Ni Incorporation. *J. Mater. Chem. A* **2018**, *6* (18), 8558–8567. https://doi.org/10.1039/C8TA02067A.

(10) Yabuuchi, N.; Hara, R.; Kubota, K.; Paulsen, J.; Kumakura, S.; Komaba, S. A New Electrode Material for Rechargeable Sodium Batteries: P2-Type $Na_{2/3}[Mg_{0.28}Mn_{0.72}]O_2$ with Anomalously High Reversible Capacity. *J. Mater. Chem. A* **2014**, *2* (40), 16851–16855. https://doi.org/10.1039/C4TA04351K.

(11) Konarov, A.; Jo, J. H.; Choi, J. U.; Bakenov, Z.; Yashiro, H.; Kim, J.; Myung, S.-T. Exceptionally Highly Stable Cycling Performance and Facile Oxygen-Redox of Manganese-Based Cathode Materials for Rechargeable Sodium Batteries. *Nano Energy* **2019**, *59*, 197–206. https://doi.org/10.1016/j.nanoen.2019.02.042.

(12) Pang, W.-L.; Zhang, X.-H.; Guo, J.-Z.; Li, J.-Y.; Yan, X.; Hou, B.-H.; Guan, H.-Y.; Wu, X.-L. P2-Type Na 2/3 Mn 1-x Al x O 2 Cathode Material for Sodium-Ion Batteries: Al-Doped Enhanced Electrochemical Properties and Studies on the Electrode Kinetics. *Journal of Power Sources* **2017**, *356*, 80–88. https://doi.org/10.1016/j.jpowsour.2017.04.076.

(13) Liu, Y.; Wang, C.; Zhao, S.; Zhang, L.; Zhang, K.; Li, F.; Chen, J. Mitigation of Jahn–Teller Distortion and Na^+ /Vacancy Ordering in a Distorted Manganese Oxide Cathode Material by Li Substitution. *Chem. Sci.* **2021**, *12* (3), 1062–1067. https://doi.org/10.1039/D0SC05427E.

(14) Tarascon, J.-M. Is Lithium the New Gold? *Nature Chem* **2010**, *2* (6), 510–510. https://doi.org/10.1038/nchem.680.

(15) Slater, M. D.; Kim, D.; Lee, E.; Johnson, C. S. Sodium-Ion Batteries. *Adv Funct Materials* **2013**, *23* (8), 947–958. https://doi.org/10.1002/adfm.201200691.

(16) Sawicki, M.; Shaw, L. L. Advances and Challenges of Sodium Ion Batteries as Post Lithium Ion Batteries. *RSC Adv.* **2015**, *5* (65), 53129–53154. https://doi.org/10.1039/C5RA08321D.
(17) Deng, J.; Luo, W.; Chou, S.; Liu, H.; Dou, S. Sodium-Ion Batteries: From Academic Research to Practical Commercialization. *Advanced Energy Materials* **2018**, *8* (4), 1701428. https://doi.org/10.1002/aenm.201701428.
(18) Ortiz-Vitoriano, N.; Drewett, N. E.; Gonzalo, E.; Rojo, T. High Performance Manganese-Based Layered Oxide Cathodes: Overcoming the Challenges of Sodium Ion Batteries. *Energy Environ. Sci.* **2017**, *10* (5), 1051–1074. https://doi.org/10.1039/C7EE00566K.
(19) Perveen, T.; Siddiq, M.; Shahzad, N.; Ihsan, R.; Ahmad, A.; Shahzad, M. I. Prospects in Anode Materials for Sodium Ion Batteries - A Review. *Renewable and Sustainable Energy Reviews* **2020**, *119*, 109549. https://doi.org/10.1016/j.rser.2019.109549.
(20) Xiang, X.; Zhang, K.; Chen, J. Recent Advances and Prospects of Cathode Materials for Sodium-Ion Batteries. *Advanced Materials* **2015**, *27* (36), 5343–5364. https://doi.org/10.1002/adma.201501527.
(21) Singh, A. N.; Islam, M.; Meena, A.; Faizan, M.; Han, D.; Bathula, C.; Hajibabaei, A.; Anand, R.; Nam, K. Unleashing the Potential of Sodium-Ion Batteries: Current State and Future Directions for Sustainable Energy Storage. *Adv Funct Materials* **2023**, *33* (46), 2304617. https://doi.org/10.1002/adfm.202304617.
(22) Neff, V. D. Electrochemical Oxidation and Reduction of Thin Films of Prussian Blue. *J. Electrochem. Soc.* **1978**, *125* (6), 886–887. https://doi.org/10.1149/1.2131575.
(23) Zhou, A.; Cheng, W.; Wang, W.; Zhao, Q.; Xie, J.; Zhang, W.; Gao, H.; Xue, L.; Li, J. Hexacyanoferrate-Type Prussian Blue Analogs: Principles and Advances Toward High-Performance Sodium and Potassium Ion Batteries. *Advanced Energy Materials* **2021**, *11* (2), 2000943. https://doi.org/10.1002/aenm.202000943.
(24) Lee, H.-W.; Wang, R. Y.; Pasta, M.; Woo Lee, S.; Liu, N.; Cui, Y. Manganese Hexacyanomanganate Open Framework as a High-Capacity Positive Electrode Material for Sodium-Ion Batteries. *Nat Commun* **2014**, *5* (1), 5280. https://doi.org/10.1038/ncomms6280.
(25) Cao, Y.; Li, M.; Lu, J.; Liu, J.; Amine, K. Bridging the Academic and Industrial Metrics for Next-Generation Practical Batteries. *Nat. Nanotechnol.* **2019**, *14* (3), 200–207. https://doi.org/10.1038/s41565-019-0371-8.
(26) Liu, Q.; Hu, Z.; Chen, M.; Zou, C.; Jin, H.; Wang, S.; Chou, S.; Liu, Y.; Dou, S. The Cathode Choice for Commercialization of Sodium-Ion Batteries: Layered Transition Metal Oxides versus Prussian Blue Analogs. *Adv Funct Materials* **2020**, *30* (14), 1909530. https://doi.org/10.1002/adfm.201909530.
(27) Li, H.; Xu, M.; Zhang, Z.; Lai, Y.; Ma, J. Engineering of Polyanion Type Cathode Materials for Sodium-Ion Batteries: Toward Higher Energy/Power Density. *Adv Funct Materials* **2020**, *30* (28), 2000473. https://doi.org/10.1002/adfm.202000473.
(28) Jin, T.; Li, H.; Zhu, K.; Wang, P.-F.; Liu, P.; Jiao, L. Polyanion-Type Cathode Materials for Sodium-Ion Batteries. *Chem. Soc. Rev.* **2020**, *49* (8), 2342–2377. https://doi.org/10.1039/C9CS00846B.
(29) Ellis, B. L.; Nazar, L. F. Sodium and Sodium-Ion Energy Storage Batteries. *Current Opinion in Solid State and Materials Science* **2012**, *16* (4), 168–177. https://doi.org/10.1016/j.cossms.2012.04.002.
(30) Riyanto, A.; Sutiarno, S.; Indriyani, N. A.; Warohmah, W.; Wardani, S. I. K.; Syafriadi, S.; Karo, P. K.; Suciati, S. W. Efek Perbedaan Komposisi Komposit Na2FeSiO4/C Berbasis Silika Sekam Padi Terhadap Fasa dan Sifat Listriknya. *ALCHEMY J. Pen. Kim* **2023**, *19* (2), 140. https://doi.org/10.20961/alchemy.19.2.65707.140-148.

(31) Kundu, D.; Talaie, E.; Duffort, V.; Nazar, L. F. The Emerging Chemistry of Sodium Ion Batteries for Electrochemical Energy Storage. *Angew Chem Int Ed* **2015**, *54* (11), 3431–3448. https://doi.org/10.1002/anie.201410376.
(32) Kim, H.; Hong, J.; Park, Y.; Kim, J.; Hwang, I.; Kang, K. Sodium Storage Behavior in Natural Graphite Using Ether-based Electrolyte Systems. *Adv Funct Materials* **2015**, *25* (4), 534–541. https://doi.org/10.1002/adfm.201402984.
(33) Song, Z.; Zhou, H. Towards Sustainable and Versatile Energy Storage Devices: An Overview of Organic Electrode Materials. *Energy Environ. Sci.* **2013**, *6* (8), 2280. https://doi.org/10.1039/c3ee40709h.
(34) Luo, W.; Allen, M.; Raju, V.; Ji, X. An Organic Pigment as a High-Performance Cathode for Sodium-Ion Batteries. *Advanced Energy Materials* **2014**, *4* (15), 1400554. https://doi.org/10.1002/aenm.201400554.
(35) Gao, R.-M.; Zheng, Z.-J.; Wang, P.-F.; Wang, C.-Y.; Ye, H.; Cao, F.-F. Recent Advances and Prospects of Layered Transition Metal Oxide Cathodes for Sodium-Ion Batteries. *Energy Storage Materials* **2020**, *30*, 9–26. https://doi.org/10.1016/j.ensm.2020.04.040.
(36) Liang, X.; Hwang, J.; Sun, Y. Practical Cathodes for Sodium-Ion Batteries: Who Will Take The Crown? *Advanced Energy Materials* **2023**, *13* (37), 2301975. https://doi.org/10.1002/aenm.202301975.
(37) Delmas, C.; Fouassier, C.; Hagenmuller, P. Structural Classification and Properties of the Layered Oxides. *Physica B+C* **1980**, *99* (1–4), 81–85. https://doi.org/10.1016/0378-4363(80)90214-4.
(38) Paulsen, J. M.; Thomas, C. L.; Dahn, J. R. Layered Li-Mn-Oxide with the O2 Structure: A Cathode Material for Li-Ion Cells Which Does Not Convert to Spinel. *J. Electrochem. Soc.* **1999**, *146* (10), 3560–3565. https://doi.org/10.1149/1.1392514.
(39) Liu, Q.; Hu, Z.; Chen, M.; Zou, C.; Jin, H.; Wang, S.; Chou, S.; Dou, S. Recent Progress of Layered Transition Metal Oxide Cathodes for Sodium-Ion Batteries. *Small* **2019**, *15* (32), 1805381. https://doi.org/10.1002/smll.201805381.
(40) Delmas, C.; Carlier, D.; Guignard, M. The Layered Oxides in Lithium and Sodium-Ion Batteries: A Solid-State Chemistry Approach. *Advanced Energy Materials* **2021**, *11* (2), 2001201. https://doi.org/10.1002/aenm.202001201.
(41) Han, M. H.; Gonzalo, E.; Singh, G.; Rojo, T. A Comprehensive Review of Sodium Layered Oxides: Powerful Cathodes for Na-Ion Batteries. *Energy Environ. Sci.* **2015**, *8* (1), 81–102. https://doi.org/10.1039/C4EE03192J.
(42) Vassilaras, P.; Ma, X.; Li, X.; Ceder, G. Electrochemical Properties of Monoclinic $NaNiO_2$. *J. Electrochem. Soc.* **2013**, *160* (2), A207–A211. https://doi.org/10.1149/2.023302jes.
(43) Lee, D. H.; Xu, J.; Meng, Y. S. An Advanced Cathode for Na-Ion Batteries with High Rate and Excellent Structural Stability. *Phys. Chem. Chem. Phys.* **2013**, *15* (9), 3304. https://doi.org/10.1039/c2cp44467d.
(44) Schaak, R. E.; Klimczuk, T.; Foo, M. L.; Cava, R. J. Superconductivity Phase Diagram of NaxCoO2·1.3H2O. **2003**, *424*.
(45) Delmas, C.; Braconnier, J.; Fouassier, C.; Hagenmuller, P. Electrochemical Intercalation of Sodium in NaxCoO2 Bronzes. *Solid State Ionics* **1981**, *3–4*, 165–169. https://doi.org/10.1016/0167-2738(81)90076-X.
(46) Berthelot, R.; Carlier, D.; Delmas, C. Electrochemical Investigation of the P2–NaxCoO2 Phase Diagram. *Nature Mater* **2011**, *10* (1), 74–80. https://doi.org/10.1038/nmat2920.
(47) Blesa, M. C.; Moran, E.; Leon, C.; Santamaria, J.; Tornero, J. D.; Menendez, N. A-NaFeO2: Ionic Conductivity and Sodium Extraction. *Solid State Ionics* **1999**.
(48) Komaba, S.; Nakayama, T.; Ogata, A.; Shimizu, T.; Takei, C.; Takada, S.; Hokura, A.; Nakai, I. Electrochemically Reversible Sodium Intercalation of Layered NaNi0.5Mn0.5O2 and NaCrO2. *ECS Trans.* **2009**, *16* (42), 43–55. https://doi.org/10.1149/1.3112727.

(49) Grimaud, A.; Hong, W. T.; Shao-Horn, Y.; Tarascon, J.-M. Anionic Redox Processes for Electrochemical Devices. *Nature Mater* **2016**, *15* (2), 121–126. https://doi.org/10.1038/nmat4551.
(50) Sathiya, M.; Rousse, G.; Ramesha, K.; Laisa, C. P.; Vezin, H.; Sougrati, M. T.; Doublet, M.-L.; Foix, D.; Gonbeau, D.; Walker, W.; Prakash, A. S.; Ben Hassine, M.; Dupont, L.; Tarascon, J.-M. Reversible Anionic Redox Chemistry in High-Capacity Layered-Oxide Electrodes. *Nature Mater* **2013**, *12* (9), 827–835. https://doi.org/10.1038/nmat3699.
(51) Xu, H.; Guo, S.; Zhou, H. Review on Anionic Redox in Sodium-Ion Batteries. *J. Mater. Chem. A* **2019**, *7* (41), 23662–23678. https://doi.org/10.1039/C9TA06389G.
(52) Rossouw, M. H.; Thackeray, M. M. LITHIUM MANGANESE OXIDES FROM Li2MnO3 FOR RECHARGEABLE LITHIUM BA'ITERY APPLICATIONS. *26* (6).
(53) Oishi, M.; Yamanaka, K.; Watanabe, I.; Shimoda, K.; Matsunaga, T.; Arai, H.; Ukyo, Y.; Uchimoto, Y.; Ogumi, Z.; Ohta, T. Direct Observation of Reversible Oxygen Anion Redox Reaction in Li-Rich Manganese Oxide, Li_2 MnO_3 , Studied by Soft X-Ray Absorption Spectroscopy. *J. Mater. Chem. A* **2016**, *4* (23), 9293–9302. https://doi.org/10.1039/C6TA00174B.
(54) Shimoda, K.; Oishi, M.; Matsunaga, T.; Murakami, M.; Yamanaka, K.; Arai, H.; Ukyo, Y.; Uchimoto, Y.; Ohta, T.; Matsubara, E.; Ogumi, Z. Direct Observation of Layered-to-Spinel Phase Transformation in Li_2 MnO_3 and the Spinel Structure Stabilised after the Activation Process. *J. Mater. Chem. A* **2017**, *5* (14), 6695–6707. https://doi.org/10.1039/C6TA11151C.
(55) Assat, G.; Tarascon, J.-M. Fundamental Understanding and Practical Challenges of Anionic Redox Activity in Li-Ion Batteries. *Nat Energy* **2018**, *3* (5), 373–386. https://doi.org/10.1038/s41560-018-0097-0.
(56) Amatucci, G. G.; Tarascon, J. M.; Klein, L. C. CoO2, The End Member of the Li x CoO2 Solid Solution. *J. Electrochem. Soc.* **1996**, *143* (3), 1114–1123. https://doi.org/10.1149/1.1836594.
(57) Tarascon, J. M.; Vaughan, G.; Chabre, Y.; Seguin, L.; Anne, M.; Strobel, P.; Amatucci, G. In Situ Structural and Electrochemical Study of Ni1−xCoxO2 Metastable Oxides Prepared by Soft Chemistry. *Journal of Solid State Chemistry* **1999**, *147* (1), 410–420. https://doi.org/10.1006/jssc.1999.8465.
(58) Yabuuchi, N. Solid-State Redox Reaction of Oxide Ions for Rechargeable Batteries. *Chem. Lett.* **2017**, *46* (4), 412–422. https://doi.org/10.1246/cl.161044.
(59) Zaanen, J.; Sawatzky, G. A.; Allen, J. W. Band Gaps and Electronic Structure of Transition-Metal Compounds. *Phys. Rev. Lett.* **1985**, *55* (4), 418–421. https://doi.org/10.1103/PhysRevLett.55.418.
(60) Seo, D.-H.; Lee, J.; Urban, A.; Malik, R.; Kang, S.; Ceder, G. The Structural and Chemical Origin of the Oxygen Redox Activity in Layered and Cation-Disordered Li-Excess Cathode Materials. *Nature Chem* **2016**, *8* (7), 692–697. https://doi.org/10.1038/nchem.2524.
(61) Okubo, M.; Yamada, A. Molecular Orbital Principles of Oxygen-Redox Battery Electrodes. *ACS Appl. Mater. Interfaces* **2017**, *9* (42), 36463–36472. https://doi.org/10.1021/acsami.7b09835.
(62) Xiao, R.; Li, H.; Chen, L. Density Functional Investigation on Li_2 MnO_3. *Chem. Mater.* **2012**, *24* (21), 4242–4251. https://doi.org/10.1021/cm3027219.
(63) Wu, Q.; Zhang, T.; Geng, J.; Gao, S.; Ma, H.; Li, F. Anionic Redox Chemistry for Sodium-Ion Batteries: Mechanisms, Advances, and Challenges. *Energy Fuels* **2022**, *36* (15), 8081–8095. https://doi.org/10.1021/acs.energyfuels.2c01601.
(64) Kim, D.; Lee, J. Anionic Redox Reactions in Manganese-Based Binary Layered Oxides for Advanced Sodium-Ion Batteries. *Chem. Mater.* **2020**, *32* (13), 5541–5549. https://doi.org/10.1021/acs.chemmater.0c00415.

(65) Zuo, W.; Ren, F.; Li, Q.; Wu, X.; Fang, F.; Yu, X.; Li, H.; Yang, Y. Insights of the Anionic Redox in P2–Na0.67Ni0.33Mn0.67O2. *Nano Energy* **2020**, *78*, 105285. https://doi.org/10.1016/j.nanoen.2020.105285.
(66) Dai, K.; Wu, J.; Zhuo, Z.; Li, Q.; Sallis, S.; Mao, J.; Ai, G.; Sun, C.; Li, Z.; Gent, W. E.; Chueh, W. C.; Chuang, Y.; Zeng, R.; Shen, Z.; Pan, F.; Yan, S.; Piper, L. F. J.; Hussain, Z.; Liu, G.; Yang, W. High Reversibility of Lattice Oxygen Redox Quantified by Direct Bulk Probes of Both Anionic and Cationic Redox Reactions. *Joule* **2019**, *3* (2), 518–541. https://doi.org/10.1016/j.joule.2018.11.014.
(67) Vergnet, J.; Saubanère, M.; Doublet, M.-L.; Tarascon, J.-M. The Structural Stability of P2-Layered Na-Based Electrodes during Anionic Redox. *Joule* **2020**, *4* (2), 420–434. https://doi.org/10.1016/j.joule.2019.12.003.
(68) Ma, C.; Alvarado, J.; Xu, J.; Clément, R. J.; Kodur, M.; Tong, W.; Grey, C. P.; Meng, Y. S. Exploring Oxygen Activity in the High Energy P2-Type $Na_{0.78}$ $Ni_{0.23}$ $Mn_{0.69}$ O_2 Cathode Material for Na-Ion Batteries. *J. Am. Chem. Soc.* **2017**, *139* (13), 4835–4845. https://doi.org/10.1021/jacs.7b00164.
(69) Susanto, D.; Cho, M. K.; Ali, G.; Kim, J.-Y.; Chang, H. J.; Kim, H.-S.; Nam, K.-W.; Chung, K. Y. Anionic Redox Activity as a Key Factor in the Performance Degradation of $NaFeO_2$ Cathodes for Sodium Ion Batteries. *Chem. Mater.* **2019**, *31* (10), 3644–3651. https://doi.org/10.1021/acs.chemmater.9b00149.
(70) Hakim, C.; Sabi, N.; Ma, L. A.; Dahbi, M.; Brandell, D.; Edström, K.; Duda, L. C.; Saadoune, I.; Younesi, R. Understanding the Redox Process upon Electrochemical Cycling of the P2-Na0.78Co1/2Mn1/3Ni1/6O2 Electrode Material for Sodium-Ion Batteries. *Commun Chem* **2020**, *3* (1), 9. https://doi.org/10.1038/s42004-020-0257-6.
(71) Maitra, U.; House, R. A.; Somerville, J. W.; Tapia-Ruiz, N.; Lozano, J. G.; Guerrini, N.; Hao, R.; Luo, K.; Jin, L.; Pérez-Osorio, M. A.; Massel, F.; Pickup, D. M.; Ramos, S.; Lu, X.; McNally, D. E.; Chadwick, A. V.; Giustino, F.; Schmitt, T.; Duda, L. C.; Roberts, M. R.; Bruce, P. G. Oxygen Redox Chemistry without Excess Alkali-Metal Ions in Na2/3[Mg0.28Mn0.72]O2. *Nature Chem* **2018**, *10* (3), 288–295. https://doi.org/10.1038/nchem.2923.
(72) Eum, D.; Kim, B.; Song, J.-H.; Park, H.; Jang, H.-Y.; Kim, S. J.; Cho, S.-P.; Lee, M. H.; Heo, J. H.; Park, J.; Ko, Y.; Park, S. K.; Kim, J.; Oh, K.; Kim, D.-H.; Kang, S. J.; Kang, K. Coupling Structural Evolution and Oxygen-Redox Electrochemistry in Layered Transition Metal Oxides. *Nat. Mater.* **2022**, *21* (6), 664–672. https://doi.org/10.1038/s41563-022-01209-1.
(73) Wang, S.; Sun, C.; Wang, N.; Zhang, Q. Ni- and/or Mn-Based Layered Transition Metal Oxides as Cathode Materials for Sodium Ion Batteries: Status, Challenges and Countermeasures. *J. Mater. Chem. A* **2019**, *7* (17), 10138–10158. https://doi.org/10.1039/C8TA12441H.
(74) Su, H.; Jaffer, S.; Yu, H. Transition Metal Oxides for Sodium-Ion Batteries. *Energy Storage Materials* **2016**, *5*, 116–131. https://doi.org/10.1016/j.ensm.2016.06.005.
(75) Mendiboure, A. Electrochemical Intercalation and Deintercalation of NaxMnOz Bronzes.
(76) Caballero, A.; Hernán, L.; Morales, J.; Sánchez, L.; Santos Peña, J.; Aranda, M. A. G. Synthesis and Characterization of High-Temperature Hexagonal P2-Na0.6 MnO2 and Its Electrochemical Behaviour as Cathode in Sodium Cells. *J. Mater. Chem.* **2002**, *12* (4), 1142–1147. https://doi.org/10.1039/b108830k.
(77) Zhuang, Y.; Zhao, J.; Zhao, Y.; Zhu, X.; Xia, H. Carbon-Coated Single Crystal O3-NaFeO2 Nanoflakes Prepared via Topochemical Reaction for Sodium-Ion Batteries. *Sustainable Materials and Technologies* **2021**, *28*, e00258. https://doi.org/10.1016/j.susmat.2021.e00258.
(78) Lee, E.; Brown, D. E.; Alp, E. E.; Ren, Y.; Lu, J.; Woo, J.-J.; Johnson, C. S. New Insights into the Performance Degradation of Fe-Based Layered Oxides in Sodium-Ion Batteries:

Instability of Fe^{3+} /Fe^{4+} Redox in α-$NaFeO_2$. *Chem. Mater.* **2015**, *27* (19), 6755–6764. https://doi.org/10.1021/acs.chemmater.5b02918.
(79) Wang, L.; Wang, J.; Zhang, X.; Ren, Y.; Zuo, P.; Yin, G.; Wang, J. Unravelling the Origin of Irreversible Capacity Loss in NaNiO2 for High Voltage Sodium Ion Batteries. *Nano Energy* **2017**, *34*, 215–223. https://doi.org/10.1016/j.nanoen.2017.02.046.
(80) Tang, M.; Yang, J.; Chen, N.; Zhu, S.; Wang, X.; Wang, T.; Zhang, C.; Xia, Y. Overall Structural Modification of a Layered Ni-Rich Cathode for Enhanced Cycling Stability and Rate Capability at High Voltage. *J. Mater. Chem. A* **2019**, *7* (11), 6080–6089. https://doi.org/10.1039/C8TA12494A.
(81) Han, M. H.; Gonzalo, E.; Casas-Cabanas, M.; Rojo, T. Structural Evolution and Electrochemistry of Monoclinic NaNiO2 upon the First Cycling Process. *Journal of Power Sources* **2014**, *258*, 266–271. https://doi.org/10.1016/j.jpowsour.2014.02.048.
(82) Yabuuchi, N.; Yano, M.; Yoshida, H.; Kuze, S.; Komaba, S. Synthesis and Electrode Performance of O3-Type $NaFeO_2$ -$NaNi_{1/2}$ $Mn_{1/2}$ O_2 Solid Solution for Rechargeable Sodium Batteries. *J. Electrochem. Soc.* **2013**, *160* (5), A3131–A3137. https://doi.org/10.1149/2.018305jes.
(83) Hwang, J.-Y.; Myung, S.-T.; Aurbach, D.; Sun, Y.-K. Effect of Nickel and Iron on Structural and Electrochemical Properties of O3 Type Layer Cathode Materials for Sodium-Ion Batteries. *Journal of Power Sources* **2016**, *324*, 106–112. https://doi.org/10.1016/j.jpowsour.2016.05.064.
(84) Jeong, M.; Lee, H.; Yoon, J.; Yoon, W.-S. O3-Type NaNi1/3Fe1/3Mn1/3O2 Layered Cathode for Na-Ion Batteries: Structural Evolution and Redox Mechanism upon Na (de) Intercalation. *Journal of Power Sources* **2019**, *439*, 227064. https://doi.org/10.1016/j.jpowsour.2019.227064.
(85) Li, X.; Wang, Y.; Wu, D.; Liu, L.; Bo, S.-H.; Ceder, G. Jahn–Teller Assisted Na Diffusion for High Performance Na Ion Batteries. *Chem. Mater.* **2016**, *28* (18), 6575–6583. https://doi.org/10.1021/acs.chemmater.6b02440.
(86) Mason, C. W.; Lange, F.; Saravanan, K.; Lin, F.; Nordlund, D. Beyond Divalent Copper: A Redox Couple for Sodium Ion Battery Cathode Materials. *ECS Electrochemistry Letters* **2015**, *4* (5), A41–A44. https://doi.org/10.1149/2.0041505eel.
(87) Wang, Q.; Mariyappan, S.; Vergnet, J.; Abakumov, A. M.; Rousse, G.; Rabuel, F.; Chakir, M.; Tarascon, J. Reaching the Energy Density Limit of Layered O3-$NaNi_{0.5}$ $Mn_{0.5}$ O_2 Electrodes via Dual Cu and Ti Substitution. *Advanced Energy Materials* **2019**, *9* (36), 1901785. https://doi.org/10.1002/aenm.201901785.
(88) Shishkin, M.; Kumakura, S.; Sato, S.; Kubota, K.; Komaba, S.; Sato, H. Unraveling the Role of Doping in Selective Stabilization of $NaMnO_2$ Polymorphs: Combined Theoretical and Experimental Study. *Chem. Mater.* **2018**, *30* (4), 1257–1264. https://doi.org/10.1021/acs.chemmater.7b04394.
(89) Rong, X.; Hu, E.; Lu, Y.; Meng, F.; Zhao, C.; Wang, X.; Zhang, Q.; Yu, X.; Gu, L.; Hu, Y.-S.; Li, H.; Huang, X.; Yang, X.-Q.; Delmas, C.; Chen, L. Anionic Redox Reaction-Induced High-Capacity and Low-Strain Cathode with Suppressed Phase Transition. *Joule* **2019**, *3* (2), 503–517. https://doi.org/10.1016/j.joule.2018.10.022.
(90) Zheng, W.; Liu, Q.; Wang, Z.; Wu, Z.; Gu, S.; Cao, L.; Zhang, K.; Fransaer, J.; Lu, Z. Oxygen Redox Activity with Small Voltage Hysteresis in Na0.67Cu0.28Mn0.72O2 for Sodium-Ion Batteries. *Energy Storage Materials* **2020**, *28*, 300–306. https://doi.org/10.1016/j.ensm.2020.03.016.
(91) Kim, E. J.; Hosaka, T.; Kubota, K.; Tatara, R.; Kumakura, S.; Komaba, S. Effect of Cu Substitution in P′2- and P2-Type Sodium Manganese-Based Oxides. **2022**.
(92) Linnell, S. F.; Manche, A. G.; Liao, Y.; Hirsbrunner, M.; Imada, S.; Naden, A. B.; Irvine, J. T. S.; Duda, L. C.; Armstrong, A. R. Effect of Cu Substitution on Anion Redox Behaviour

in P3-Type Sodium Manganese Oxides. *J. Phys. Energy* **2022**, *4* (4), 044006. https://doi.org/10.1088/2515-7655/ac95cc.
(93) Mortemard De Boisse, B.; Nishimura, S.; Watanabe, E.; Lander, L.; Tsuchimoto, A.; Kikkawa, J.; Kobayashi, E.; Asakura, D.; Okubo, M.; Yamada, A. Highly Reversible Oxygen-Redox Chemistry at 4.1 V in $Na_{4/7-x}[\square_{1/7}Mn_{6/7}]O_2$ (□: Mn Vacancy). *Advanced Energy Materials* **2018**, *8* (20), 1800409. https://doi.org/10.1002/aenm.201800409.
(94) Or, T.; Kaliyappan, K.; Bai, Z.; Chen, Z. High Voltage Stability and Characterization of P2-$Na_{0.66}Mn_{1-y}Mg_yO_2$ Cathode for Sodium-Ion Batteries. *ChemElectroChem* **2020**, *7* (15), 3284–3290. https://doi.org/10.1002/celc.202000414.
(95) Liu, H.; Gao, X.; Chen, J.; Gao, J.; Wang, H.; Mei, Y.; Liu, H.; Deng, W.; Zou, G.; Hou, H.; Ji, X. Cu-Substitution P2-Na0.66Mn1-Cu O2 Sodium-Ion Cathode with Enhanced Interlayer Stability. *Journal of Energy Chemistry* **2022**, *75*, 478–485. https://doi.org/10.1016/j.jechem.2022.09.010.
(96) Islam, M. S.; Fisher, C. A. J. Lithium and Sodium Battery Cathode Materials: Computational Insights into Voltage, Diffusion and Nanostructural Properties. *Chem. Soc. Rev.* **2014**, *43* (1), 185–204. https://doi.org/10.1039/C3CS60199D.
(97) Saxena, S.; Badole, M.; Vasavan, H. N.; Srihari, V.; Das, A. K.; Gami, P.; Dagar, N.; Deswal, S.; Kumar, P.; Poswal, H. K.; Kumar, S. Elucidating the Electrochemical Behavior of a P3-Type High-Na-Content Cathode. *Energy Fuels* **2024**, *38* (13), 12140–12149. https://doi.org/10.1021/acs.energyfuels.4c01476.
(98) Qiao, Y.; Guo, S.; Zhu, K.; Liu, P.; Li, X.; Jiang, K.; Sun, C.-J.; Chen, M.; Zhou, H. Reversible Anionic Redox Activity in Na_3RuO_4 Cathodes: A Prototype Na-Rich Layered Oxide. *Energy Environ. Sci.* **2018**, *11* (2), 299–305. https://doi.org/10.1039/C7EE03554C.
(99) Siriwardena, D. P.; Fernando, J. F. S.; Wang, T.; Firestein, K. L.; Zhang, C.; Brand, H. E. A.; Jones, M. W. M.; Kewish, C. M.; Berntsen, P.; Jenkins, T.; Lewis, C.-E. M.; Von Treifeldt, J. E.; Dubal, D. P.; Golberg, D. V. Probing the Effect of Mg Doping on Triclinic Na2Mn3O7 Transition Metal Oxide as Cathode Material for Sodium-Ion Batteries. *Electrochimica Acta* **2021**, *394*, 139139. https://doi.org/10.1016/j.electacta.2021.139139.
(100) Toumar, A. J.; Ong, S. P.; Richards, W. D.; Dacek, S.; Ceder, G. Vacancy Ordering in O 3 -Type Layered Metal Oxide Sodium-Ion Battery Cathodes. *Phys. Rev. Applied* **2015**, *4* (6), 064002. https://doi.org/10.1103/PhysRevApplied.4.064002.
(101) Stansby, J. H.; Sharma, N.; Goonetilleke, D. Probing the Charged State of Layered Positive Electrodes in Sodium-Ion Batteries: Reaction Pathways, Stability and Opportunities. *J. Mater. Chem. A* **2020**, *8* (47), 24833–24867. https://doi.org/10.1039/D0TA09553B.
(102) Voronina, N.; Shin, M.; Kim, H.; Yaqoob, N.; Guillon, O.; Song, S. H.; Kim, H.; Lim, H.; Jung, H.; Kim, Y.; Lee, H.; Lee, K.; Yazawa, K.; Gotoh, K.; Kaghazchi, P.; Myung, S. Hysteresis-Suppressed Reversible Oxygen-Redox Cathodes for Sodium-Ion Batteries. *Advanced Energy Materials* **2022**, *12* (21), 2103939. https://doi.org/10.1002/aenm.202103939.
(103) Yabuuchi, N.; Nakayama, M.; Takeuchi, M.; Komaba, S.; Hashimoto, Y.; Mukai, T.; Shiiba, H.; Sato, K.; Kobayashi, Y.; Nakao, A.; Yonemura, M.; Yamanaka, K.; Mitsuhara, K.; Ohta, T. Origin of Stabilization and Destabilization in Solid-State Redox Reaction of Oxide Ions for Lithium-Ion Batteries. *Nat Commun* **2016**, *7* (1), 13814. https://doi.org/10.1038/ncomms13814.
(104) Jia, M.; Li, H.; Qiao, Y.; Wang, L.; Cao, X.; Cabana, J.; Zhou, H. Elucidating Anionic Redox Chemistry in P3 Layered Cathode for Na-Ion Batteries. *ACS Appl. Mater. Interfaces* **2020**, *12* (34), 38249–38255. https://doi.org/10.1021/acsami.0c11763.
(105) Min, K.; Kim, K.; Jung, C.; Seo, S.-W.; Song, Y. Y.; Lee, H. S.; Shin, J.; Cho, E. A Comparative Study of Structural Changes in Lithium Nickel Cobalt Manganese Oxide as

a Function of Ni Content during Delithiation Process. *Journal of Power Sources* **2016**, *315*, 111–119. https://doi.org/10.1016/j.jpowsour.2016.03.017.
(106) Huang, Q.; Liu, J.; Zhang, L.; Xu, S.; Chen, L.; Wang, P.; Ivey, D. G.; Wei, W. Tailoring Alternating Heteroepitaxial Nanostructures in Na-Ion Layered Oxide Cathodes via an in-Situ Composition Modulation Route. *Nano Energy* **2018**, *44*, 336–344. https://doi.org/10.1016/j.nanoen.2017.12.014.
(107) Cheng, C.; Hu, H.; Yuan, C.; Xia, X.; Mao, J.; Dai, K.; Zhang, L. Precisely Modulating the Structural Stability and Redox Potential of Sodium Layered Cathodes through the Synergetic Effect of Co-Doping Strategy. *Energy Storage Materials* **2022**, *52*, 10–18. https://doi.org/10.1016/j.ensm.2022.07.030.
(108) Cheng, C.; Chen, C.; Chu, S.; Hu, H.; Yan, T.; Xia, X.; Feng, X.; Guo, J.; Sun, D.; Wu, J.; Guo, S.; Zhang, L. Enhancing the Reversibility of Lattice Oxygen Redox Through Modulated Transition Metal–Oxygen Covalency for Layered Battery Electrodes. *Advanced Materials* **2022**, *34* (20), 2201152. https://doi.org/10.1002/adma.202201152.
(109) Chen, G.; Ji, H.; Fang, H.; Zhai, J.; Ma, Z.; Ji, W.; Wang, Y.; Huang, Y.; Liu, L.; Tong, W.; Zeng, W.; Xiao, Y. Dual Modification of P3-Type Layered Cathodes to Achieve High Capacity and Long Cyclability for Sodium-Ion Batteries. *ACS Appl. Mater. Interfaces* **2023**, *15* (28), 33682–33692. https://doi.org/10.1021/acsami.3c06375.
(110) Kumakura, S.; Tahara, Y.; Kubota, K.; Chihara, K.; Komaba, S. Sodium and Manganese Stoichiometry of P2-Type $Na_{2/3}$ MnO_2. *Angew Chem Int Ed* **2016**, *55* (41), 12760–12763. https://doi.org/10.1002/anie.201606415.
(111) Okada, S.; Takahashi, Y.; Kiyabu, T.; Doi, T.; Yamaki, J.-I.; Nishida, T. Layered Transition Metal Oxides as Cathodes for Sodium Secondary Battery. *Meet. Abstr.* **2006**, *MA2006-02* (4), 201–201. https://doi.org/10.1149/MA2006-02/4/201.
(112) Ding, F.; Zhao, C.; Zhou, D.; Meng, Q.; Xiao, D.; Zhang, Q.; Niu, Y.; Li, Y.; Rong, X.; Lu, Y.; Chen, L.; Hu, Y.-S. A Novel Ni-Rich O3-Na[Ni0.60Fe0.25Mn0.15]O2 Cathode for Na-Ion Batteries. *Energy Storage Materials* **2020**, *30*, 420–430. https://doi.org/10.1016/j.ensm.2020.05.013.
(113) Yuan, D. D.; Wang, Y. X.; Cao, Y. L.; Ai, X. P.; Yang, H. X. Improved Electrochemical Performance of Fe-Substituted $NaNi_{0.5}$ $Mn_{0.5}$ O_2 Cathode Materials for Sodium-Ion Batteries. *ACS Appl. Mater. Interfaces* **2015**, *7* (16), 8585–8591. https://doi.org/10.1021/acsami.5b00594.
(114) Sun, X.; Jin, Y.; Zhang, C.-Y.; Wen, J.-W.; Shao, Y.; Zang, Y.; Chen, C.-H. $Na[Ni_{0.4}$ $Fe_{0.2}$ $Mn_{0.4-x}$ $Ti_x]O_2$: A Cathode of High Capacity and Superior Cyclability for Na-Ion Batteries. *J. Mater. Chem. A* **2014**, *2* (41), 17268–17271. https://doi.org/10.1039/C4TA03828B.
(115) Guo, H.; Avdeev, M.; Sun, K.; Ma, X.; Wang, H.; Hu, Y.; Chen, D. Pentanary Transition-Metals Na-Ion Layered Oxide Cathode with Highly Reversible O3-P3 Phase Transition. *Chemical Engineering Journal* **2021**, *412*, 128704. https://doi.org/10.1016/j.cej.2021.128704.
(116) Wang, H.; Liao, X.-Z.; Yang, Y.; Yan, X.; He, Y.-S.; Ma, Z.-F. Large-Scale Synthesis of $NaNi_{1/3}$ $Fe_{1/3}$ $Mn_{1/3}$ O_2 as High Performance Cathode Materials for Sodium Ion Batteries. *J. Electrochem. Soc.* **2016**, *163* (3), A565–A570. https://doi.org/10.1149/2.0011605jes.
(117) Fu, H.; Fan, G.; Zhou, J.; Yu, X.; Xie, X.; Wang, J.; Lu, B.; Liang, S. Facilitating Phase Evolution for a High-Energy-Efficiency, Low-Cost O3-Type Na_x $Cu_{0.18}$ $Fe_{0.3}$ $Mn_{0.52}$ O_2 Sodium Ion Battery Cathode. *Inorg. Chem.* **2020**, *59* (18), 13792–13800. https://doi.org/10.1021/acs.inorgchem.0c02239.
(118) Stansby, J. H.; Dose, W. M.; Sharma, N.; Kimpton, J. A.; López Del Amo, J. M.; Gonzalo, E.; Rojo, T. Structural Evolution and Electrochemistry of the Mn-Rich P2–Na2/3Mn0.9Ti0.05Fe0.05O2 Positive Electrode Material. *Electrochimica Acta* **2020**, *341*, 135978. https://doi.org/10.1016/j.electacta.2020.135978.

(119) Ding, Y.; Wang, S.; Sun, Y.; Liu, Q.; An, Q.; Guo, H. Layered Cathode-Na0.67Li0.15Ni0.18Mg0.02Mn0.8O2 with P2/O3 Hybrid Phase for High-Performance Na-Ion Batteries. *Journal of Alloys and Compounds* **2023**, *939*, 168780. https://doi.org/10.1016/j.jallcom.2023.168780.
(120) Li, Z.; Du, F.; Bie, X.; Zhang, D.; Cai, Y.; Cui, X.; Wang, C.; Chen, G.; Wei, Y. Electrochemical Kinetics of the Li[$Li_{0.23}$ $Co_{0.3}$ $Mn_{0.47}$]O_2 Cathode Material Studied by GITT and EIS. *J. Phys. Chem. C* **2010**, *114* (51), 22751–22757. https://doi.org/10.1021/jp1088788.
(121) Yu, L.; Cheng, Z.; Xu, K.; Chang, Y.-X.; Feng, Y.-H.; Si, D.; Liu, M.; Wang, P.-F.; Xu, S. Interlocking Biphasic Chemistry for High-Voltage P2/O3 Sodium Layered Oxide Cathode. *Energy Storage Materials* **2022**, *50*, 730–739. https://doi.org/10.1016/j.ensm.2022.06.012.
(122) Yabuuchi, N.; Kajiyama, M.; Iwatate, J.; Nishikawa, H.; Hitomi, S.; Okuyama, R.; Usui, R.; Yamada, Y.; Komaba, S. P2-Type Nax[Fe1/2Mn1/2]O2 Made from Earth-Abundant Elements for Rechargeable Na Batteries. *Nature Mater* **2012**, *11* (6), 512–517. https://doi.org/10.1038/nmat3309.
(123) Pieczonka, N. P. W.; Liu, Z.; Lu, P.; Olson, K. L.; Moote, J.; Powell, B. R.; Kim, J.-H. Understanding Transition-Metal Dissolution Behavior in $LiNi_{0.5}$ $Mn_{1.5}$ O_4 High-Voltage Spinel for Lithium Ion Batteries. *J. Phys. Chem. C* **2013**, *117* (31), 15947–15957. https://doi.org/10.1021/jp405158m.
(124) Chen, C.; Huang, W.; Li, Y.; Zhang, M.; Nie, K.; Wang, J.; Zhao, W.; Qi, R.; Zuo, C.; Li, Z.; Yi, H.; Pan, F. P2/O3 Biphasic Fe/Mn-Based Layered Oxide Cathode with Ultrahigh Capacity and Great Cyclability for Sodium Ion Batteries. *Nano Energy* **2021**, *90*, 106504. https://doi.org/10.1016/j.nanoen.2021.106504.
(125) Shevchenko, V. A.; Glazkova, I. S.; Novichkov, D. A.; Skvortsova, I.; Sobolev, A. V.; Abakumov, A. M.; Presniakov, I. A.; Drozhzhin, O. A.; Antipov, E. V. Competition between the Ni and Fe Redox in the O3-$NaNi_{1/3}$ $Fe_{1/3}$ $Mn_{1/3}$ O_2 Cathode Material for Na-Ion Batteries. *Chem. Mater.* **2023**, *35* (10), 4015–4025. https://doi.org/10.1021/acs.chemmater.3c00338.
(126) Boivin, E.; House, R. A.; Marie, J.; Bruce, P. G. Controlling Iron Versus Oxygen Redox in the Layered Cathode $Na_{0.67}$ $Fe_{0.5}$ $Mn_{0.5}$ O_2 : Mitigating Voltage and Capacity Fade by Mg Substitution. *Advanced Energy Materials* **2022**, *12* (30), 2200702. https://doi.org/10.1002/aenm.202200702.

Supplementary information

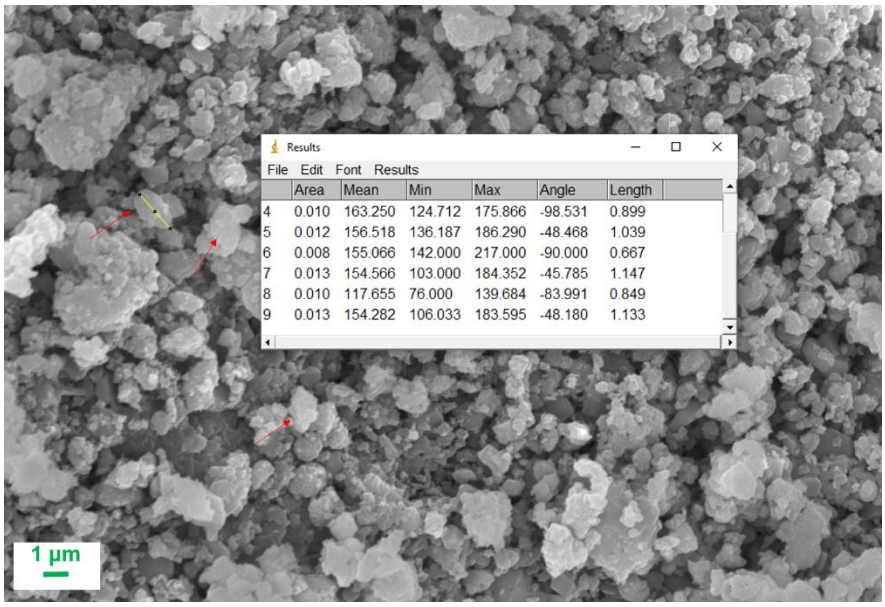

Figure S1. SEM image of Cu-doped material (average particle size identification by Image J).

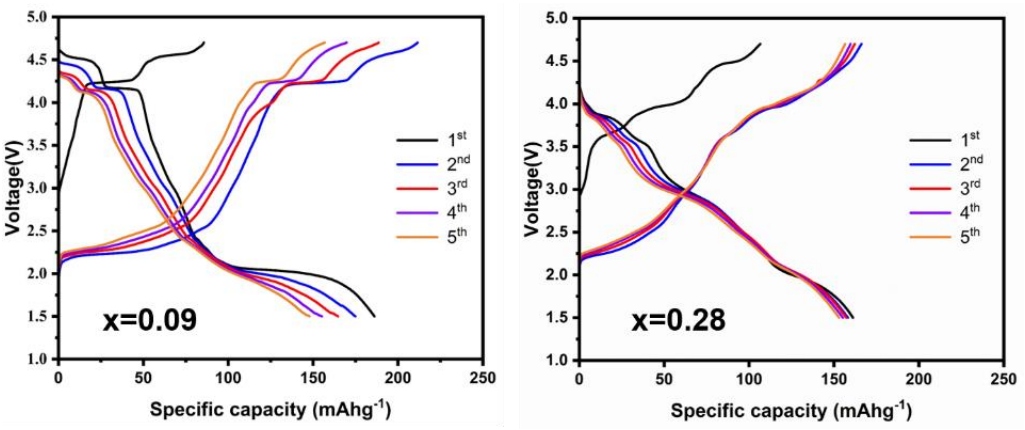

Figure S2. Galvanostatic charge/discharge profile at the current of 20 mA g^{-1}: a) x=0.09 and b) x=0.28.

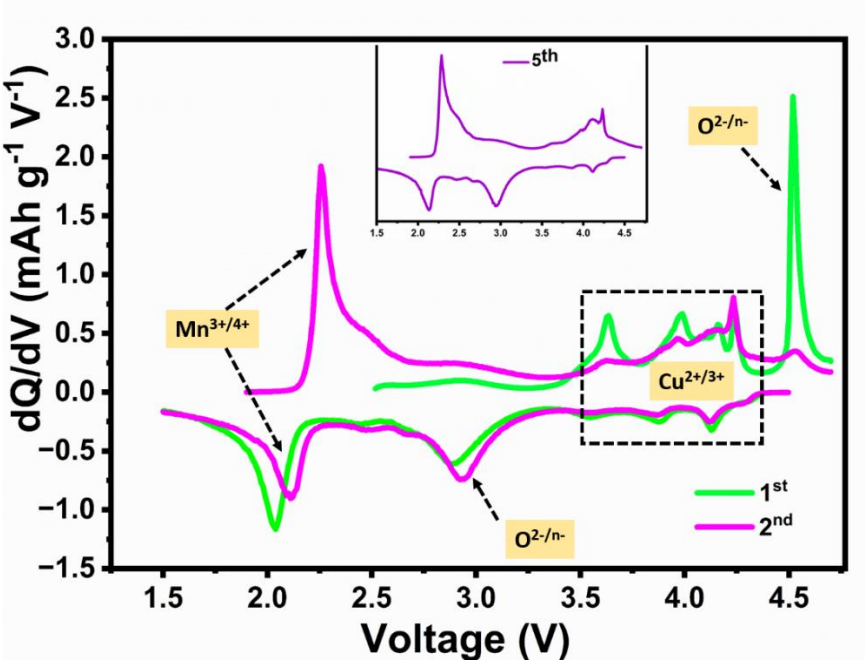

Figure S3. The corresponding dQ/dV plot of $Na_{0.62}Mn_{0.75}Cu_{0.19}O_2$

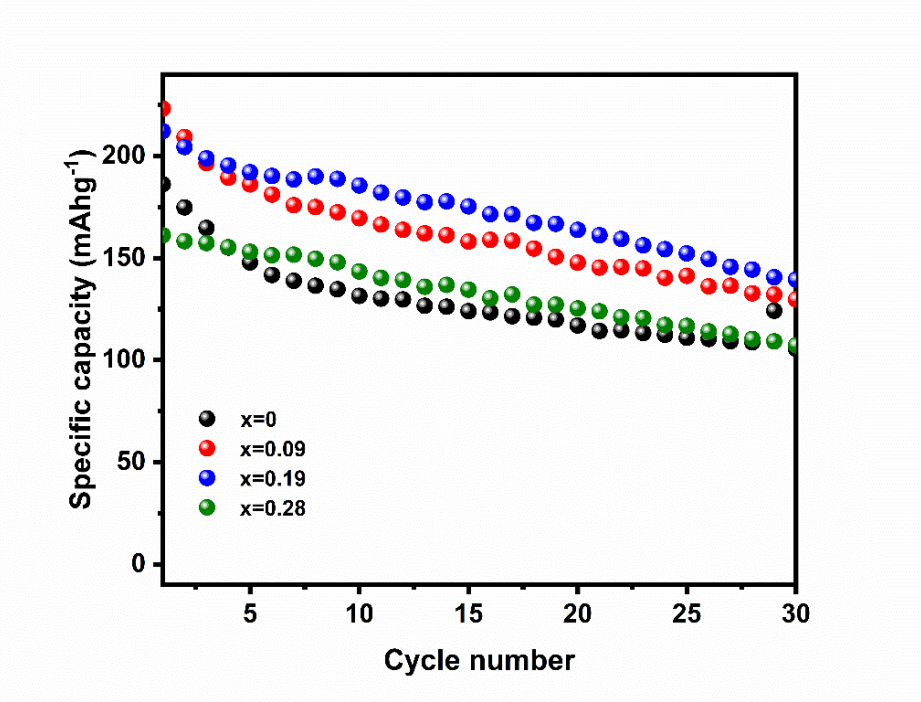

Figure S4. Cycling performance of $Na_{0.62}Mn_{1-x}Cu_xO_2$

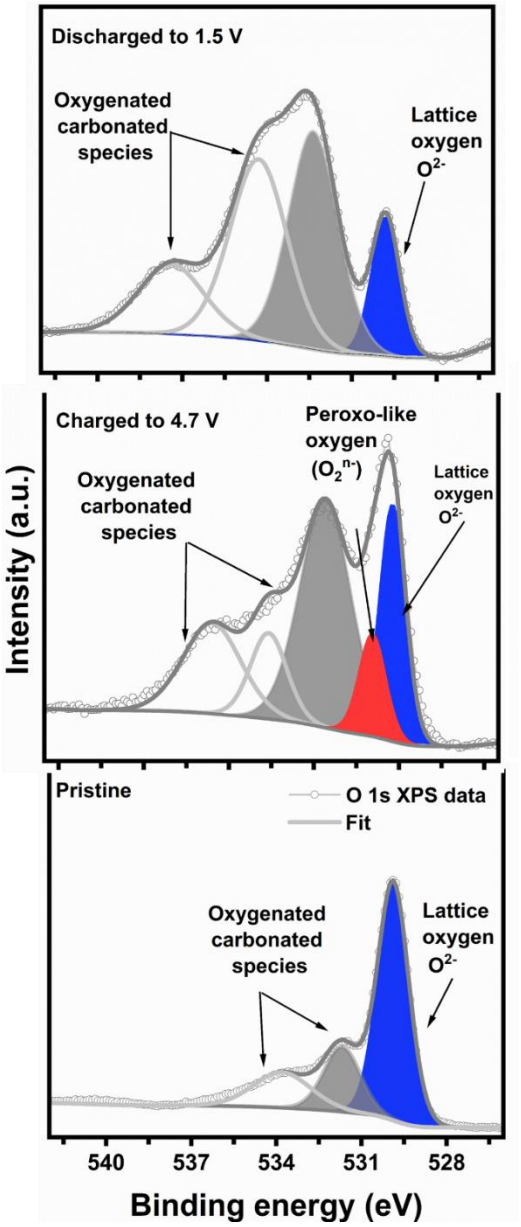

Figure S5. *Ex situ* XPS spectra of the electrode: O 1s

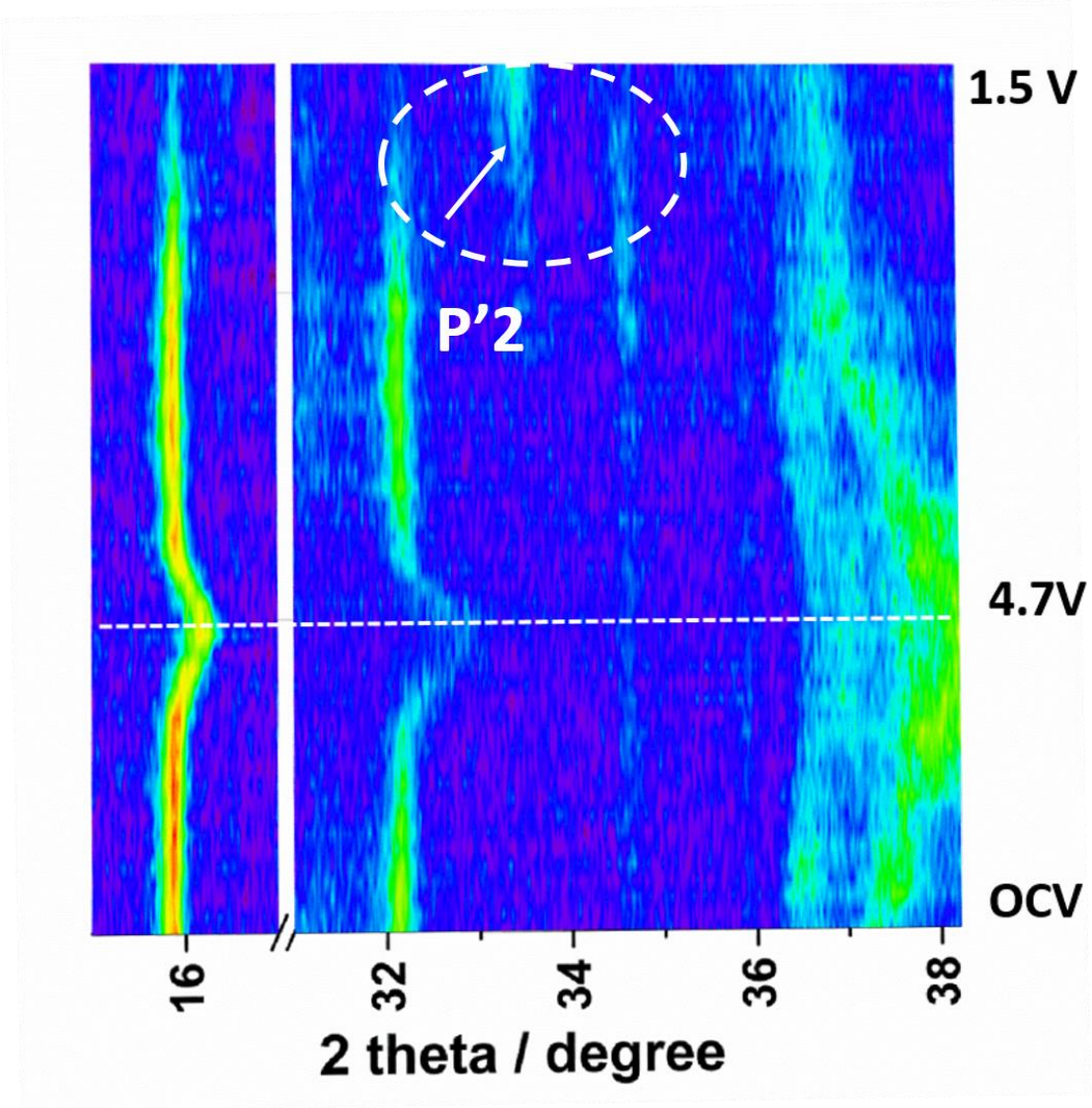

Figure S6. *Operando* XRD patterns of the first charge/discharge between 1.5−4.7 V undoped material

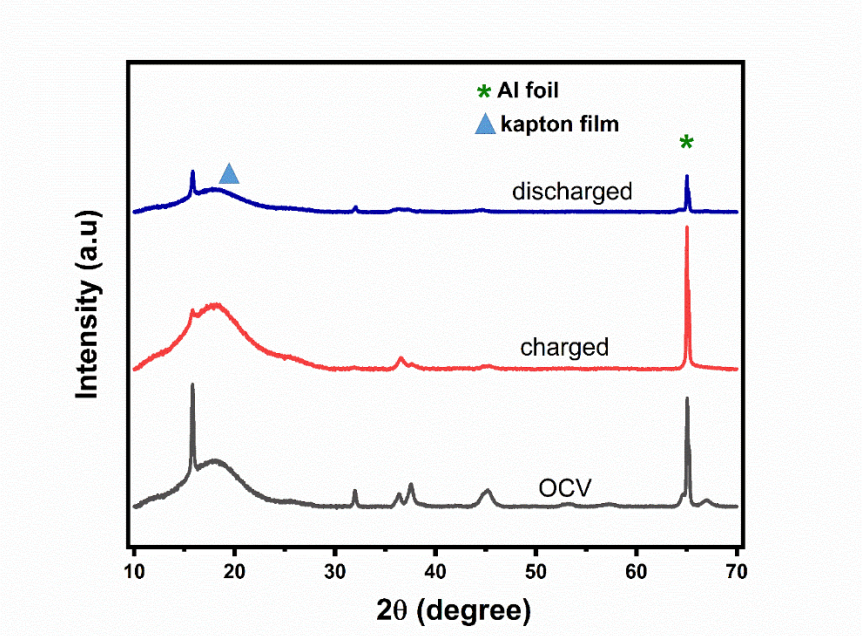

Figure S7. *Ex situ* XRD patterns of $Na_{0.62}Cu_{0.19}Mn_{0.75}O_2$ after 1st charge and 1st discharge

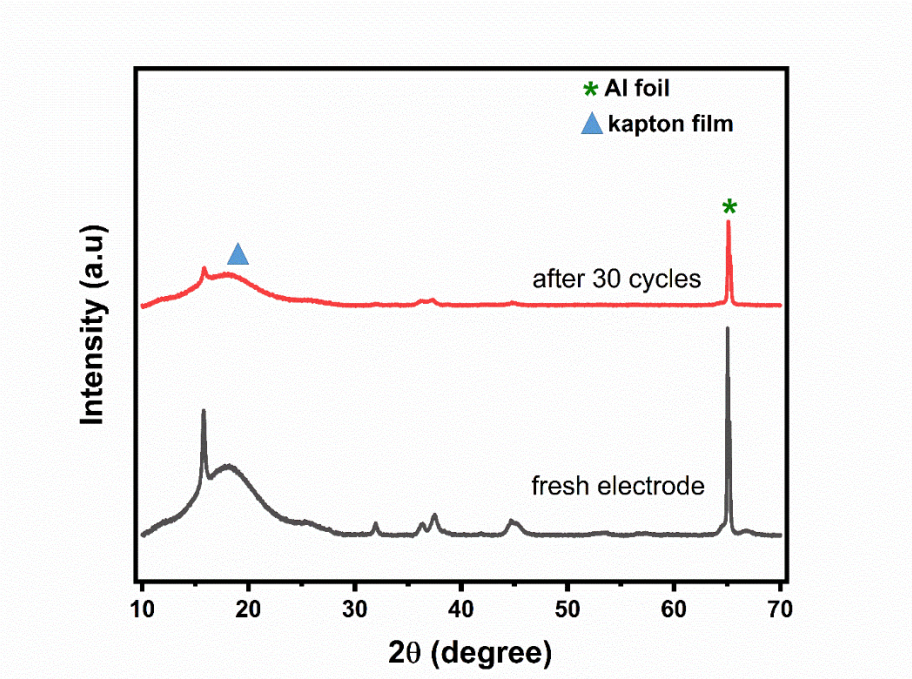

Figure S8. *Ex situ* XRD patterns of $Na_{0.62}Cu_{0.19}Mn_{0.75}O_2$ after 30 cycles

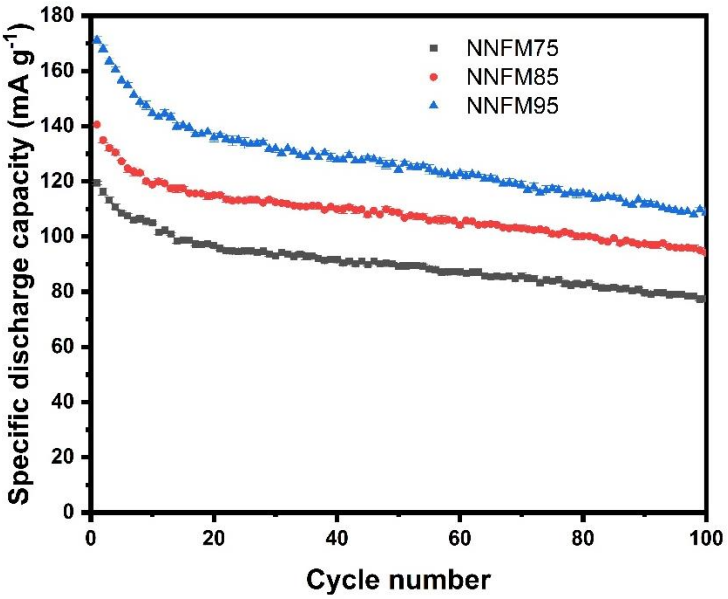

Figure S9. Cycling performance of NNFM cathodes with error bar

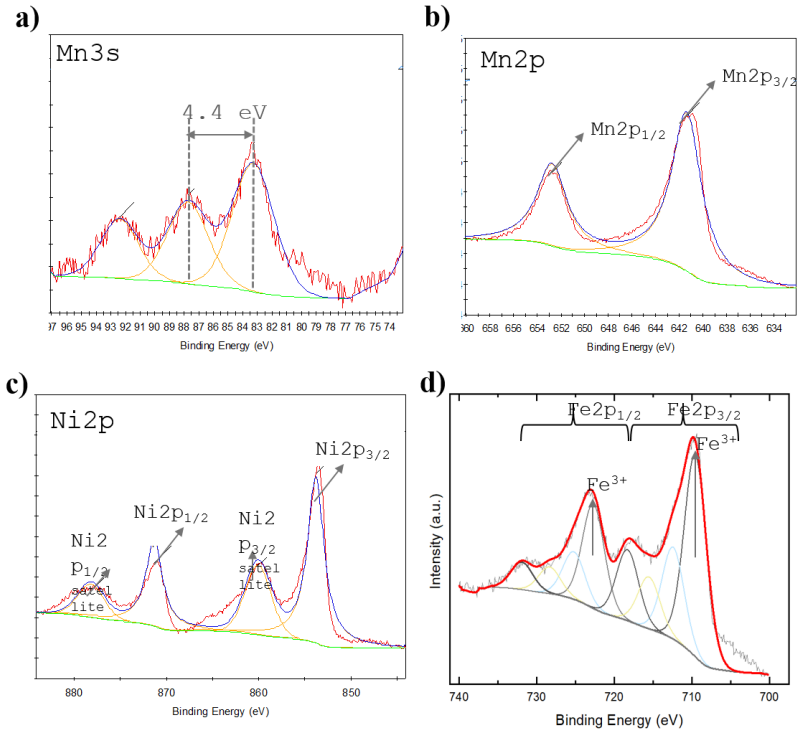

Figure S10. The XPS spectra of a) Mn 3s; b) Mn 2p; c) Ni 2p; d) Fe 2p.